Acoustic Vector Network Analyser

A thesis
submitted in fulfilment
of the requirements for the Degree
of

Doctor of Philosophy

at

The University of Waikato

by

Kyle Pennington

THE UNIVERSITY OF
WAIKATO
Te Whare Wānanga o Waikato

University of Waikato
2017

Abstract

This research aims at increasing the accuracy and precision of characterising acoustic materials by adapting well-known techniques developed for the radio-frequency domain to the acoustic domain.

Two novel methods are developed with different approaches for determining the reflectivity of materials: computationally and physically.

The first method is a advancement of the current "industry standard", the impedance tube, by using additional microphones and error correcting methods. A vector network analyser (VNA) is used as the data acquisition component with the aim of developing a module to allow the device to measure in the acoustic domain. The multi-microphone method employs the use of a mathematical model of the acoustics with the impedance tube to computationally solve for the unknown acoustic properties. The method is found to contain multiple sources of error at each stage of the process which makes reliable calibration and measurement difficult. The advantage of using a VNA is lost due to the inclusion of non-systematic error.

The second method uses wave superposition to form directional couplers to determine the reflectivity. This method allows for a more robust calibration routine as the error is systematic and can be corrected using intelligent procedures and measurement standards. The measurement accuracy was found to be ± 1.5 dB over a frequency range from 800 to 2200 Hz. The device is used to characterise the acoustic properties of pasture in order to aid the development of pasture meters. Pasture was found to reflect a relatively small amount and absorb the majority of the incident acoustic energy.

Preface

This research stems from the need of Gallagher Group Ltd to characterise the acoustic properties of pasture to assist in the possible development of a pasture meter, the details of which are commercial sensitive. I thought the project was interesting given the diverse range of elements involved in solving the problem: mechanical and electronic design, construction, software development, simulation, mathematics, physics, and biology. I had been inspired to start this project after working overseas on developing devices that measured the structural integrity of pipelines using acoustics in the petrochemical industry.

The problem of developing a device to characterise an acoustic element seemed to share many similarities to developing the VNA during the RF boom in the 1940s.

Firstly, an attempt was made to adapt a VNA to allow it to measure sound and soon branched into multiple devices utilising multiple measurement techniques.

I have ended up learning and developing a much broader range of topics and projects than the initial scope of this PhD.

Writing this thesis has been a battle of attrition. In hindsight I would have taken different approaches to this project, however in doing so, would have missed many of valuable lessons along the way. I hope that further research can be done in the exciting areas this project has uncovered.

Acknowledgements

I would like to thank my chief supervisor, Professor Jonathan Scott, for the opportunity to do this PhD and providing valuable feedback throughout the research and to Dr. Howell Round as my secondary supervisor. Thanks to Tony Smith and Kerry Bodman at Gallagher Group Ltd for working with me to develop a solution to an industrial problem. A special thank you to the Ministry of Business, Innovation, and Employment, New Zealand and Tanya Wakefield at the Postgraduate Studies Office for their generous help.

Finally, I will always be grateful to Rebecca, and my friends and family for their constant support.

Statement of Originality

There are a number of original contributions to the field of acoustic characterisation and calibration in this thesis.

The major contribution of this thesis is the realisation of an acoustic vector network analyser (AVNA) using a directional coupler and calibration standards. The initial idea to use a directional coupler in the acoustic domain was my chief supervisor's, Jonathan Scott, based on having a vast amount of experience using them in the radio frequency (RF) industry. The design and construction of the AVNA system, including the calibration standards, are my own.

The compensation algorithm and methods used to collect and process the measured data for the impedance tube method are novel, as well as this particular implementation of an impedance tube with a VNA.

Contents

1 Introduction

This chapter provides an overview of the current methods and calibration techniques in the literature to measure various useful acoustic properties. Section 1.1 explores the methods used to measure acoustic impedance and explains the limitations and advantages of each. Section 1.2 presents details on the similar techniques used in the radio frequency domain and the extensive research that has been done in this area to solve the calibration problems. Section 1.3 describes the operation and purpose of a vector network analyser (VNA).

1.1 Acoustic Impedance Measurement Methods

The ability to fully characterise the interaction of sound with objects or materials has a wide range of applications, including sound absorption materials, musical instruments [1], speaker enclosures, exhaust systems [2–4], ear canals [5], and vegetation [6–10].

A simple approach to characterise a material is to direct a sound wave of a specific frequency toward the surface of the material and observe the results. A portion of the incident travelling wave will be reflected, a portion absorbed within the material, and a portion transmitted through the other side of the material. The ratio of these portions can provide useful information about the behaviour of the material at that frequency, such as the attenuation constant and acoustic impedance.

Acoustic impedance $\mathbf{Z}$ is a commonly used parameter to describe the acoustic

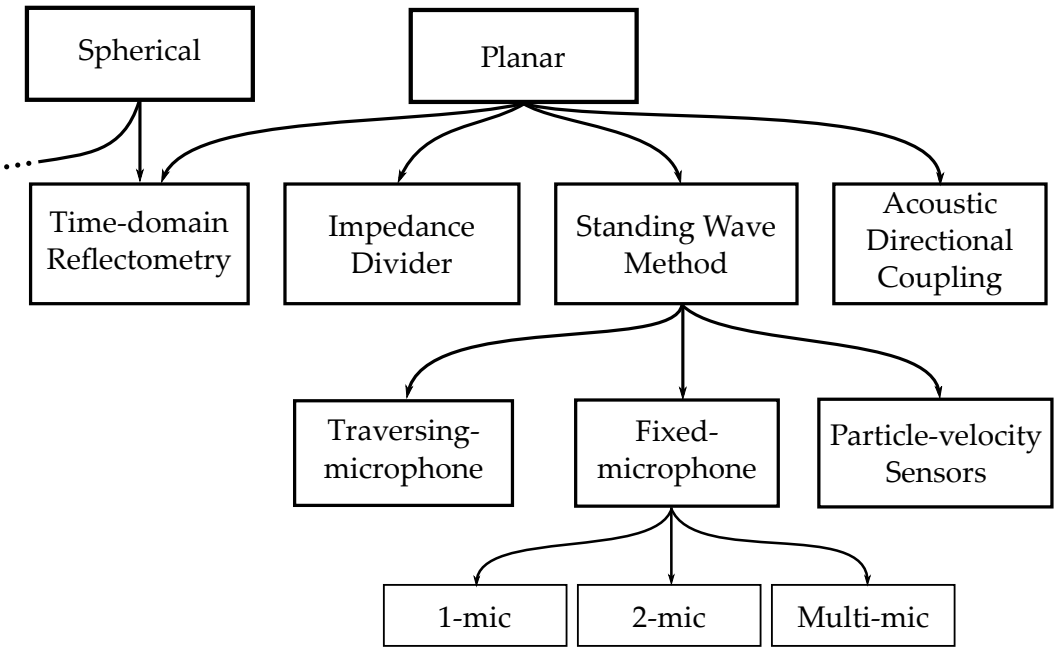

Figure 1.1: Diagram of the types of impedance measurement setups.

transmission properties of a medium or element defined as

$$Z = \frac{p}{U} \tag{1.1}$$

where p is the pressure and U is the volume velocity. Acoustic impedance can be used to determine the reflection and transmission of sound waves at interfaces if the acoustic impedance of the two mediums is known. The reflection coefficient is

$$\Gamma_{12} = \frac{Z_2 - Z_1}{Z_2 + Z_1} \tag{1.2}$$

for a wave travelling from medium 1 to medium 2 [11]. The proof is presented in Appendix A.1.

Techniques and instruments for measurement of acoustic impedance have been around for decades; the advances have been heavily dependent on the available electronics and computing technology of the time. Increasing the accuracy, precision, and speed of measurement are in constant development with many different hardware setups, techniques, and calibration procedures available. Benade and Ibisi [12]; Dalmont [13]; and Tao and Seybert [4] have performed literature reviews on this subject. An overview of the acoustic setup types is shown in Figure 1.1.

Acoustic impedance measurement types can generally categorised by their use

of either spherical or plane waves.

Spherical methods [8, 14, 15] employ the use of anechoic chambers or reverberation rooms and microphones are spatially arranged to measure the absorption and reflection properties of materials or objects. These methods take measurements from various directions and positions (depending on the application), not just normal to the surface of the material. In some cases, it may not be practical to move large complex objects into a laboratory for measurement; spherical methods can be performed in situ. These methods can also be useful when characterising anisotropic materials (i.e., materials that have properties which are dependant on direction) as their shape produce complex sound interactions. Calibration and repeatability is often difficult due to uncontrolled environment [16].

Plane waves are formed by transmitting sound through a straight rigid tube with a width that is smaller than the wavelength of interest, preventing sound waves from becoming multi-modal. The rigid tube is an acoustic transmission line, often called an "impedance tube". Testing a sample within the impedance tube has multiple advantages: this only requires a relatively small sample of material, saving costs; this does not require an anechoic chamber, saving space; and it is more easily calibrated due to the increased repeatability.

There are four methods used to determine the magnitude and phase of the incident and reflected waveforms: impedance divider method, standing-wave method, time-domain reflectometry (TDR), and acoustic directional coupling. The impedance divider method simplifies the problem by reducing the length of the impedance tube to minimise the effect of standing waves. The standing-wave method deduces the travelling waves from standing-wave pattern. The TDR method separates the waves in the time domain by only using a brief signal and measuring the waveforms separately. The directional coupling method physically separates the waveforms using geometry. These methods are further explained in the following sections.

1.1.1 Impedance Divider Methods

The impedance divider methods were one of the earliest methods to determine acoustic impedance, dating back to the late '40s [17, 18]. One implementation uses a sound driver and a microphone separated by a high impedance (narrow tube), shown in Figure 1.2 . When $Z_L \ll Z_{large}$, this setup effectively produces a constant velocity source (analogous to a current source in the electrical domain). Given that the particle velocity is constant, equation 1.1 shows that the measured pressure is directly proportional to the unknown impedance. This relationship is advantageous as it does not require the use of computers. However, the presence of

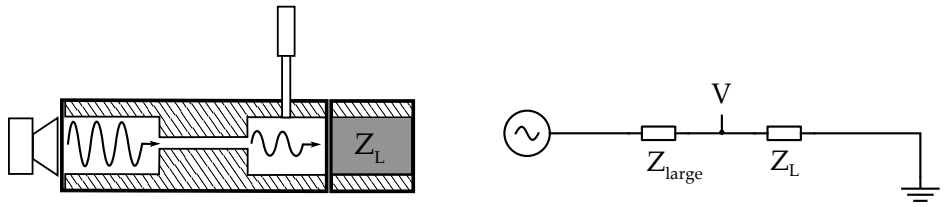

Figure 1.2: Left: Diagram of an impedance divider method. A high impedance load (narrow tube) separates the sound driver and the unknown load Z_L. Right: The electronic equivalent circuit to the acoustic setup with the voltage source replacing the sound driver and the voltage V replacing the microphone.

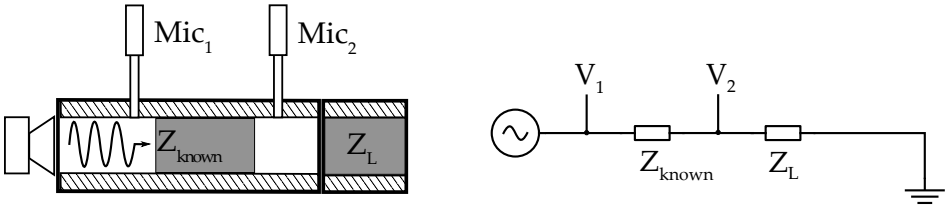

Figure 1.3: Left: Acoustic impedance divider setup. Two microphones are separated by a load of known impedance. Right: The electronic equivalent circuit to the acoustic setup.

standing waves in the tube will cause inaccurate impedance measurements due to the pressure fluctuations. To minimise this effect, the wavelengths must be much greater than length of the tube. Also, the magnitude of the signal in the second chamber is small due to the narrow capillary tube. This increases the difficulty in isolating noise from the environment and stray noise from the first chamber which will degrade the precision and accuracy.

To summarise, there are three major limitations with this approach: it cannot measure high impedance loads; it is only useful at low frequencies; and it has a low signal-to-noise ratio.

In 1993, de Block and van den Brink [19] used the impedance divider method using two microphones separated by a known impedance, shown in Figure 1.3. The volume velocity can be expressed as

$$U = \frac{p_1 - p_2}{Z_{known}} \tag{1.3}$$

and

$$U = \frac{p_2}{Z_L}. \tag{1.4}$$

This method is analogous to a voltage divider in the electronic domain, where the load impedance Z_L becomes

$$Z_L = \frac{p_2}{p_1 - p_2} \cdot Z_{known}. \tag{1.5}$$

Z_{known} is realised by empirically adjusting packed wool layers so that it is equal to $Z_0 - Z_{source}$, where Z_0 is the characteristic impedance of the impedance tube and Z_{source} is the impedance of the acoustic driver. Under this condition the device would be matched, although explicit details on how de Blok and van den Brink achieved the matching of this impedance are not given in their manuscript. This method also has a low maximum working frequency (100 Hz) because of the requirement to avoid multi-modal waves. The advantage of this system is at low frequencies where standing-wave methods will be seen to require impedance tubes greater than ten metres.

1.1.2 Standing-Wave Method

The standing-wave method involves measuring the standing-wave pattern caused by the superposition of the incident and reflected plane waves formed in an impedance tube. An introduction and overview of the existing literature of the standing-wave method and its various forms are provided in this section; we will look at this in more depth in Chapter 2 and devise several original techniques to improve upon the method.

Historically, the traversing-microphone method was used to determine the standing-wave ratio which does not require computers to calculate acoustic impedance. In 1953, Lippert [20] discusses the standing-wave pattern and a technique to measure it with probe microphone having multiple tube orifices.

Traversing-microphone Method

The traversing-microphone method [21–23] uses an impedance tube with a sound source and load at either end. A probe tube microphone and sound source are positioned in such a way to allow the tip of the microphone to traverse along the tube, shown in Figure 1.4. Measurements are made to find the position and magnitude of the maxima and minima of the standing wave (Figure 1.5). It is of interest to note that the distance between the minima (and maxima) is always $\lambda/2$, and the maxima are positioned half way between. Note that in Figure 1.5 the minima of the standing-wave pattern are predicted as having unequal depths. The change in the minima magnitude is not due to the acoustic load, but the attenuation of the impedance tube. An ideal impedance tube would have equal minima magnitudes.

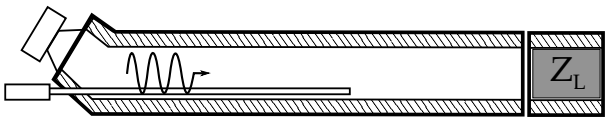

Figure 1.4: Diagram of the traversing-microphone method.

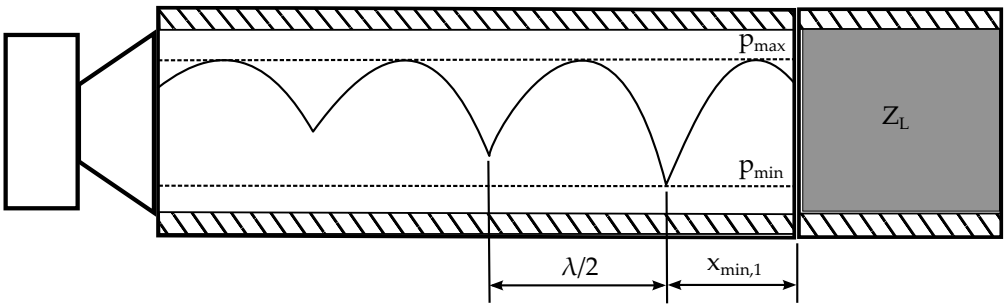

Figure 1.5: Representation of a standing wave pattern in an impedance tube. The position of the first minima $x_{min,1}$, the magnitude of the maxima $|p_{max}|$, and minima $|p_{min}|$ are shown.

From the ISO[1] [22] and ASTM[2] [23] standards, the standing wave ratio SWR is

$$\text{SWR} = \frac{|p_{max}|}{|p_{min}|}. \tag{1.6}$$

The magnitude of the maxima and minima can be expressed as

$$\begin{aligned} |p_{max}| &= |p_i| + |p_r| \\ &= |p_i| + |\Gamma p_i| \\ &= |p_i|(1 + |\Gamma|) \end{aligned} \tag{1.7}$$

and

$$\begin{aligned} |p_{min}| &= |p_i| - |p_r| \\ &= |p_i| - |\Gamma p_i| \\ &= |p_i|(1 - |\Gamma|). \end{aligned} \tag{1.8}$$

Combining with equation 1.6 and rearranging for the reflection coefficient mag-

[1] International Organization for Standardization.
[2] American Society for Testing and Materials.

nitude $|\Gamma|$ gives

$$|\Gamma| = \frac{\text{SWR} - 1}{\text{SWR} + 1}. \tag{1.9}$$

The phase ϕ of the reflection can also be determined from the position of the first minima $x_{\text{min},1}$, such that

$$\phi = \pi \left(\frac{4x_{\text{min},1}}{\lambda} - 1 \right) \tag{1.10}$$

where λ is the wavelength.

The traversing-microphone method has three major limitations:

- It is laborious and time consuming, as the microphone must be manually moved to find the maxima and minima for each frequency.
- The length of the impedance tube must be at least one half the wavelength of interest, implying that measurement at a low frequency would require a large setup.
- The microphone is obstructing the sound field in the impedance tube which causes measurement errors.

Fixed-microphone Methods

The physical interference of the traversing microphone can be minimised using two fixed sensors, mounted flush, through the impedance tube wall. This also removes the need to manually move the microphone. The drawback is that the microphones will not be in the correct position to measure the maxima and minima across a range of frequencies. In principle this is not necessary.

Given the relationship in equation 1.1, a microphone (pressure sensor) can be substituted for a device to measure the volume velocity of the air through a cross-section of the tube, commonly called a "volume velocity sensor".

In 1996, de Bree et al. [24] invented a new sensor for volume velocity called the microflown (stylised as μ-flown). A hot wire anemometer was used by Pratt et al [25] with some success.

Volume velocity and pressure setups [15, 26] succumb to similar effects as the traversing microphone, that is, the sensor physically interferes with the sound field. The combination of two sensor types also requires an additional step to calibrate the relationship between the measured voltages. This method is uncommon for these reasons, so most configurations utilise two or more pressure sensors in a variety of arrangements.

Two-microphone methods [1, 3, 8, 9, 13, 16, 19, 27–41], shown in Figure 1.6 (a), are the most commonly used. This method attempts to determine the same standing wave parameters found in the traversing-microphone method, but they must be

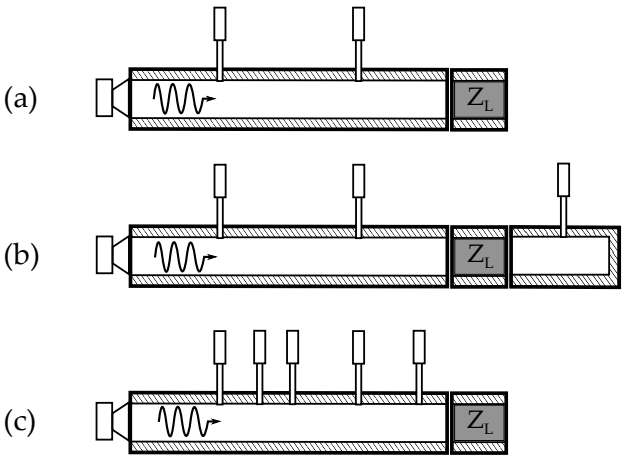

Figure 1.6: Diagram of various standing-wave methods. (a) Two-microphone. (b) Three-microphone. (c) Multi-microphone.

calculated rather than directly measured. A series of equations representing the forward and reverse travelling waves at the two measurement positions can be formed, given that the positions of the microphones are known precisely with respect to the measurement plane. These equations are resolved to find the complex reflection coefficient of the device under test (DUT).

Two variations of the calculation are found in the literature: the "transfer-function" method [33] and the "wave decomposition" theory [11]. Both of these methods ultimately yield exactly the same result but use different notation to resolve the simultaneous equations.

The transfer-function method takes less steps to determine the answer by simply applying transfer matrices of bundled parameters. However, the abstract nature of these matrices means that it is not intuitive. The wave decomposition theory will be used throughout this thesis as it can easily be adapted to many set-ups and even the radio frequency (RF) domain.

In 1977, Seybert and Ross [16] introduced the two-microphone method. They used Gaussian white noise to drive the sound source and two wall-mounted microphones were used to capture the acoustic spectra. The data is then Fourier transformed to the frequency domain and averaged. A third microphone was added downstream of the DUT to measure the transmission loss. Attenuation in the tube is assumed negligible due to the close microphone spacing. The differences in microphone sensitivity and phase were corrected by flush-mounting the microphones on a plate at the end of the impedance tube. An offset short, an offset open, and a muffler were measured. The method is shown to break down at frequencies corresponding to half wavelength intervals due to ill conditioned equations. At these intervals the

equations contain redundant data because the measurement positions are effectively measuring the same position, which becomes unsolvable.

In 1980, Chung and Blaser [28, 29] developed a calibration procedure where the microphone positions are switched in order to correct phase and magnitude differences between the microphones. In the experiments, an additional microphone is added in the same x-axis location as microphone One. Noise is purposely added to one of the microphones signal to test the systems susceptibility to noise. A 19 mm thickness foam and an open were measured. The accuracy of this method was found to be comparable to the standing-wave methods, but about 40 times faster. It was found that the distance from the surface of the test sample to the nearest microphone should be kept to a minimum, but greater than 10 mm in their case. This is likely due to the turbulence close to porous materials - what RF people call "evanescent modes".

In 1983, Smith and Parrott [42] evaluated the two measurement techniques used to measure material samples, the two-thickness method and the two-cavity method. The method attempts to determine the material measurement from the cavity by changing the dimensions of one out of two separate measurements. The two-thickness method measures the material at a single thickness, then with a doubled thickness sample. The two-cavity method uses one sample of material but changes the length of the cavity behind the sample. The two-cavity method was found superior as it was faster to replace the cavity than attach an additional material thickness. The method was also advantageous as it did not have contact with the original sample and cause positional errors.

In 1986, Chu [31] identified the assumption of no impedance tube attenuation in Chung and Blaser's and Seybert and Ross' method. Chu calculated that a 1% error in the measurement of the reflection coefficient would result in an error of 8.5% for the absorption coefficient.

In 1986, Bodén and Åbom [30] investigated the influence of some errors on the two-microphone method by numerical simulation and experimental measurement. In the case of using a broadband acoustic source, they find that the error caused by inadequate spectral resolution can be reduced by decreasing the impedance tube length and keeping the distance between the microphone and the acoustic element small. However, the system breaks down as the distance between the microphones approaches zero. They concluded that the length of the impedance tube should be kept short (5-10 duct diameters) and the source impedance should be well matched to avoid reflections. A typical accuracy of ± 0.5 mm with a millimetre rule to measure the microphone positions result in a relative error of less than 1% for separation distances over 50 mm.

In 1989, Jones and Parrott [43] evaluated the two-microphone method and found

that two microphones can achieve measurements at some frequencies which fulfil conditions. They also explored the use of additional microphones to improve accuracy, which are most accurate when evenly spaced across a half-wavelength.

In 1990, Gibiat and Laloë [1] introduced a calibration routine for the two-microphone method which used a 'short' and two 'offset-shorts'. The short is a solid cover on the end of the impedance tube which ideally has a reflection coefficient of 1. The offset short is a short with a section of impedance tube which adds phase shift and allows for a wider usable frequency range.This calibration routine corrected several sources of systematic error caused by geometrical imperfections of the measurement device or the microphones.

In 1990, McIntosh et al. [44] used an extra measurement position in a cavity downstream of the unknown material to determine the acoustic loss, shown in Figure 1.6 (b). They found that for accurate measurement of propagation constant, characteristic admittance, and bulk modulus – the sample thickness must be approximately a wavelength or more. Thinner thicknesses give accurate measurements of finite amplitude flow impedance.

In 1991, Champoux and Stinson [45] used a similar technique to McIntosh et al. but had an improved accuracy when measuring highly resistive loads.

In 1991, Chu [46] compared the accuracy between using a Gaussian noise or a pure sine-wave sound source. It was found that the pure sine-wave source had better accuracy. Multiple microphones were also tested. A least-squares fit technique was developed with the additional microphones. It was found that the positions of the microphones play a significant role in the precision of the acoustic measurements. Arbitrary microphone spacing, as earlier suggested, is not well optimised over the full working frequency range.

In 1992, de Blok and van den Brink [21] explored the characterisation of unknown acoustic elements and the ability to characterise without the knowledge of the internal structure. This theory can be extended to N-port setups.

In 2000, Song and Bolton [47] used a pair of two-microphone setups to form a two-port acoustic measurement system. They used the system to characterise porous materials with fewer measurements by using the reciprocity of homogeneous and isotropic materials. The assumption limits the use of this method from being used on asymmetrical materials or ports.

In 2001, Dalmont [48] presented a calibration technique for methods utilising constant-velocity sources using multiple "offset shorts" (known length tubes with a sealed reflective termination). The frequency is swept until the system resonates due to the offset shorts. This technique is independent of temperature related error due to not relying on a known wave number. However, this technique only yields calibrated data for every resonant harmonic; any frequency between must be

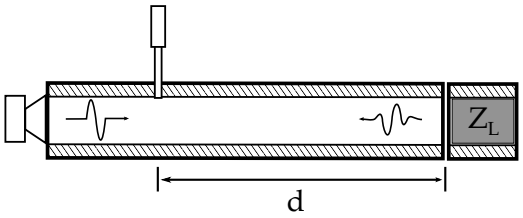

Figure 1.7: Diagram of a time-domain reflectometer.

interpolated.

In 2005, Ho et al. [49] developed a two-port system with four microphones similar to Song and Bolton. The system was also limited to symmetrical materials.

In 2009, Salissou and Panneton [50] tested several two-microphone and four-microphone methods from the literature for comparison. They also proposed an improved version of Ho et al. by accounting for asymmetrical materials.

In 2009, Song and Bolton [47] used the two-microphone method to estimate the impedance and characterisation of porous materials, although it is limited to isotropic materials.

Three [44, 48, 51, 52] and four-microphone methods [47, 49–51] use extra microphones to over-determine the system of simultaneous equations. Multi-microphone methods [53–57], shown in Figure 1.6 (c), provide a wider working frequency range, and greater accuracy by reducing dependence on the precision of each microphone.

One notable example of this method is Price [55] who uses six microphones in the impedance tube to determine the magnitude and phase of the travelling waves. A custom made jig to compensating the microphones is used and the microphones are measured simultaneously with a Presonus digitiser. This implementation of the standing-wave method appears to be well designed and is shown to measure an open-ended tube with good accuracy. The multi-microphone method is further explored in Chapter 2.

Brüel & Kjær commercially produce an impedance tube [41] utilising the two-microphone transfer function [58], which has been used by many researchers [8, 47, 53] in the field.

1.1.3 Time-domain Reflectometry

Both spherical and planar systems can take advantage of Time-domain Reflectometry (TDR) [5, 38, 59]. This technique transmits a brief signal or impulse and measures the resulting waveform at a position in the system over time. A single microphone is used as shown in Figure 1.7 using an impedance tube. The incident waveform must be brief so that the microphone can measure the waveforms separately without any

overlap.

The duration the signal takes to travel from the microphone to the test element and back to the microphone is dependant on the speed of sound c in the medium and the distance d from the microphone to the test element, such that the duration is

$$\Delta t = \frac{2d}{c}. \tag{1.11}$$

In order to separate the signals, the system must compromise between the length of the tube and the duration of the signal. The accuracy of the measurement is dependant on the signal-to-noise ratio of the returning signal. If the tube it too long, the signal will attenuate and the returning signal will be too weak. If the signal duration is too brief there will not be enough energy for analysis.

The positions of acoustic impedance changes along the tube, or in the test port, can be determined from the reflected waveform if the speed of sound is known. If an impulse is used then the acoustic impedance at each frequency can also be found by applying a Fourier transform to the reflected response [59].

In 2007, Lefebvre et al. [59] developed a TDR and compared it to the two-microphone method of Seybert and Ross. The calibration method simply measures the unknown port then normalises with the response of a rigid termination. The method is found to be fast but requires a long tube and is inaccurate at high frequencies due to attenuation.

1.1.4 Acoustic Directional Coupler

Another method of determining the magnitude and phase of the travelling waves is to use a directional coupler. This method uses a branch-guide coupler to physically separate a proportion of each wave to be measured. The difficulty with this method is that branch-guide couplers are far from ideal even at the designed frequency of interest. As the frequency range of the device is extended this problem is exacerbated. A method to correct the errors in the acoustic directional coupler has not yet been found in the literature. We discuss a novel solution further in Chapter 3 as the main contribution of this thesis.

1.2 Comparison with the Radio Frequency Domain

In the radio frequency domain there is a need to characterise electrical networks to determine their effects on a signal. This characterisation allows designers to build and optimise larger electrical systems with the knowledge of how components will behave. The vector network analyser (VNA) is a commonly used tool to measure impedance in the electrical domain, similar to the acoustic directional coupler

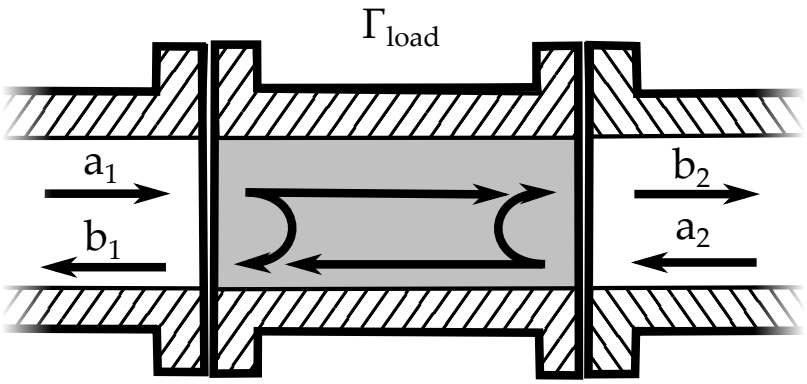

Figure 1.8: Two-port S-parameters.

previously mentioned. Passive electrical components such as resistors, capacitors, and inductors all have equivalent acoustic counterparts. The similarity between the two domains was found to be sufficient to warrant an investigation if any of the technologies developed by the heavily funded microwave electronics industry could be applied to acoustics. This section covers the prerequisite knowledge relating to the VNA and its development.

1.2.1 Scattering Parameters

Electromagnetic waves are commonly propagated through transmission lines such as coaxial cable or waveguide (much like sound in an impedance tube). When the wave travels through an impedance change, part of the wave is reflected, and part is transmitted. Scattering parameters (also known as S-parameters) describe the reflection and transmission of these waves, where the reflection coefficient of port one is

$$S_{11} = \Gamma_{load} = \frac{\text{Reflected}}{\text{Incident}} = \frac{b_1}{a_1}. \tag{1.12}$$

The s-parameters for a two-port load are shown in Figure 1.8 . The complex linear gain of port one and two are

$$S_{21} = \frac{b_2}{a_1} \tag{1.13}$$

and

$$S_{12} = \frac{b_1}{a_2} \tag{1.14}$$

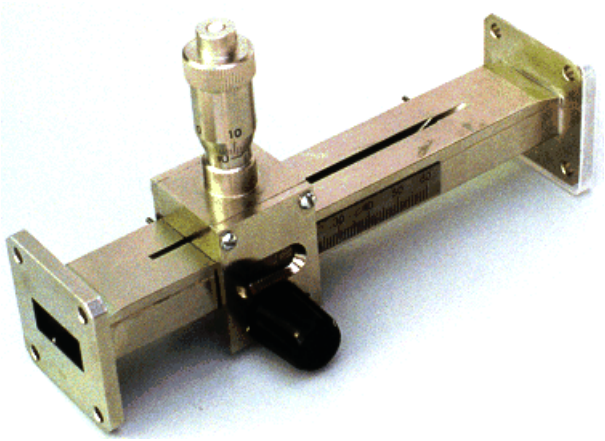

Figure 1.9: Slotted-line and moveable detector. [61]

respectively. Similarly, the reflection coefficient of port two is

$$\mathbf{S}_{22} = \frac{\mathbf{b}_2}{\mathbf{a}_2}. \tag{1.15}$$

Appendix D provides further detail on S-parameters and signal flow graphs.

The impedance of the load can be determined if the characteristic impedance of the line and the reflection coefficient is known:

$$\mathbf{Z}_{\text{load}} = \mathbf{Z}_0 \frac{1 + \mathbf{\Gamma}_{\text{load}}}{1 - \mathbf{\Gamma}_{\text{load}}}. \tag{1.16}$$

1.2.2 Slotted Line Method

Dr. Rohde and Dr. Schwarz founded Rohde & Schwarz in 1933. One of their early products was a slotted-line device which uses the standing wave theory similar to that described in Section 1.1.2 [60]. The slotted-line is a section of waveguide or coaxial with a long narrow slot cut down the length of one side. A moveable detector slides along the length of the waveguide to measure the magnitude of the electromagnetic wave inside. Figure 1.9 shows a photograph of a slotted-line and moveable detector. In the electromagnetic domain the radiation does not escape due to there not being an electric field perpendicular to the slot [62]. The same effect can not be utilised in sound due to the different propagation physics. The slotted-line device has the disadvantage that measurements must be made with one frequency at a time and is laborious. This device has all but disappear in the modern day.

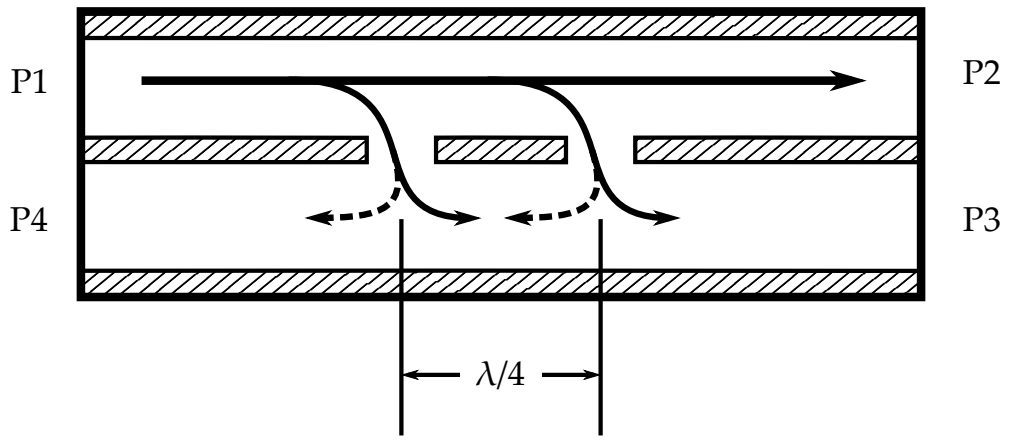

Figure 1.10: Cross-section of a two-aperture directional coupler. The input wave travels in the main line from P1 (input port) to P2 (transmitted port). The waves travelling through the aperture towards P3 (coupled port) are in phase so they constructively interfere. Whereas the waves travelling towards P4 (isolated port) are $\lambda/2$ out of phase and cancel.

1.2.3 Directional Coupler

A directional coupler is a device used to separate a proportion of the waves travelling in one direction to a secondary circuit, often used for measurement. A directional coupler implemented in waveguide has two lines coupled together, the main line and the coupled line, with a series of apertures $\lambda/4$ apart. Figure 1.10 shows a simple two-aperture coupler. Waves in the coupling line travelling in the same direction as the main line constructively interfere, whereas the reverse cancel.

Directivity is a measure of how much separation there is between the forward and reverse waves in the coupling line i.e. $P3/P4$. The directivity is greatest at the design frequency (shown in Figure 1.11) and rolls off at other frequencies as the reverse wave becomes larger. The coupler has ideal directionality at wavelength multiples, when the distance between apertures is $\lambda(n+\frac{1}{4})$. The coupler also reverses directionality when the distance between apertures is $\lambda(n+\frac{1}{2})$.

The earliest directional couplers first began to appear in the 1920s and 1930s for wire and coaxial lines [63]. These were typically only used as power-splitters which did not require high directivity.

In 1959, Levy [64] presented a method to design directional couplers using Chebyshev filters to achieve high directivity over wide bandwidths. Near ideal directivity at one frequency is sacrificed for a sufficient directivity over a wide bandwidth.

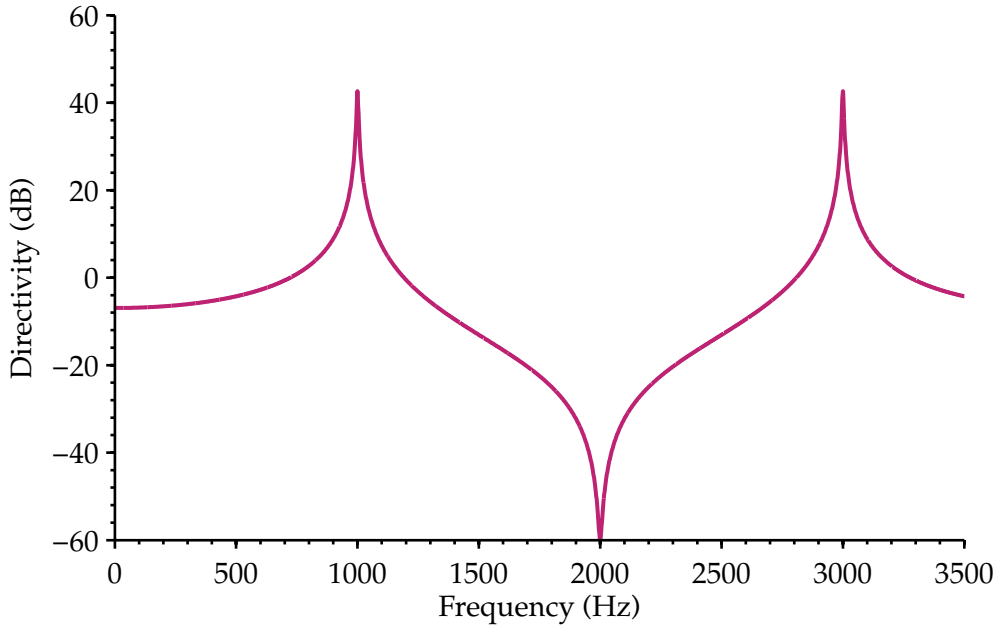

Figure 1.11: Theoretical directivity of a two-aperture coupler designed for 1 kHz. The first harmonic is shown at 3 kHz.

1.3 Vector Network Analyser

After the slotted-line there was a push for devices which measured impedance with increased automation and speed. An alternate technique to the standing wave theory is to separate the forward and reverse waves with a directional coupler. A small proportion of the forward signal is directed to the coupled port of the coupling line. The magnitude and phase of forward wave is determined from the measurement of this port, with some prior knowledge of the coupler's characteristics.

The difficulty before the 1950s was generating a stable reference oscillator that could be swept over a wide range of frequencies and measuring the phase differences with a high degree of accuracy. In 1951, Epsztein [65] patented the m-type backward wave oscillator (BWO) which allowed voltage-controlled frequency generation of over an octave.

In the early 1950s Rohde & Schwarz released the first VNA they called a 'Z-g-diagraph', capable of measuring magnitude and phase of S-parameters up to 300 MHz. In 1954 the Z-g-diagraph reached frequencies of 2.4 GHz.

By 1967 the advancement of microelectronics allowed a computer to be connected to the HP 8540 for calibration, the first automatic error corrected VNA [66]. This prompted the development of error correction algorithms to improve accuracy.

The 'Short-Open-Load-Thru' (SOLT) method was one of the earliest methods

and is still commonly used. The method employs the use of multiple calibration standards which are measured by the VNA to determine the bias errors of the device itself. These errors are then corrected after a measurement of a DUT is performed. The short and open calibration standards behave differently in the acoustic domain compared to the RF domain. An RF short has a π phase shift as Ohm's law states that the voltage across the short will be zero. An acoustic short is a solid wall on the end of the impedance tube which is an infinite impedance resulting in a reflection coefficient with no phase shift. Further detail is provided in Chapter 4.

In 1979, Engen and Hoer [67] introduced the 'Thru-Reflect-Line' (TRL) calibration technique. The technique is particularly useful for applications with immobile test ports, such as wafer probing and waveguide [68]. Today it is still considered one of the highest quality error correction methods [69].

The 'unknown thru' calibration technique was developed in 1992 by Ferrero and Pisani [70]. As the name implies, the technique does not require the impedance of the 'thru' to be known in order to complete a full two-port calibration.

2

Standing-Wave Method

This chapter explores the use of impedance tubes to measure the reflectivity of acoustic loads with standing-waves. In Section 2.1, the underlying standing-wave theory is explained and aspects are shown which can be exploited with a numerical fit of multiple measurement positions. An overview of early methods using the standing wave pattern is presented in Section 2.2. Section 2.4 discusses the design and construction of an original impedance tube measurement system, outlining the hardware used and the reasoning behind it. Measurements are then taken in Section 2.6 as a consistency check and an investigation into the sources of error takes place in Section 2.8.

2.1 Theory

This section shows the connection between the standing-wave pattern and the reflection coefficient of the load.

2.1.1 Travelling Waves

An accurate model of the measured sound pressure must be developed in order to decompose the standing wave into the constituent travelling plane waves.

The general form for the sound pressure, $\mathbf{p}$, of a single travelling wave can be

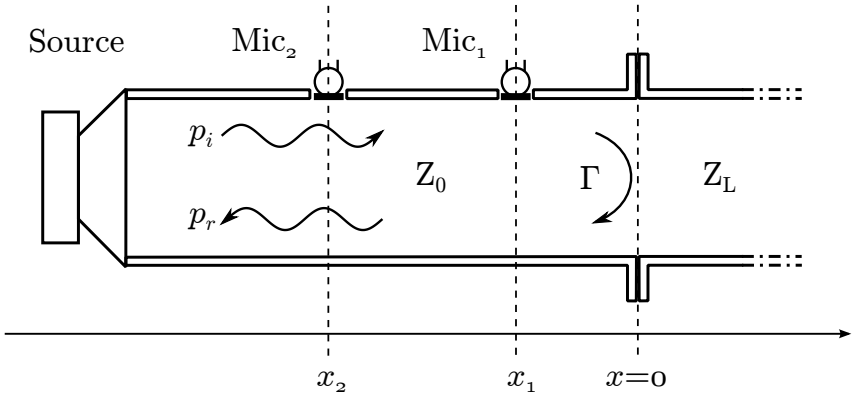

Figure 2.1: Two-microphone impedance tube showing the incident and reflected travelling waves. The load is Z_L.

represented at any point on the x-axis and time, t, by

$$\mathbf{p}(x,t) = Ae^{j(kx-\omega t+\phi)} \tag{2.1}$$

and

$$\mathbf{k} = \frac{\omega}{c} + j\alpha \tag{2.2}$$

where:

- A is the amplitude;
- ω is the angular frequency;
- ϕ is the phase shift;
- c is the speed of sound;
- α is the attenuation constant.

Letting $\mathbf{A} = Ae^{j\phi}$ and dropping ωt, by using the phasor representation, the pressure of the incident (positive x) and reflected (negative x) plane sound waves can be expressed as

$$\mathbf{p}_i(x) = \mathbf{A}_i e^{jkx} \tag{2.3}$$

and

$$\mathbf{p}_r(x) = \mathbf{A}_r e^{-jkx}, \tag{2.4}$$

respectively. Figure 2.1 is a diagram showing the relationship between the travelling waves and the load, Z_L. Using superposition, the measured sound pressure at a point, x, becomes

$$\mathbf{p}(x) = \mathbf{A}_i e^{jkx} + \mathbf{A}_r e^{-jkx}. \tag{2.5}$$

The complex reflection coefficient, Γ, of the load at $x = 0$ is

$$\Gamma = \frac{A_r}{A_i} = \frac{Z_L - Z_0}{Z_L + Z_0}, \tag{2.6}$$

where Z_0 is the characteristic impedance of the impedance tube. An obvious, but important, note to make is that the reflection coefficient of the load is the ratio of reflected to incident sound waves. The impedance of the load can also be determined from this ratio if the characteristic impedance of the tube is known. Measuring the magnitude and phase of the incident and reflected waves is difficult as they become superimposed in the impedance tube for signal durations longer than a few milliseconds, depending on the setup. The superposition of the waves creates a pattern unique to the magnitude and phase of the waves, called a standing wave pattern.

2.1.2 Standing Waves

Standing wave patterns are a phenomenon caused by the interference of two waves travelling in opposite directions. Periodic maxima and minima occur along the length of the tube when a DUT with an impedance other than the characteristic impedance is attached to the measurement port. The maxima and minima are spaced one quarter wavelength apart and the phases of the travelling waves determines the longitudinal shift of the pattern.

The standing wave patterns for a range of reflection coefficients are shown in Figure 2.2. If the impedance tube has a characteristic impedance Z_0 then $\Gamma = 0$, $\Gamma = 0.5$, and $\Gamma = 1$ would be produced in the following conditions $Z_L = Z_0$, $Z_L = 3Z_0$, and $Z_L = \infty$, respectively.

Attenuation of the travelling waves inside the impedance tube also affects the standing wave pattern as shown in Figure 2.3.

2.2 Early Methods Using the Standing Wave Ratio

Several early methods exist that use the standing wave method to then determine the reflection coefficient or impedance of a load. They are relatively simple and cheap methods for determining impedance but are laborious and time consuming.

Slotted-Line Method

The slotted-line method was used to measure the standing wave ratio in the RF domain. The slotted line device consists of a section of waveguide with a long narrow slot cut down the length of one of the sides. The slot allows for a measurement

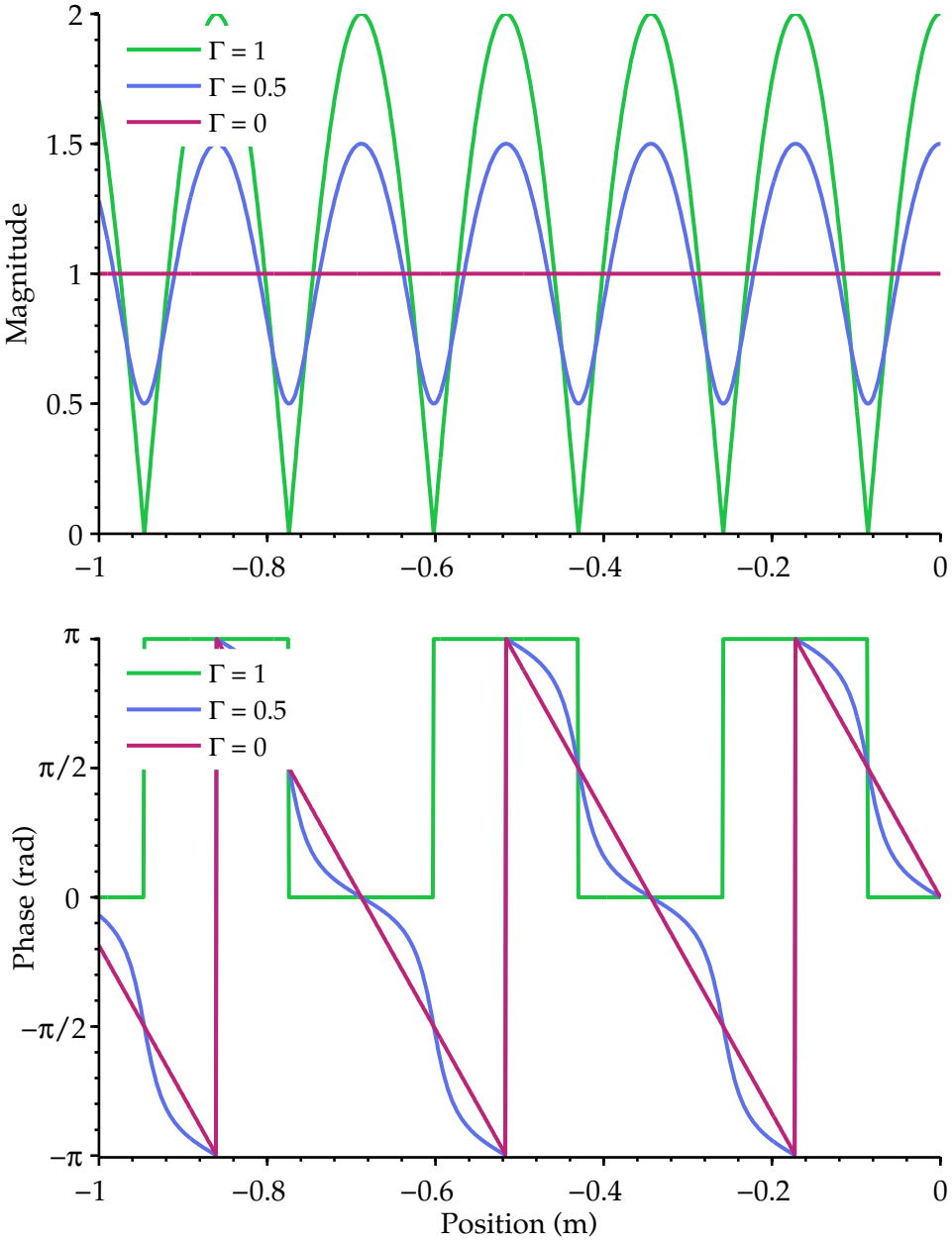

Figure 2.2: Various theoretical standing wave patterns at 1 kHz.

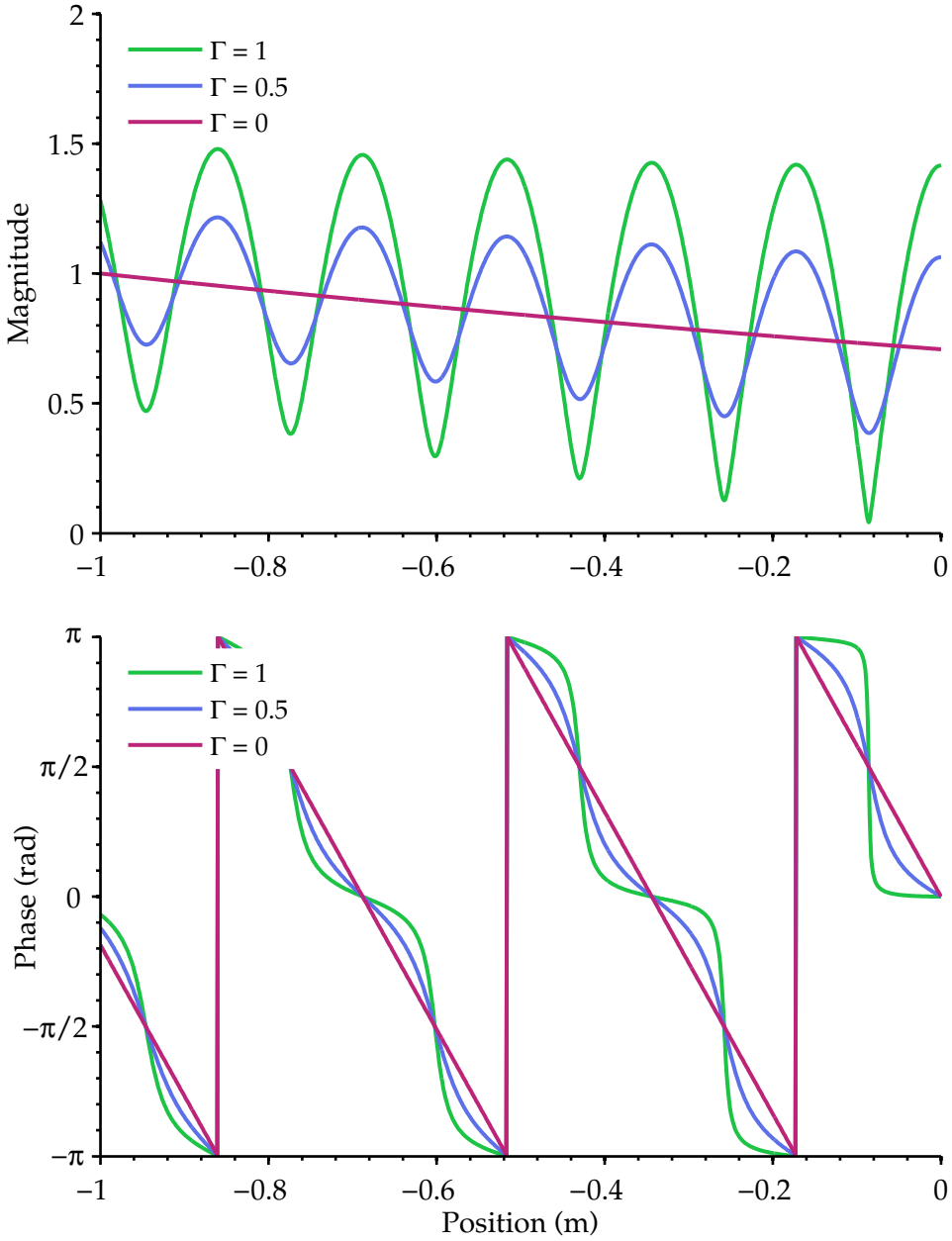

Figure 2.3: Theoretical standing wave pattern at 1 kHz with an attenuation of 3 $^{dB}/_{m}$.

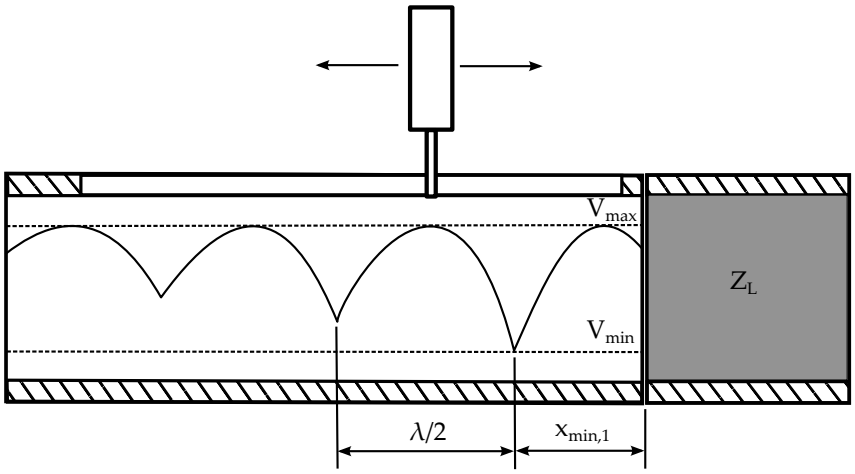

Figure 2.4: Diagram of the slotted line method. The measurement probe can be seen at the top which can traverse within the slot. An example of the amplitude of a standing wave is shown inside the impedance tube.

probe to be inserted and traversed to different positions of the waveguide, as shown in Figure 2.4. The measurement probe is moved along the slot to find the maxima and minima of the standing wave pattern. Once a maxima or minima is found, the magnitude and the position measurement are recorded. The voltage standing wave ratio can then be calculated, and in turn the magnitude of the reflection coefficient, given,

$$\text{VSWR}=\frac{|V_{max}|}{|V_{min}|}=\frac{1+|\Gamma|}{1-|\Gamma|}. \tag{2.7}$$

The phase component of the reflection coefficient is

$$\angle\Gamma=\frac{4\pi}{\lambda}x_{min,1}-\pi \tag{2.8}$$

where $x_{min,1}$ is the distance to the first minimum from the DUT.

A similar method exists in the acoustic domain—the traversing-microphone method.

Traversing-Microphone Method

The traversing probe microphone method was commonly used to determine the acoustic impedance of a load. It required the use of a capillary tube inside the impedance tube which was moved along the axis to find maxima and minima, while reading the amplitude and position of the microphone. Figure 2.5 shows a diagram of the traversing microphone setup.

The reflection coefficient is determined in the same manner as the slotted-line

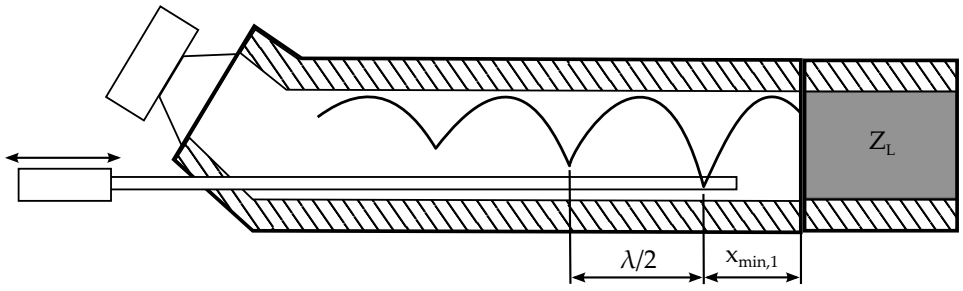

Figure 2.5: Diagram of the traversing microphone setup. The probe microphone can move back and forth to measure different points of the standing wave.

method with equations 2.7 and 2.8.

The method suffers from error caused by the probe microphone interfering with the wavefield inside the impedance tube. Measurements are also slow and tedious as they must be made manually, one frequency at a time.

2.3 Multi-microphone Method

An alternate approach to the laborious earlier methods is to have multiple microphones fixed in different positions along the impedance tube and try to reconstruct the standing wave pattern from this information. This was all made possible by the advancement of digital-to-analogue converters and microprocessors to remove most of the manual aspects of measurement. A DUT could simply be attached to the measurement port and the computer could quickly step through each of the frequencies in a wide range and calculate the reflection coefficient.

The concept sounds promising but the difficulty lies in determining the standing wave pattern with only limited arbitrary measurement positions, whereas the earlier methods sought for measurements at the optimum positions.

The two-microphone method, as the name suggests, only uses two fixed microphones. It has become a commonly used instrument for measuring the acoustic impedance of materials and lumped-element networks since the 1970s [16].

In equation 2.5, the wavenumber, $\mathbf{k}$; position, x; and the pressure, $\mathbf{p}$, are all known, the unknowns are the complex amplitudes of the travelling waves, $\mathbf{A}_i$ and $\mathbf{A}_r$. It is therefore theoretically possible to reconstruct the standing wave pattern with complex measurements with only two different positions, so long as the sound pressure measurements are unique.

The simultaneous equations for the measured sound pressures, $\mathbf{p}(x_1)$ and $\mathbf{p}(x_2)$,

at two measurement positions, x_1 and x_2, are:

$$\mathbf{p}(x_1) = \mathbf{A}_i e^{jkx_1} + \mathbf{A}_r e^{-jkx_1} \tag{2.9}$$

$$\mathbf{p}(x_2) = \mathbf{A}_i e^{jkx_2} + \mathbf{A}_r e^{-jkx_2} \tag{2.10}$$

This can be expressed in matrix form:

$$\begin{bmatrix} e^{jkx_1} & e^{-jkx_1} \\ e^{jkx_2} & e^{-jkx_2} \end{bmatrix} \begin{bmatrix} \mathbf{A}_i \\ \mathbf{A}_r \end{bmatrix} = \begin{bmatrix} \mathbf{p}(x_1) \\ \mathbf{p}(x_2) \end{bmatrix} \tag{2.11}$$

Solving for $\mathbf{A}_i$ and $\mathbf{A}_r$ by inverting the left most matrix and applying to both sides:

$$\begin{bmatrix} \mathbf{A}_i \\ \mathbf{A}_r \end{bmatrix} = \begin{bmatrix} e^{jkx_1} & e^{-jkx_1} \\ e^{jkx_2} & e^{-jkx_2} \end{bmatrix}^{-1} \begin{bmatrix} \mathbf{p}(x_1) \\ \mathbf{p}(x_2) \end{bmatrix} \tag{2.12}$$

The reflection coefficient can then be calculated:

$$\Gamma = \frac{\mathbf{A}_r}{\mathbf{A}_i} \tag{2.13}$$

The reliance on only two microphones causes any errors in the pressure measurements to become magnified when the reflection coefficient is calculated.

The multi-microphone method extends the same principles used in the two-microphone method, however by adding additional measurement positions allows for increased precision in determining the standing-wave parameters. The additional microphones can also allow for more parameters, such as attenuation, to be included into the standing-wave model to further increase accuracy.

2.3.1 Numerical Fit

The use of more measurement positions means that the series of simultaneous equations becomes over-determined. The best solution is to use all the data with a least-squares fit.

Matrix algebra is used to fit the standing-wave pattern to the measured data by allowing the non-linear solver to vary the magnitude and phase of the forward and reverse waves while attempting to minimise the least-squares error between the measured $\mathbf{p}_{meas}$ and fitted data $\mathbf{p}_{fit}$. The fitted data points are generated using

$$\mathbf{p}_{fit} = \mathbf{A}_i e^{jkx} + \mathbf{A}_r e^{-jkx}. \tag{2.14}$$

The real and imaginary components of the error term is calculated by

$$\text{err}_{\text{re}} = \Re(\mathbf{p}_{\text{fit}} - \mathbf{p}_{\text{meas}}) \tag{2.15}$$

and

$$\text{err}_{\text{im}} = \Im(\mathbf{p}_{\text{fit}} - \mathbf{p}_{\text{meas}}). \tag{2.16}$$

The total error term is then calculated by

$$\text{err}_{\text{total}} = \frac{\text{err}_{\text{re}}^2 + \text{err}_{\text{im}}^2}{\frac{|\mathbf{p}_{\text{fit}}|+|\mathbf{p}_{\text{meas}}|}{2}}. \tag{2.17}$$

Equation 2.17 is designed so that the calculated error for each microphone is normalised by the mean of the measured and fitted magnitudes. This prevents the fitting algorithm from biasing towards the large magnitude measurements—instead favouring the more important anti-nodes. The fitting algorithm is run individually for each step in the frequency sweep to determine the travelling waves and in turn the acoustic impedance of the load. Refer to appendix F.2 for a detailed description of the fitting algorithm.

Numerical Fit Verification

Ideal synthetic measurement data is fed into the numerical fit program to verify that the fitting algorithm is behaving correctly. The expected measured pressures at six positions when a load of infinite impedance is attached to the end of the impedance tube. Figure 2.6 shows the calculated reflectivity which should theoretically be unity. The deviation from unity below 100 Hz is because the wavelengths are so large that only a small proportion of the standing wave pattern is measured.

A further test is to add noise to the data to simulate potentially noisy microphone signals and check that the fitting algorithm converges to realistic values. Figure 2.7 shows the same test as Figure 2.6 but with 10% noise added to the data. The fitting algorithm produces a result that has on average less than 10% error which indicates the theory and fitting algorithm are working as expected.

2.4 Hardware

The hardware implementation of the theory is shown in Figure 2.8. An impedance tube with multiple microphones are positioned along the length of the tube. A sound driver is connected to one end and a coupling flange on the other. The loud speaker is driven by a 40 W audio amplifier, with the VNA supplying the waveform signal. A PC is interfaced with the VNA to control the input and output signals. The

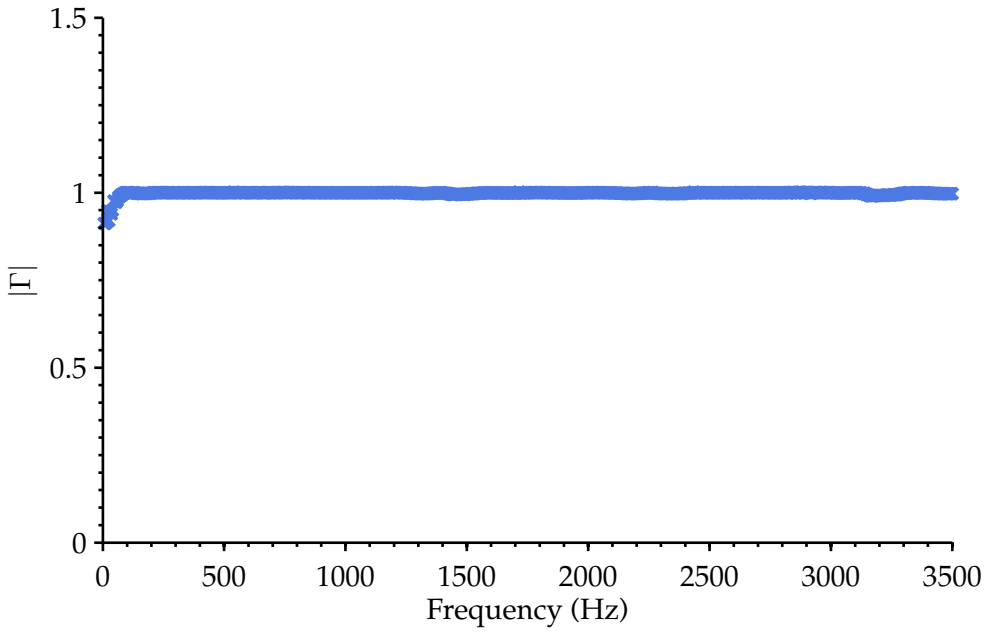

Figure 2.6: Reflection coefficient produced with the fitting algorithm on synthetic data.

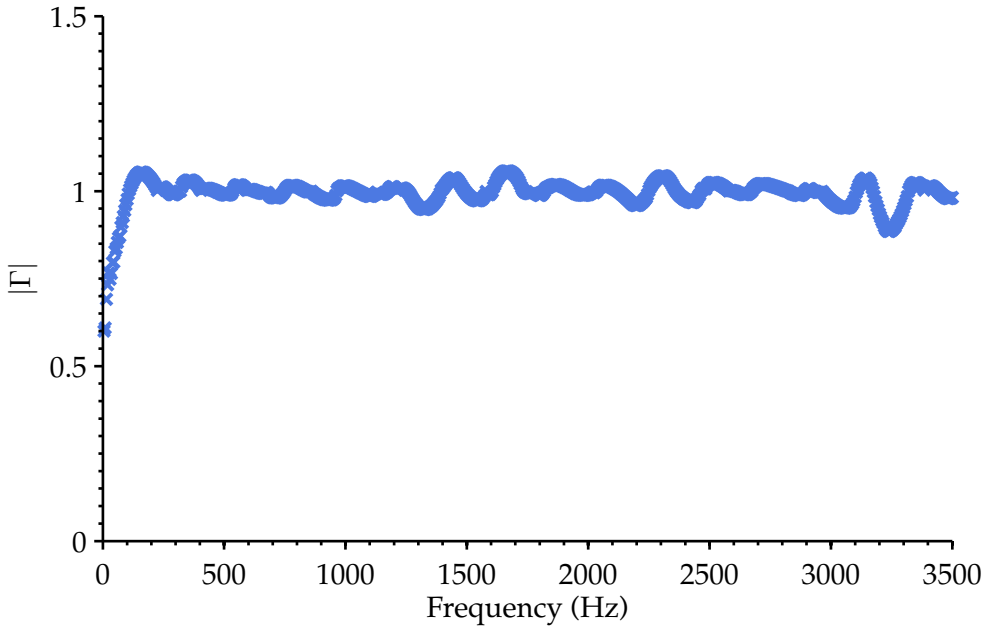

Figure 2.7: Reflection coefficient produced with the fitting algorithm on synthetic data with 10% noise.

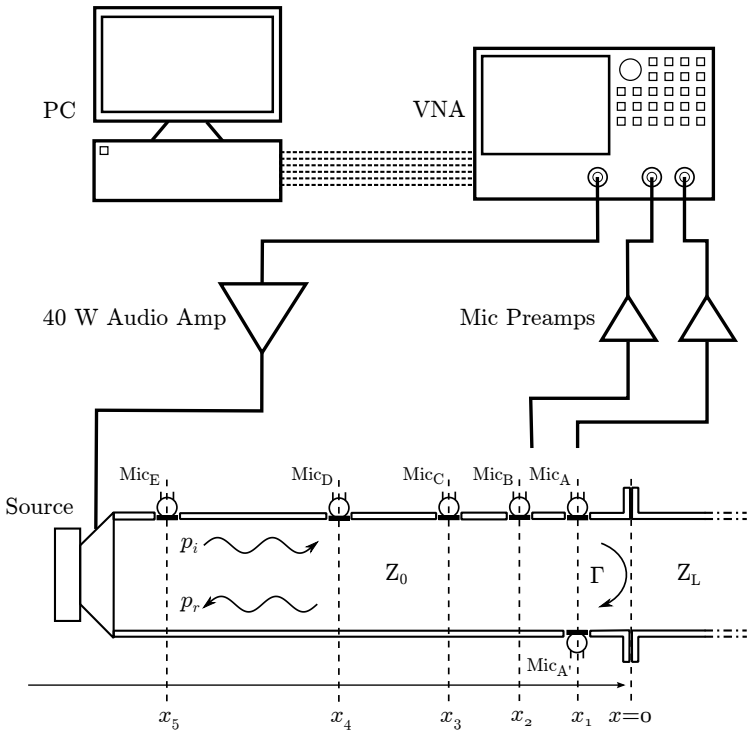

Figure 2.8: Block diagram of the hardware used in the impedance tube method.

VNA is also used to measure magnitude and phase of the microphones, which are buffered by microphone preamplifiers.

The realisation of the multi-microphone impedance tube is shown in Figure 2.9.

2.4.1 Impedance Tube

The impedance tube is the heart of this measurement system. Sound waves travelling inside of the impedance tube must be isolated from the outside world and any interference from the measurement equipment must be minimised. For this reason, the material and structure of the impedance tube must be selected carefully. Ideally, the material should be rigid with a smooth, uniform surface to allow for plane sound waves to travel normal to the wall with minimal interference. A large proportion of the attenuation of the sound waves is caused by the surface of the impedance tube. The impedance tube used in this instance was chosen to be PVC pressure piping for its rigidity, availability, and ease of machining.

The impedance tube must be airtight to ensure the measured sound pressure is correct. Air leaks can cause attenuation, reflections due to a change in impedance, and high frequency noise. Points that are vulnerable to air leaks are around the load and loudspeaker connection flange and the microphone ports. Both of these areas were fitted with lubricated o-rings to prevent air leaks by applying pressure with

Figure 2.9: Photograph of the multi-microphone impedance tube. This revision has six microphones in five unique positions. The source is shown on the left end of the impedance tube and the coupling interface for the load on the right end.

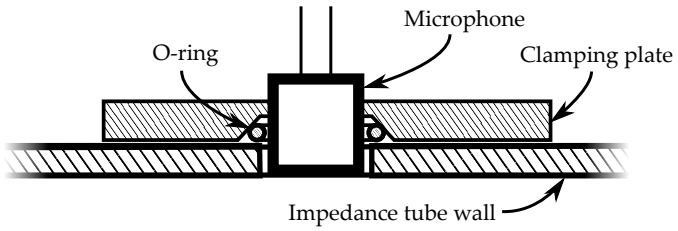

Figure 2.10: Drawing showing the cross-section of microphone port with the impedance tube. The microphone is flush with the impedance tube wall and the o-ring prevents air leaks from within the tube.

the clamping plate, shown in Figure 2.10. The implemented build design is shown in Figure 2.11. The flange also has a built in o-ring and a corresponding groove on the mating face, a photograph of the coupling flange seal is show in Figure 2.12.

The inner diameter d of the tube determines the upper frequency limit f_u of the system. This is to prevent non-plane wave mode propagation from occurring, which would interfere with the measurement of the plane waves.

ISO 10534-2:2001 [33] states that for circular tubes, the upper frequency limit is

$$f_u = \frac{0.58c}{d}. \tag{2.18}$$

Therefore, the 50 mm PVC tube used in this setup has an upper frequency limit of 4.0 kHz.

The lower frequency limit f_l of the system is dependant on the microphone

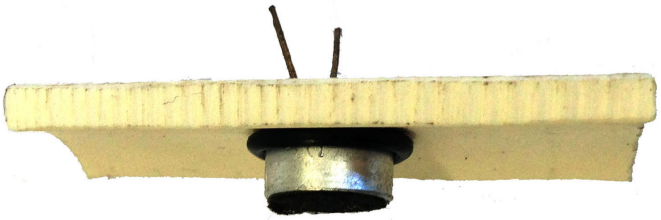

Figure 2.11: Photograph of microphone seal.

Figure 2.12: Photograph of the coupling flange and seal.

Microphone	A	A′	B	C	D	E
Position (m)	-0.100	-0.100	-0.145	-0.213	-0.381	-0.803

Table 2.1: Microphone x-axis positions from the impedance tube coupling interface used for the multi-microphone method.

spacing distance and phase detection resolution of the acquisition equipment. The system is most accurate when the spacing between the microphones is a quarter of a wavelength and their position lies on a node and an anti-node on the standing wave pattern. At longer wavelengths, the system extrapolates two measurement points that are relatively close together which causes any inaccuracies in the measurement to be exaggerated when the standing wave pattern is reconstructed. If a minimum distance of 5% of a wavelength is allowed between microphones then the impedance tube apparatus with a microphone spacing of 0.703 m allows for a lower frequency limit of 24 Hz.

2.4.2 Microphone Positioning

Given the upper and lower frequency limits of the system, the working frequency range is over seven octaves. The accuracy of measurements within this range are however not all usable with only two microphones. The standing wave pattern is cyclic and repeats every half wavelength, therefore at wavelengths where the microphones are a half wavelength apart the microphones are measuring the same point in the waveform. The reduction of information from the duplicate measurement causes the fit to be unsuccessful. The microphone positions were chosen to minimise this effect by choosing positions where the distance between the microphones are not multiples of each other.

The chosen positions of the microphones are given in table 2.1. In this configuration, microphones 1 and 2 have the same x-axis position, but are on opposite sides of the impedance tube. The purpose of this is to check that the two microphones are measuring the same sound pressure level (SPL). If there are abnormalities in the system the sound waves may not longer propagate in solely the x-axis which can be detected by these microphones. The two microphones also increase confidence of the measurement at the first position.

From the chosen positions the strength of the measurement at a particular frequency can be determined by knowing where the measurement positions will lie on the waveform. From this information a confidence of the measurement system can be calculated at a given frequency and microphone positions. The confidence in the measurement due to the chosen microphone positioning is shown in Figure 2.13.

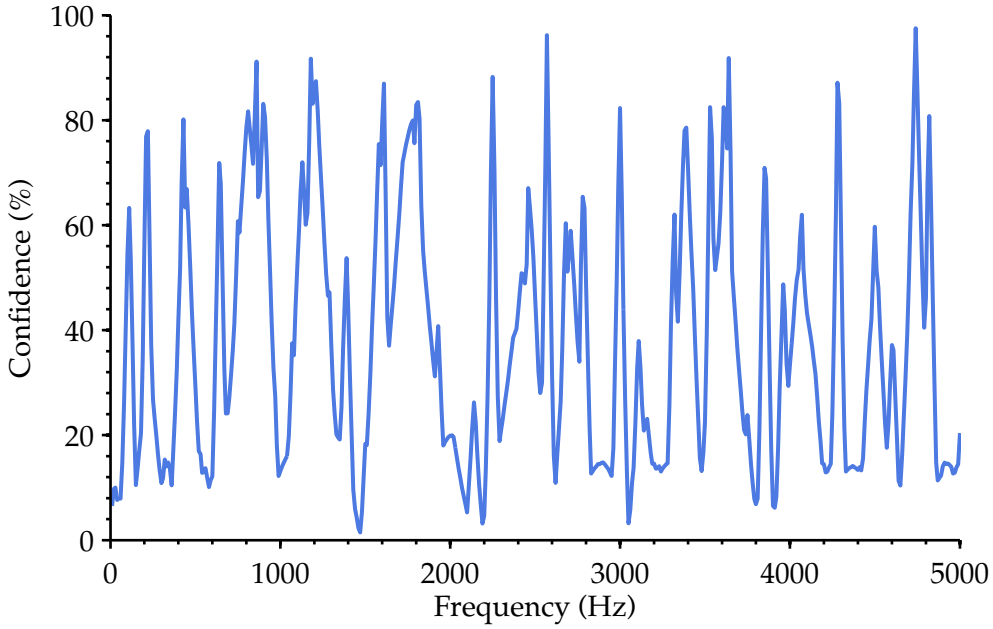

Figure 2.13: Theoretical accuracy of the system due to microphone positioning. The simulation is for a perfect acoustic short with zero phase shift. The additional microphones increase the proportion of useful working frequency range.

The confidence is representation of the microphone positions where a confidence of 1 is where the microphones are in ideal positions and 0 when they are all measuring the same point in the waveform.The Figure shows that even with 5 unique microphone positions the confidence still drops below 20% at various frequencies. The calculation code is available in appendix F.1.

2.4.3 Loudspeaker

A Visaton FRS 5 50 mm 5 W full-range loudspeaker is used as the source transducer. The driving signal is from the 50 Ω output on the 4395A which requires an audio amplifier to drive the 8 Ω loudspeaker. This function is performed by a 50 W high-performance audio power amplifier[1] based on the LM3876T [71], which has a 0.1% THD from 20 Hz to 20 kHz.

2.4.4 Microphones

Electret condenser microphone capsules[2] are used to measure the sound pressure in the impedance tube. The electret microphones require a voltage bias to operate, so

[1] A more detailed description and schematic of the amplifier is presented in appendix E.2.
[2] AM4011: A 10 mm capsule with a operating frequency range of 50–12500 Hz.

they were interfaced to the 4395A via a custom op-amp pre-amp circuit[3]. The circuit amplifies the input to near the full scale input of the VNA.

Consideration must also be given regarding the size and shape of the microphone. The microphone should have minimal interference with sound travelling down the impedance tube. To accomplish this, the face of the microphone is flush mounted with the wall of the impedance tube. The width of the face can also be important to the system's ability to measure high frequencies because the pressure across the face of the microphone in most cases will not be uniform, the microphone measurement is an average of the sound pressure across the microphone face. Therefore, the width of the face must be much smaller than the wavelength of interest, ideally of infinitesimal width to achieve the greatest resolution. The 10 mm capsules are 12% of the wavelength at the maximum cut off frequency of 4 kHz which is allowable but some loss of resolution is expected.

2.4.5 Acquisition

An Agilent 4395A network/spectrum/impedance analyser is used for data acquisition. The 4395A is connected to a PC via a GPIB interface with custom C# software. A network analyser was used for its superior magnitude and phase measurement accuracy of ± 0.05 dB and ± 0.3 deg, respectively [72].

The reference port (used as the reference signal for phase measurement) of the VNA was connected to a split from the oscillator output.

One difficulty of using a VNA is that only two ports can be connected at a time. Furthermore, the VNA only measures one port at a time which can cause issues if the test environment changes between each microphone measurement. Further details are presented in appendix F.3.

2.5 Measurement Technique

The VNA only has two measurement ports which are read sequentially. The measurement connections to each microphone must be shifted to the next microphone after each measurement in order to measure all six microphones.

Typically when making RF measurements, the VNA measures directly from the coupled ports of the directional coupler meaning that measurements contain systematic error which can be calibrated out. However, when using the stand-wave method the raw measured data must undergo processing before the directional data can be obtained for error correction. The processing stages are shown in Figure 2.14 .

[3] Additional information is presented in appendix E.3.

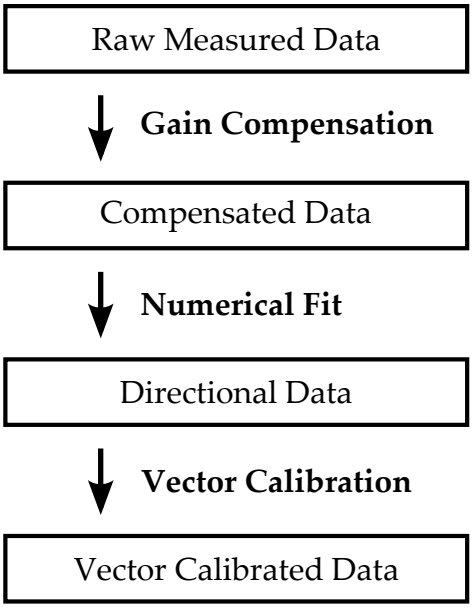

Figure 2.14: Block diagram showing the stages of calibration.

2.5.1 Gain Compensation

Although the same model of microphones are used in each of the measurement positions, they do not have identical frequency responses. Figure 2.15 shows the variation between the microphones measuring an acoustic short from the same position in the impedance tube. Microphone 2, which is in position A', is not shown in this compensation arrangement but is compensated and used later in this chapter as a means to determine if Microphone 1 was measuring correctly.

Ideally, a matched load would be measured rather than an acoustic short so that the frequency response would be relatively flat (free of nodes or anti-nodes). However, creating a matched load would require an impedance tube of infinite length, or an impedance tube with gradient of absorber in order to minimise the reflected travelling wave. An alternate method was to measure the acoustic short (for its strong repeatability) and find the relationships between the microphones using linear regression. Figure 2.16 shows the relative phase and magnitudes of the microphones when normalised to microphone 4.

After determining the normalisation matrix for the microphones, measured data can be compensated to correct the varied gains between the microphones. Figure 2.17 shows the frequency responses of the microphones after the compensation matrix has been applied. The program listing can be found in appendix F.5.

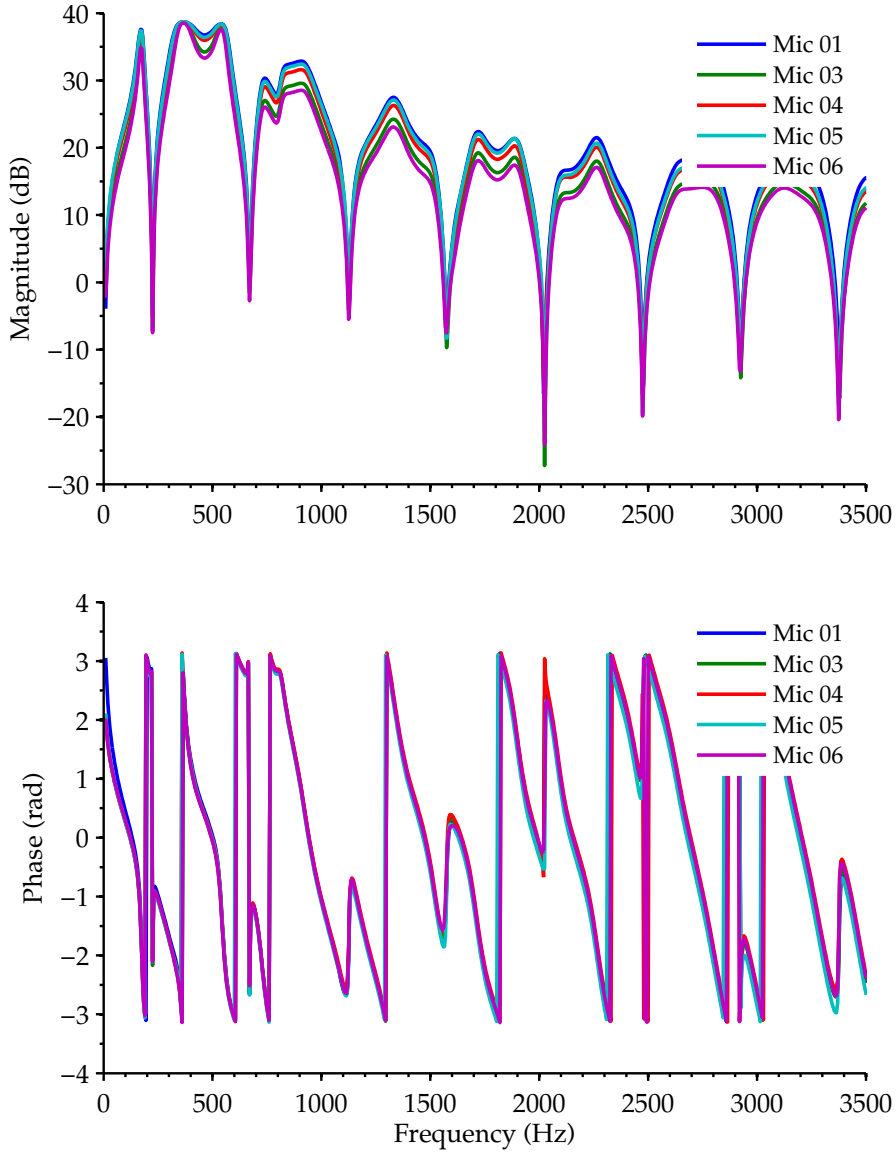

Figure 2.15: Uncompensated measurement of an acoustic short comparing the microphone responses from the same position.

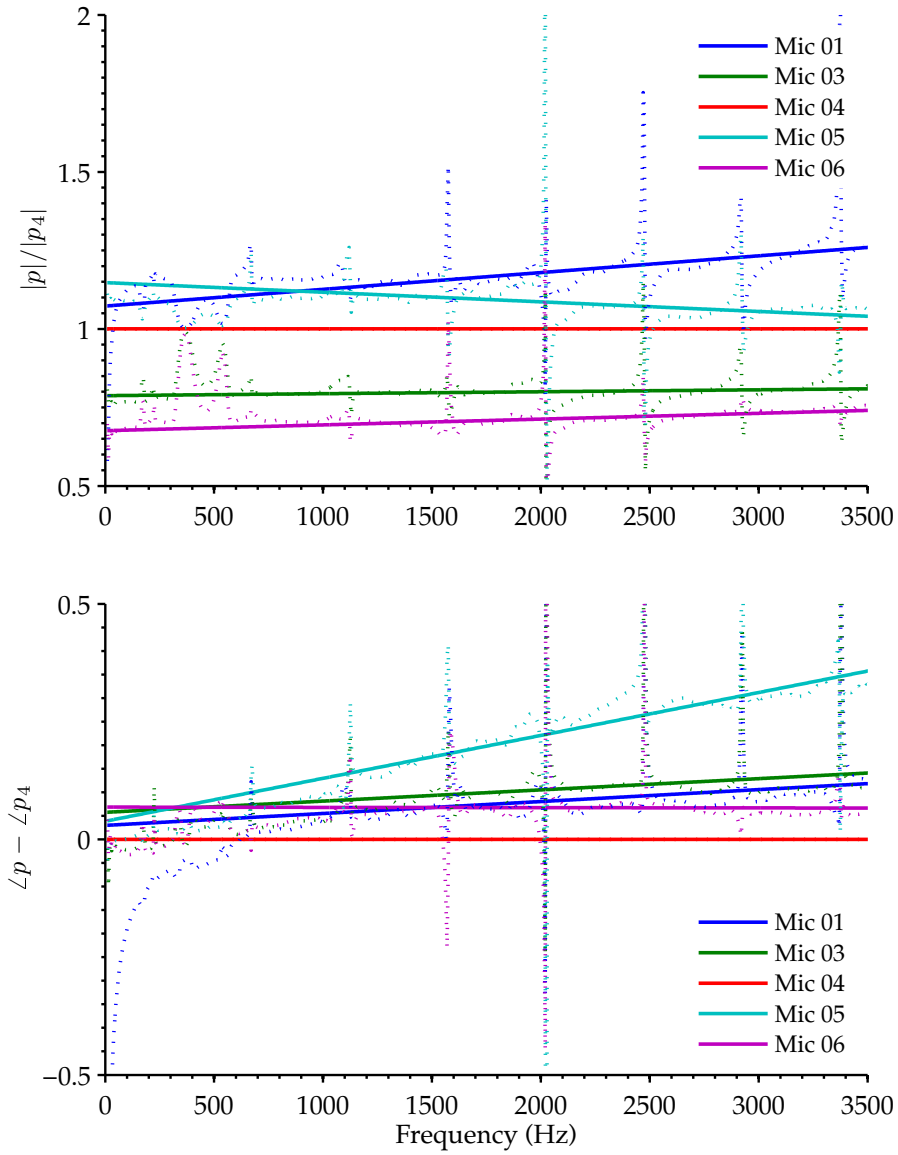

Figure 2.16: Normalisation fits of the microphones against microphone 4. The microphones gain and phase frequency dependence can be seen. The solid lines are linear fits. The dotted lines are measured data.

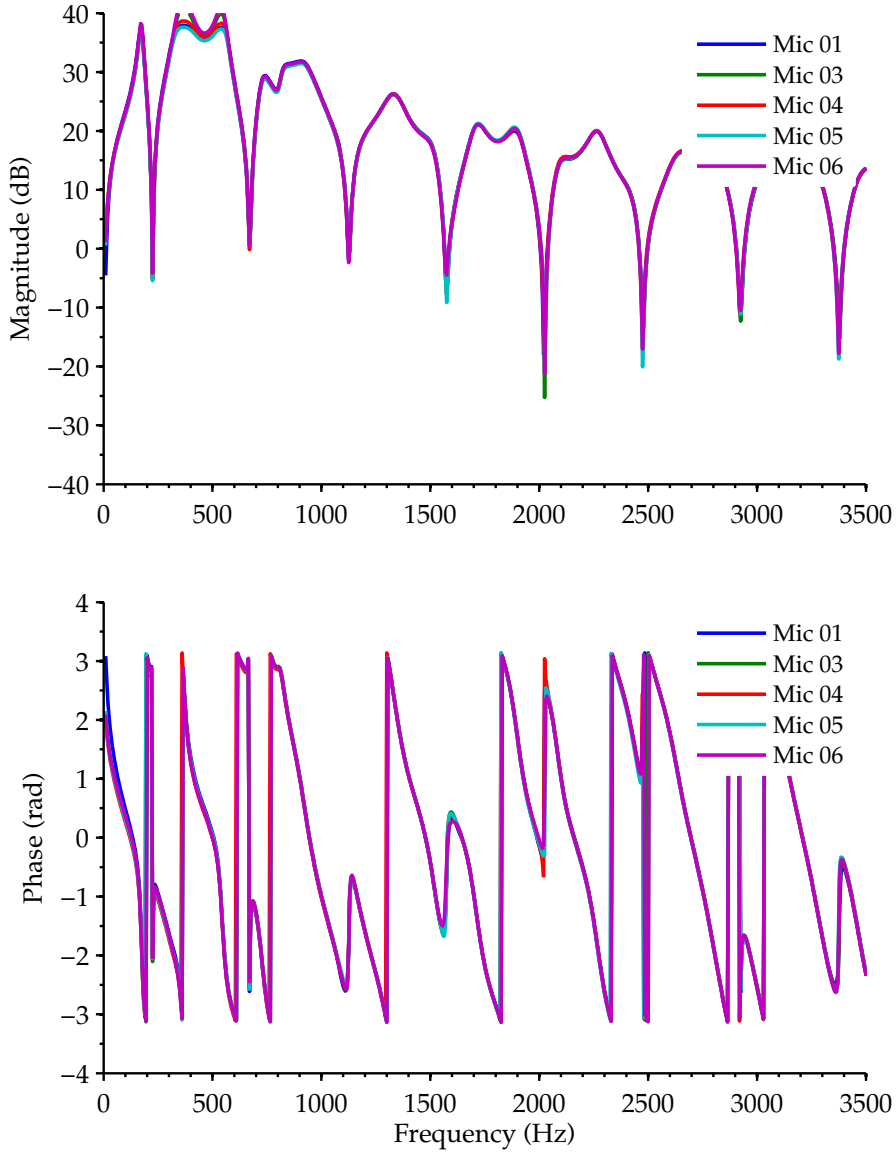

Figure 2.17: Compensated measurement data of the acoustic short. The variance between the microphones has been reduced significantly.

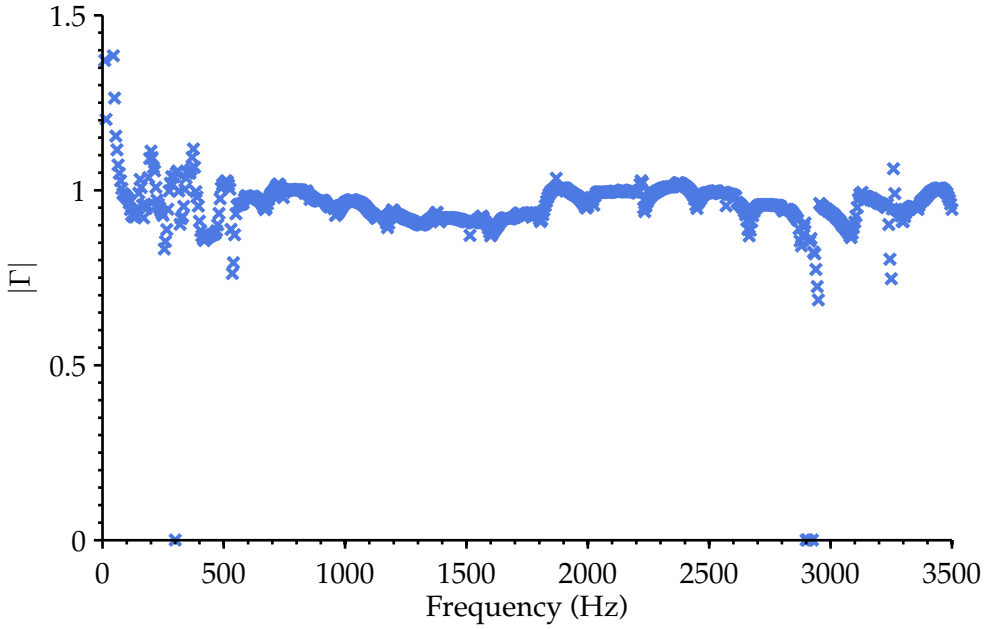

Figure 2.18: Reflection coefficient measurement of an acoustic short. The theoretical value is unity.

2.6 Measurement of an Acoustic Short

An acoustic load with known reflection properties must be measured in order to verify that the method is operating correctly. The simplest first step is to measure an acoustic structure that can be determined with physics. A perfect acoustic short when measured as a load produces a unity reflection coefficient and zero phase shift. This can nearly be achieved in reality by using a solid, smooth, dense material as a plate to seal the coupling end of the impedance tube. As previously shown in Figure 2.2, the acoustic short produces the most unique standing-wave pattern which allows for the strongest numerical fit. These are the reasons why it is used to verify this method.

The error should be less than 1% for the device to be useful for high accuracy and precision applications. Figure 2.18 shows the reflection coefficient calculated from the fitted parameters. The error below 600 Hz is quite erratic, varying $\pm 20\%$, and at 300 Hz completely failing. From 600 Hz to 2800 Hz, the error varies between 5 and 10%. Above 2800 Hz, the method again has higher than usual error and breaks down at 2900 Hz. An investigation to determine the source of the errors must take place to be able to improve the accuracy of the the measurements. A good starting point is to determine whether the numerical fit is functioning correctly.

2.7 Numerical Fit Verification

An investigation is conducted into the boundary cases of the numerical fit to gain more insight on how the fit is performing. Figure 2.19 shows the successful numerical fit of a standing-wave pattern at 600 Hz to the six measured data points. The reflection coefficient is calculated to be 0.98 which is close to the theoretical value—which seems plausible. The difference can be accounted for in the non-ideal materials and medium used. The sum of least squares fit error is -45 dB. The success at this particular frequency can be attributed to how the microphone positions happen to lie over key positions of the standing-wave pattern, namely both ends of the phase flat sections and points near the magnitude nodes and anti-nodes.

Figure 2.20 shows the numerical fit of the previously shown erroneous point at 300 Hz from Figure 2.18. The magnitude fit appears effective with a least squares error of 3.6 dB. However, the error in the fit of the phase data is apparent. If the numerical fit only considers this phase data the resulting fit is shown in Figure 2.21. The numerical fit successful determines the reflection coefficient to be 1.02.

The inconsistencies in the calculated reflection coefficients raise a few questions about the robustness of the numerical fit. Is the numerical fit correctly solving to the data or is the data not accurate enough to solve?

Figure 2.22 shows the reflection coefficients if the fit only uses the phase data and Figure 2.23 show only using the magnitude data. Comparing these with the original fit, previously shown Figure 2.18 produced with equation 2.17, it can be seen that large portions of these fits return values close to theoretical.

Figure 2.24 shows the error caused by noise added to synthetic data. It can be seen that certain frequencies are more susceptible to input error than others, due to the where the microphone positions happen to lie on the standing wave pattern. This can seen clearly in Figure 2.25 as well as the error in the results of the fitting algorithm are proportional to the magnitude of noise added to the data. We might have expected a weak algorithm to rise steeply at a point where the noise causes it to breakdown and produce erroneous results. An alternate approach would be to use a weighted combination of the magnitude and phase similar to the algorithms presented by Douglas and Mandic [73].

2.8 Investigation into Error Sources

As mentioned earlier, the wavenumber, position, and pressure must be known in order to solve the series simultaneous equations. Obtaining these values is not trivial.

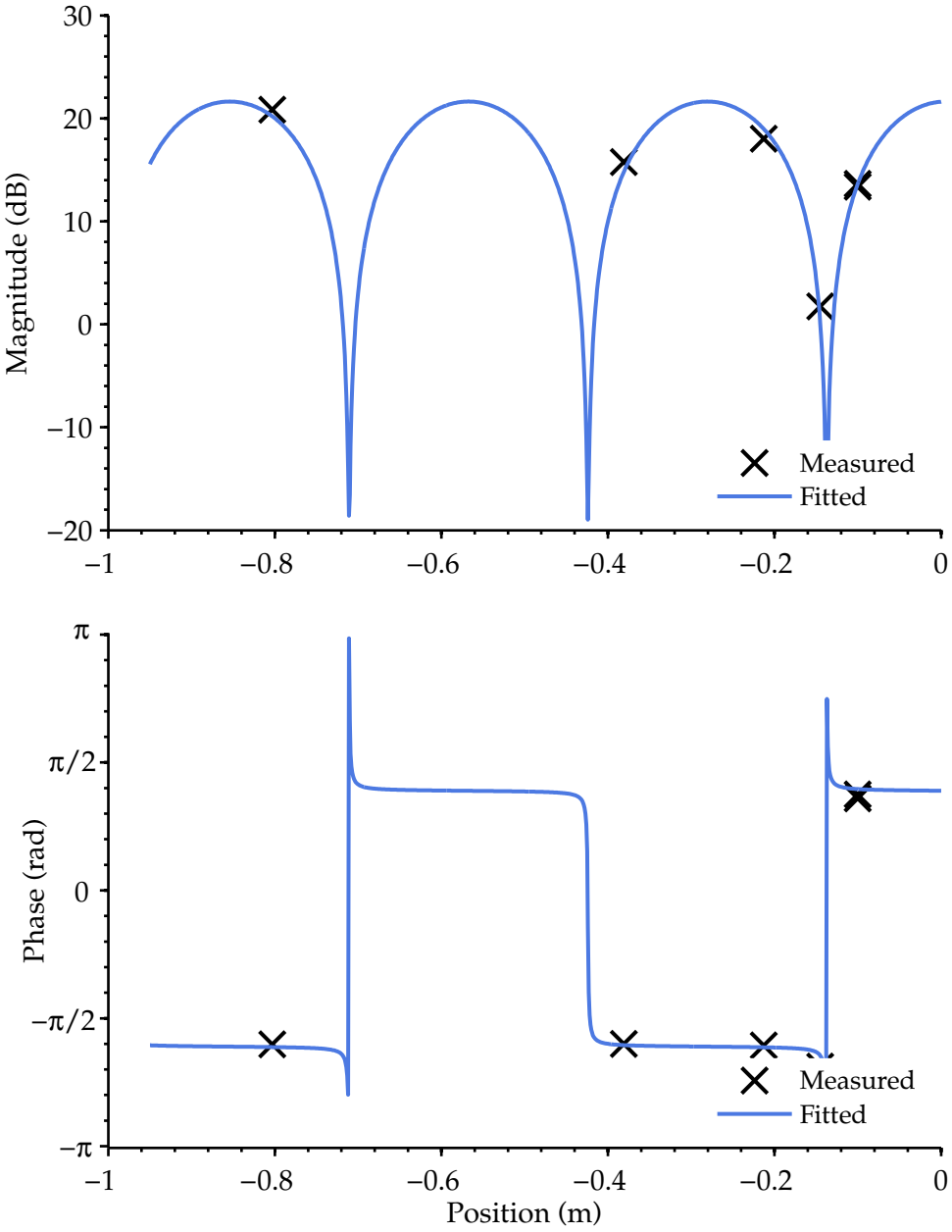

Figure 2.19: Compensated data showing an excellent numerical fit of the standing-wave pattern for an acoustic short at 600 Hz with a sum of least squares fit error of −45 dB. The fit resulted in a near theoretically ideal $|\Gamma|$ value of 0.98. The 0 x-axis position is the plane of coupling flange.

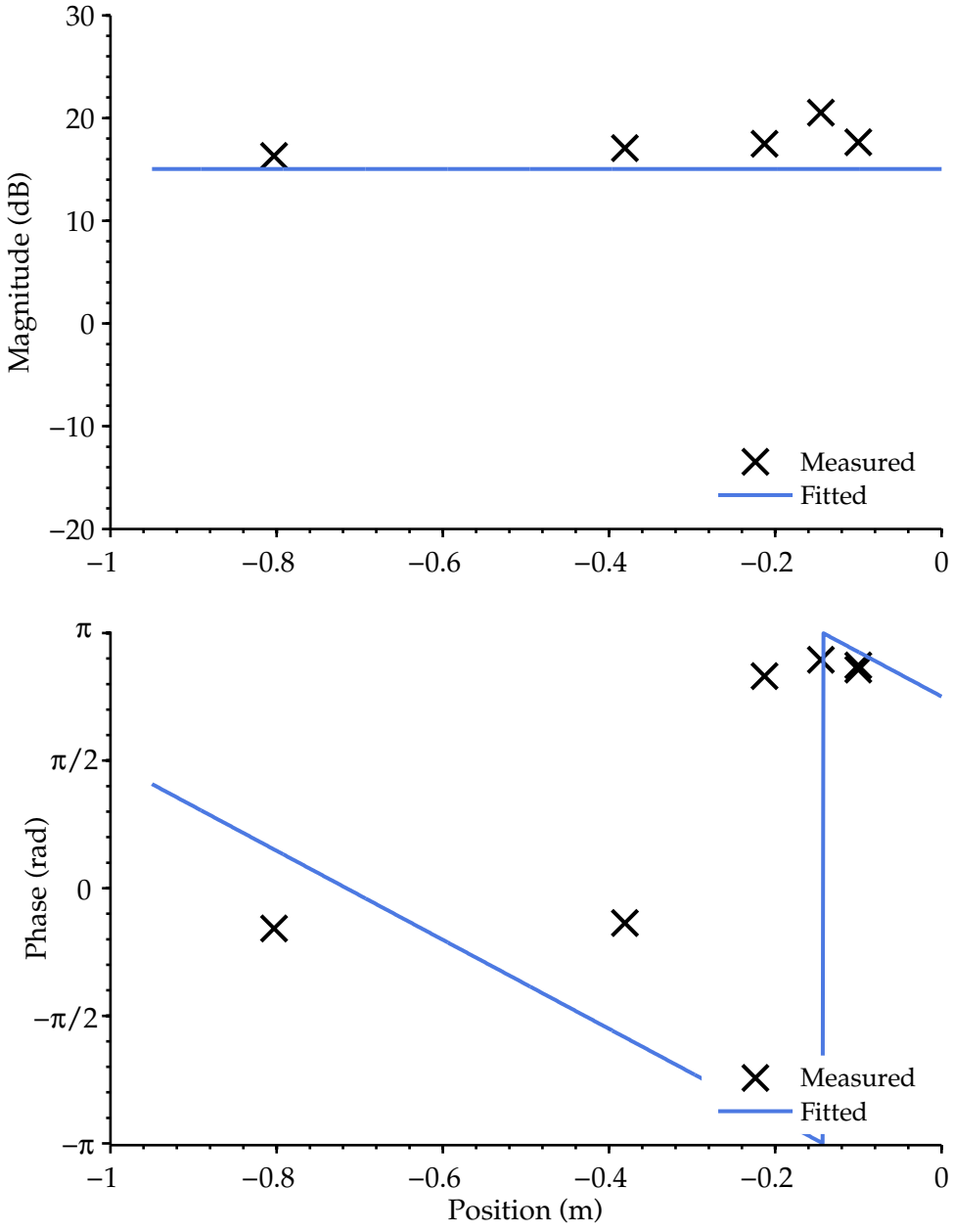

Figure 2.20: Erroneous fit of an acoustic short at 300 Hz. The resulting reflection coefficient is 0.00.

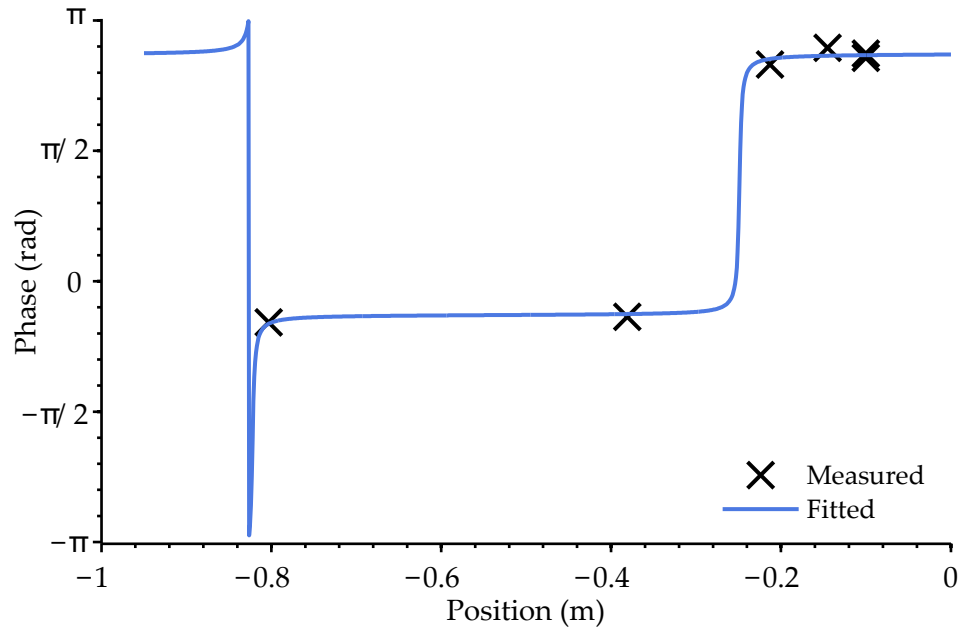

Figure 2.21: Numerical fit of an acoustic short at 300 Hz using only the phase data. The resulting reflection coefficient is 1.02.

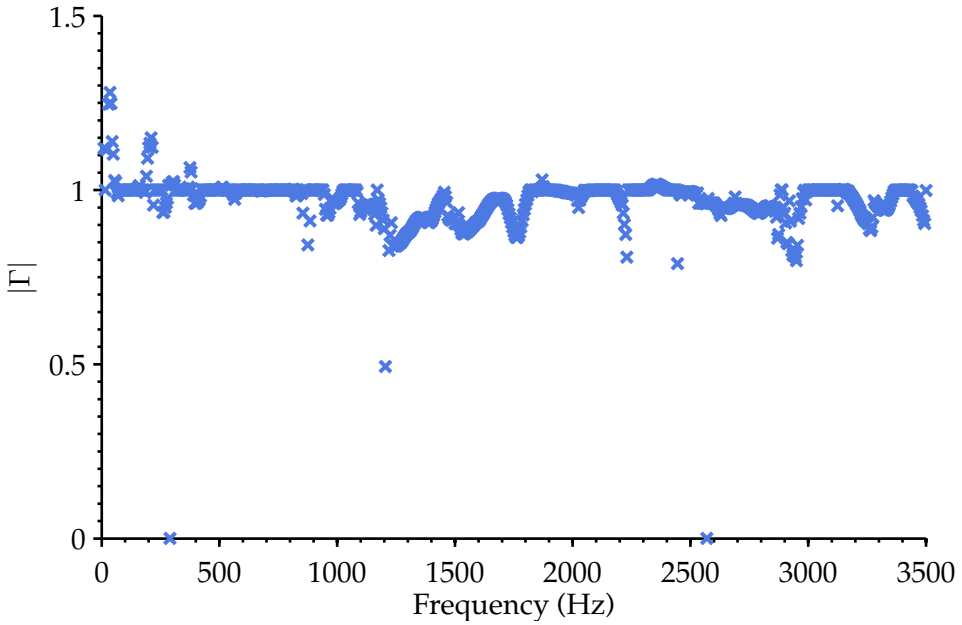

Figure 2.22: Reflection coefficient of an acoustic short only fitting to the phase data.

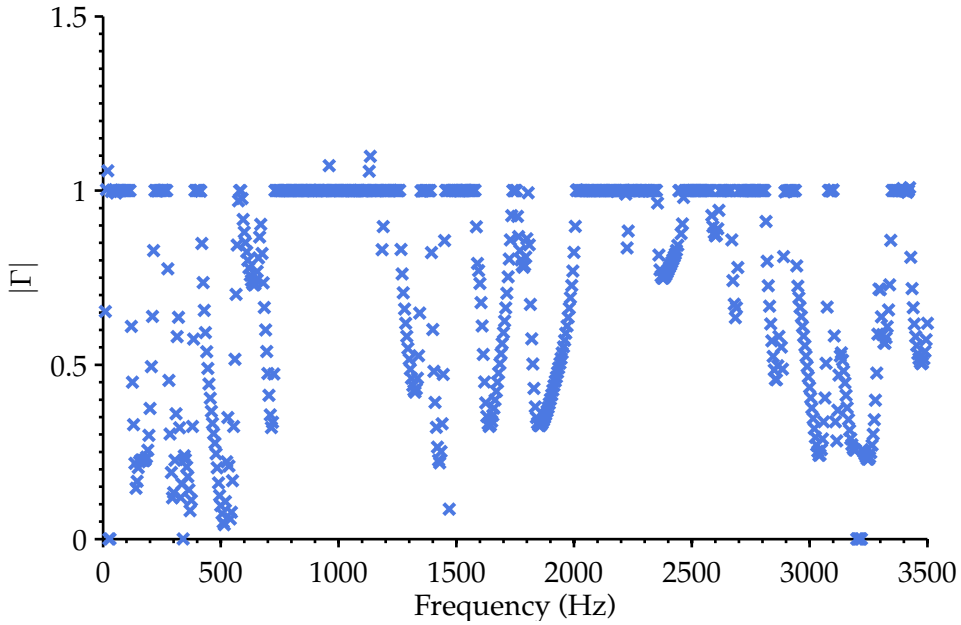

Figure 2.23: Reflection coefficient of an acoustic short only fitting to the magnitude data.

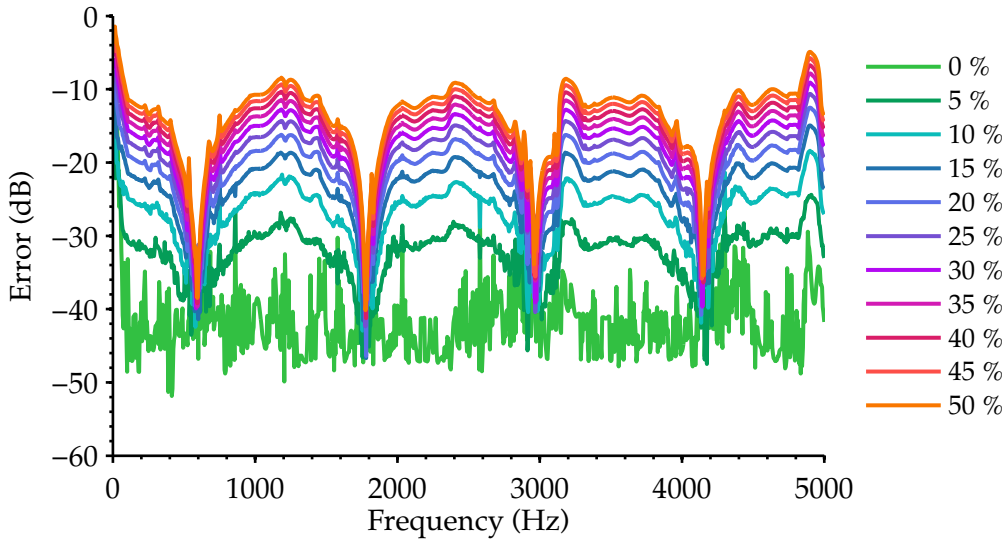

Figure 2.24: Error caused by random noise added to synthetic measurement data. The results are averaged over 1000 repetitions.

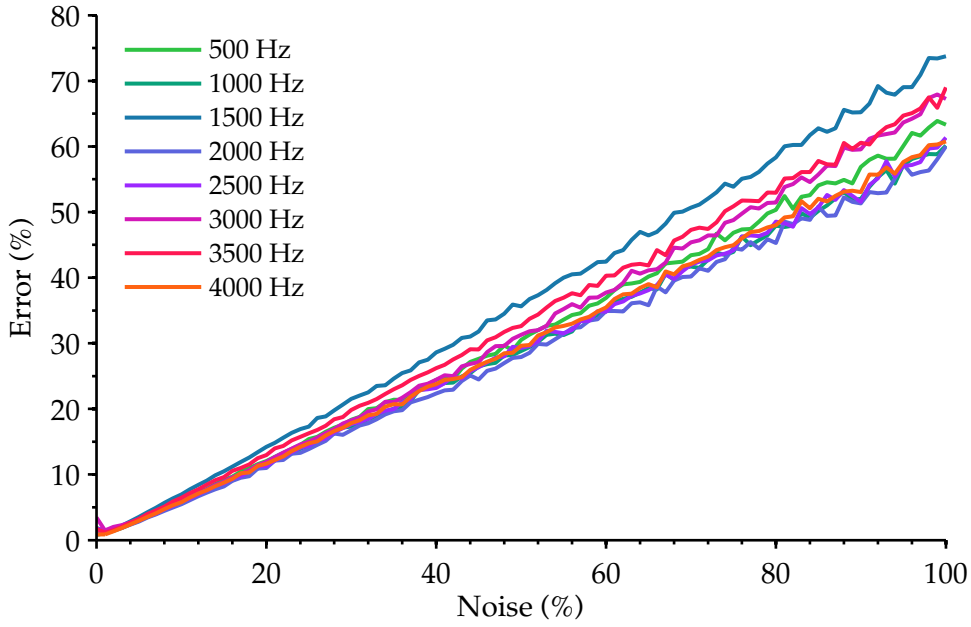

Figure 2.25: Error caused by random noise added to synthetic measurement data. The results are averaged over 1000 repetitions.

The wavenumber, shown previously in equation 2.2, is comprised of angular frequency, the speed of sound, and the attenuation.

Angular frequency is set by the signal generator (in our case, the VNA). The Agilent 4395A is specified at having a source frequency accuracy of less than ± 5.5 ppm [72].

The speed of sound in the tube is dependant of the properties of the medium (air) inside the impedance tube such that

$$c = 20.05\sqrt{T + 273.15} \tag{2.19}$$

where T is the temperature in degrees Celsius (°C). Therefore an increase in temperature from 20 °C to 25 °C causes a change of wavelength of -0.9%.

The cooling effect of the walls of the cavity can affect the impedance due to temperature fluctuations. This effect was shown to have no significant effect above 20 Hz for cavity volumes of 60 cm^3 [18]. In an air-conditioned temperature-controlled room the variation in environmental temperature was measured to be within 3°C. Local temperature variation due to energy dissipation of the equipment, mainly the loudspeaker would likely introduce a small error which is minimised by allowing the system to stabilise before measurements are made.

The attenuation of the sound waves in the impedance tube is mostly dependant on frequency, with some dependence on temperature. Determining the attenuation

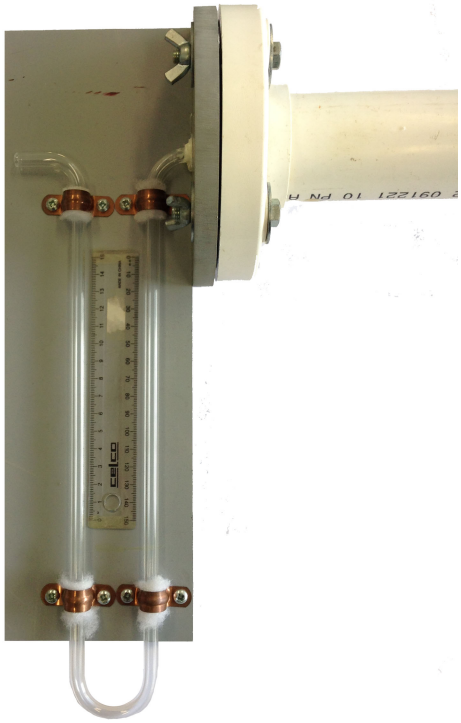

Figure 2.26: Bespoke liquid-column manometer to test the air tightness of the impedance tube.

can be performed with numerous methods. It can be determined prior to error correction measurements. It can also be determined by using more than two microphones and using the additional freedom in the simultaneous equations to solve for attenuation too.

Determining the positions of the microphones is relatively straight forward. The distance from the measurement plane (face of the coupling flange) to the centre of the microphone, although they are not known exactly due to the microphone face having a discrete size. There are some known asymmetries between the position the microphone actually measures and the physical location [74].

The seals and airtightness of the impedance tube were tested with a custom made liquid-column manometer, shown in Figure 2.26. A DC signal was applied to the loudspeaker and the pressure within the impedance tube was shown on the manometer. The pressure was slow to subside indicating the tube was well sealed.

Figure 2.27 shows the microphone and speaker stability test. The test was performed over six hours to determine the magnitude and phase variance over time. The magnitude was found to vary by -39 dB. This cyclic effect is most likely caused by the air-conditioning switching on and off in the laboratory which would vary the ambient temperature within the range discussed earlier. Further room temperature

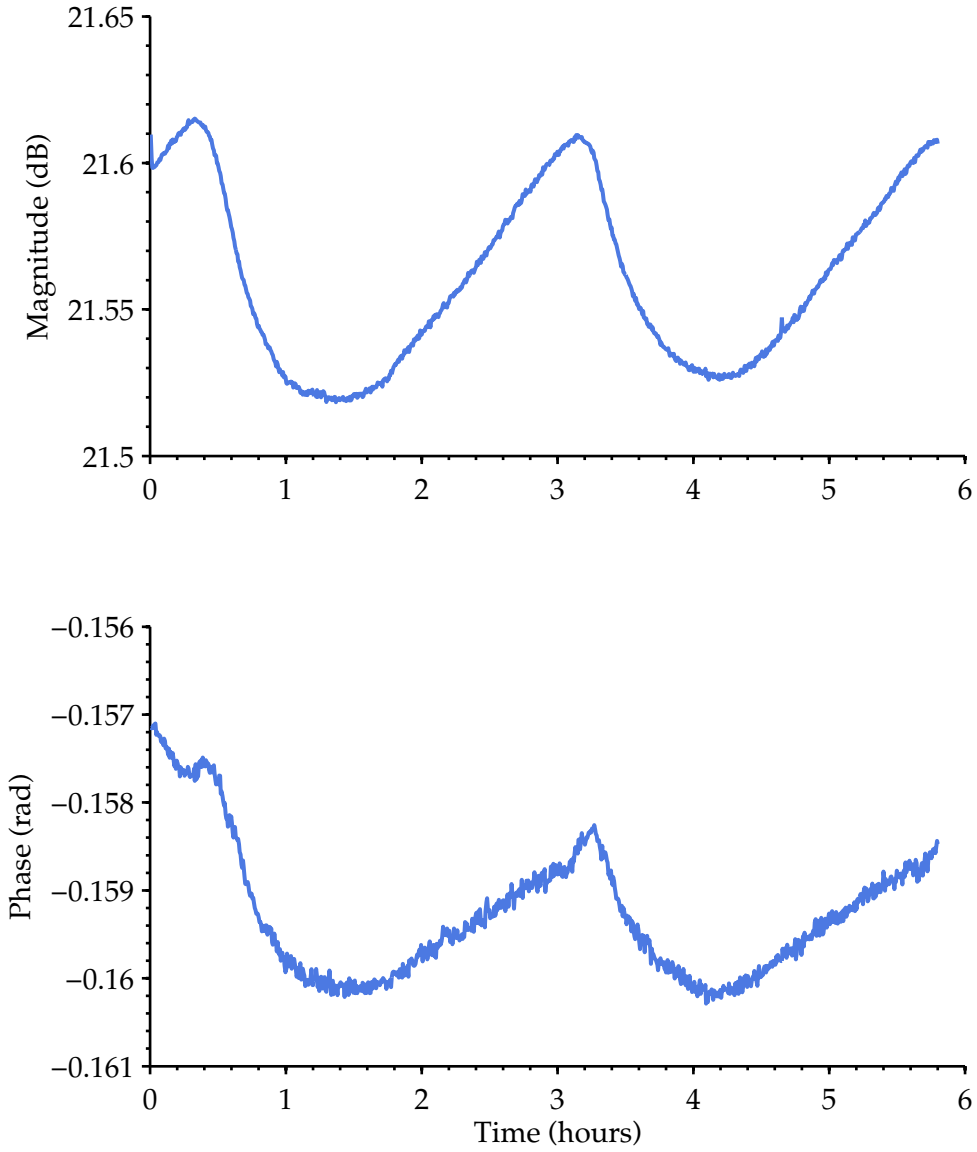

Figure 2.27: Microphone and loudspeaker stability test. The loudspeaker was driven with a 2 kHz signal over six hours.

control would be unfeasible for this project but temperature compensation could yield marginal gains.

2.9 Conclusion

The investigation into the cause of the error shows that determining the forward and reverse waves using multiple microphones relies heavily on the accuracy of the microphone measurements. There are many variables which affect the measurement of a microphone which are difficult to keep constant even in a controlled environment. Using a VNA in this method for the superior phase accuracy may have more drawbacks than advantages. The slow sequential data capture means that the measurement points were not taken under identical conditions.

Reducing variability would produce more accurate results but the major problem with this method is that any error in the measurement becomes exaggerated after being transformed by each of the multiple post-processing stages. The effect is that the method is unstable and only with difficulty can you achieve an accurate measurement with high precision.

3
Acoustic Directional Coupler

In this chapter an introduction to why using a directional coupler could prove successful is given in Section 3.1. The design of the system is described in Section 3.2.

3.1 Introduction

In the previous chapter we explored the multi-microphone standing-wave method as a possible system to resolve directionality, but foundit inherently contained errors which could not be corrected by calibration.An alternate method was sort, where to physically, rather than computationally, separate the travelling waves with a similar technique developed for use in the RF domain.

3.1.1 Vector Network Analyser

The VNA has become a staple of the RF industry for measuring impedance with high precision, accuracy, and repeatability since the 1960s. Two of the major features of the VNA which allow such excellent impedance measurement are the calibration routine and the directional couplers.

Of the two types of error, systematic and random, there is a large amount of systematic error caused by imperfections in the equipment and setup. This error is repeatable and proportional caused by specific features in the setup. The calibration

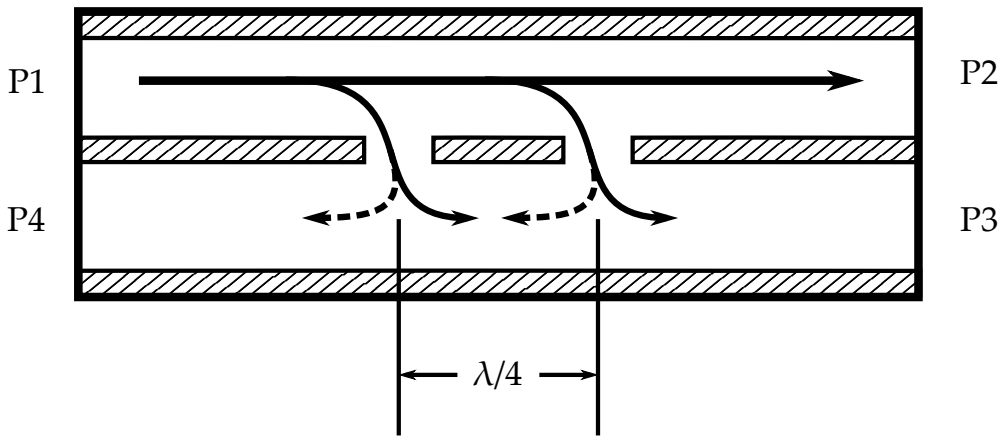

Figure 3.1: Diagram of a directional coupler. A small portion of the travelling wave propagating from P1 to P2 will only be received at P3. The waves travelling to P4 are a half wavelength out of phase and cancel.

routine involves determining the values of systematic error in a measurement and correcting for them. Further details of calibration are discussed in Chapter 4.

The second major feature is the directional couplers which link directly back to the calibration routine. The reason why these two are so well matched is that even though the directional couplers can produce a large amount of error, most of which is systematic and can be corrected by calibration. The bulk of the remaining random error in the measurements can be corrected by intelligent averaging routines.

3.1.2 Directional Coupler

The directional coupler is a device which uses constructive and destructive interference to separate a small proportion of a travelling wave depending on the direction of propagation. This is useful as the standing wave pattern does not need to be determined in order to find the magnitude and phase of the incident and reflected waves—they can be measured directly.

Figure 3.1 shows a diagram of a two-aperture directional coupler design. The key to the design is changing the distance, depending on direction, that the travelling waves must travel to reach the coupled ports. With careful selection of the distance between the apertures the directional coupler can be designed to work optimally at a specific wavelength—a proportion of the signal that is propagating from P1 to P2 arrives at P3 and none at P4. However, at other frequencies the directional coupler will not behave ideally, with more signal ending up at P4, and even at certain harmonic frequencies the directionality can completely reverse. Directivity is a measure of how well the directional coupler separates the waves to the desired

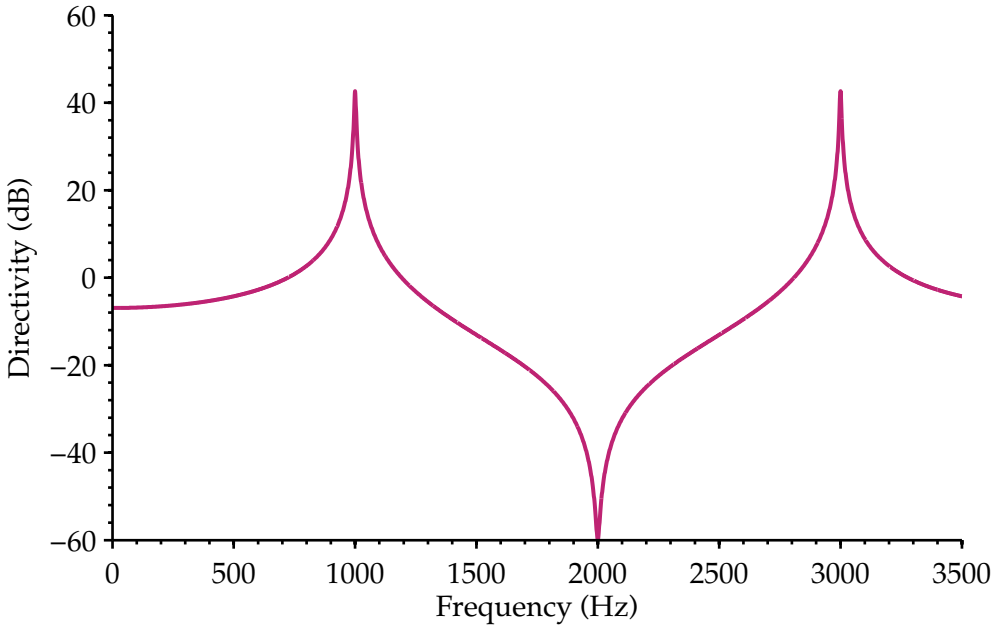

Figure 3.2: Directivity of a two-aperture coupler designed for 1 kHz.

ports i.e. $P3/P4$. The simple two-aperture design has a high directivity at the designed frequency but is reduced within an octave as shown in Figure 3.2.

The coupling factor is the measure of the proportion of the incident wave being received at the coupled port i.e. $P3/P1$. This can be tuned depending on the sensitivity of the measurement devices on the coupled ports. If more signal-to-noise is required the coupling factor can be increased to divert more power away from the main tube. Alternately, the output power of the acoustic driver can be increased, but this may lead to non-linear affects in the dampening materials due to air turbulence [75].

Typically when measuring the acoustic impedance of a material or element it is more useful to measure it at a range of frequencies in order to find minima, maxima, or just to identify trends. The narrow measurement frequencies of the two-aperature design therefore has limited use. But, the design can be adjusted to perform over a wider range of frequencies at the cost of directionality. The working range of the coupler can be widened by adding additional apertures designed to work at frequencies near the centre frequency [76]. Figure 3.3 shows directivity of a coupler with additional apertures. The amplitude of the maxima and minima have become less extreme and the directivity of the frequencies near the centre are better performing. This flattening of the directivity is the limitation of this frequency broadening technique. At a point the directionality becomes insufficient to differentiate the amplitude of the forward and reverse waves causing the method to fail. It is estimated that 15 dB of directivity is needed to resolve the magnitude

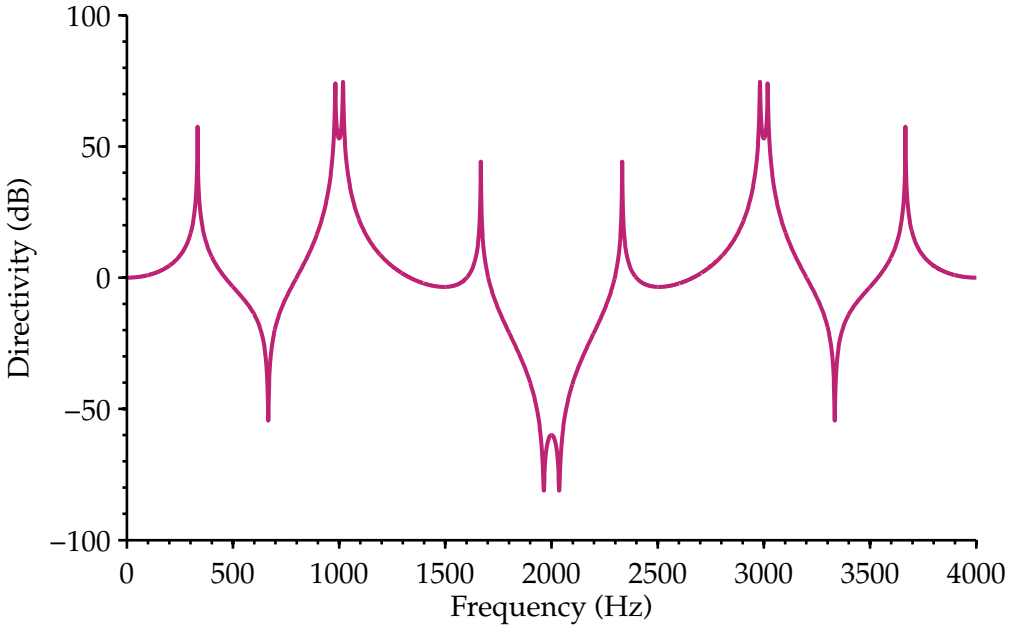

Figure 3.3: Directivity of a four-aperture coupler designed for 1 kHz with an additional coupled frequency which extends the bandwidth but also adds harmonic interference with the main channel.

and phase of the travelling waves [62].

3.2 Design

The intent of the acoustic measurement device is to characterise materials or acoustic elements over a wide range of frequencies. A proven acoustic coupler design developed by Lagasse [77] was chosen which incorporates eight branches to achieve a directivity of over 30 dB from 2250 to 4250 Hz connecting 30x30 mm waveguide, shown in Figure 3.4. A rectangular waveguide was used in this design, as opposed to the circular waveguide in the standing wave method, to simplify the mathematics of the directional coupler. The design originates from an RF directional coupler design method using Chebyshev and Butterworth polynomials proposed by Levy and Lind in 1968 [76].

The acoustic directional coupler suffers from one of the limitations previously described in subsection 2.4.1, namely the upper cut-off frequency limit is

$$f_u = \frac{0.5c}{a} \tag{3.1}$$

for square tubes, where a is the inner width of the tube, to ensure only the fundamental mode is allowed to travel in the system. The implication of this is that

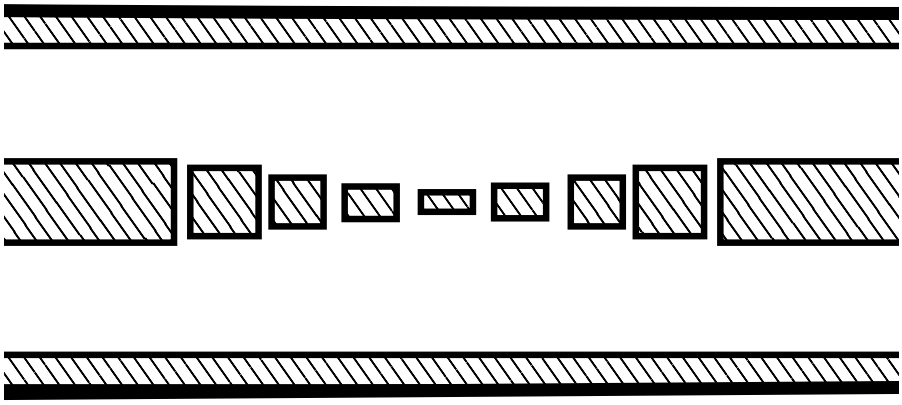

Figure 3.4: Eight branch directional coupler.

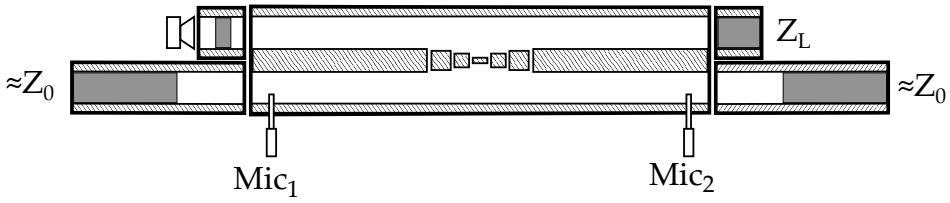

Figure 3.5: Diagram of the acoustic directional coupler hardware.

directional couplers of different widths are required to extend the working frequency range further.

The realisation of the directional coupler in a measurement system is shown in Figure 3.5, where instead of using a 30x30 mm waveguide a 60x60 mm cross-section is used. The effect of this is that the working frequency range of this design is shifted down to between 750 Hz and 2200 Hz. The acoustic directional coupler consists of two acoustic waveguides, the main line and the coupled line, connected via a series of apertures. The coupled lines have matched acoustic impedance (Z_0) terminations to prevent reflections. Any reflections would reduce the directivity of the coupler. The loudspeaker also has acoustically resistive material in front of it to minimise reflections caused by the impedance change.

3.3 Hardware

The dimensioned technical drawing is available in appendix Figure E.1. In the main line, a loudspeaker is at one end and a measurement flange at the other. Two microphones are positioned near either end of the coupled line with acoustic dampening material at the ends.

Figure 3.6: MDF directional coupler.

The initial directional coupler prototype, shown in Figure 3.6, is made from medium-density fibreboard (MDF) for the material's rigidity and ease of construction. The wooden components are wood glued and screwed in place.

Matched acoustic loads for the coupled lines were also constructed in a similar fashion, which appears in Figure 3.7. They contain triangular foam inserts to increase the attenuation and reduce reflections caused by large changes of impedance.

The microphone measurement ports are drilled to the diameter of the microphones so that they can be press-fitted in place to prevent any air-leaks or misalignment.

3.3.1 Impedance Tube

Two versions of the acoustic directional coupler were fabricated, one from MDF and another from transparent acrylic which appears in Figure 3.8. The acrylic has a flatter and less porous surface than the MDF which causes less absorption and reflections as the travelling wave passes down the tube and therefore increases transmission.

Acoustic Loads

A set of acoustic loads were also made from MDF, shown in Figure 3.9, which have precise dimensions allowing their acoustic properties to be calculated from acoustic theory. The design and purpose of the acoustic loads is detailed in 4.5.

The absorbing acoustic loads, shown in Figure 3.10, are construct out of a variety of foam densities which are more effective at absorbing sound at different frequencies.

3.4 Acquisition

Behringer ECM 8000 microphones were used with built-in preamplifiers to allow them to directly connect to the recording interface. A Presonus AudioBox 1818VSL is used as the recording interface in this system. The interface has a 24-bit ADC which can read up to 18 channels simultaneously at 96 kHz. The 1818VSL is interfaced

Figure 3.7: Matched impedance load with attenuating material inside to prevent reflections.

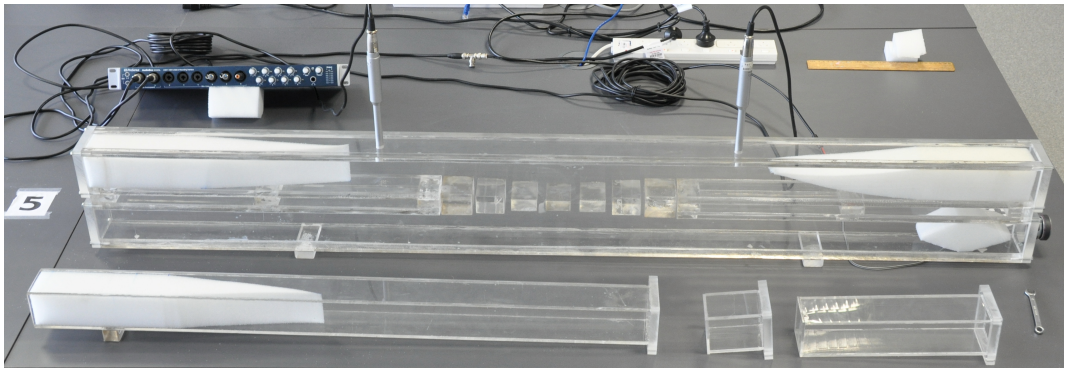

Figure 3.8: Photograph of the acoustic directional coupler fabricated from acrylic. The source is on the bottom right with the coupling end on the left. The calibration standards can be seen below. The Presonus AudioBox 1818VSL recording interface is shown to the top left.

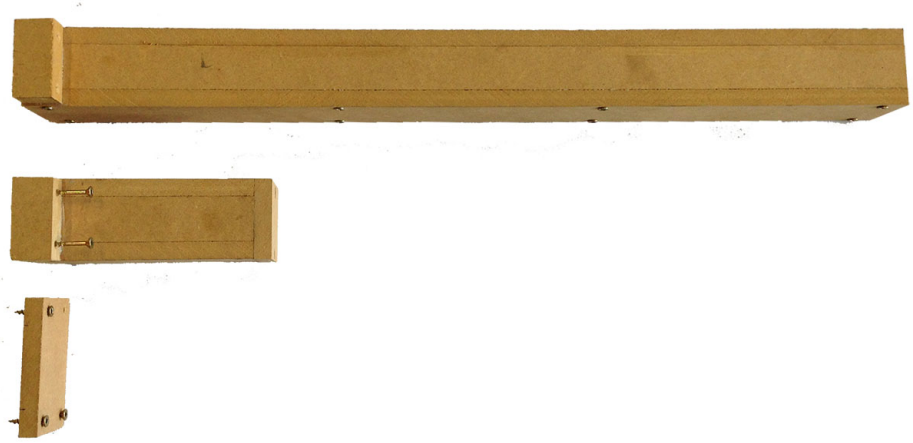

Figure 3.9: MDF acoustic loads. Top: 450 mm offset open. Middle: 150 mm offset short. Bottom: Short.

Figure 3.10: Foam wedges of different densities and lengths used as acoustic loads.

with the PC via a custom C# program designed to continuously update the input and output buffers of the recording interface. The software allows frequency sweeps to be set up with various parameters. At each frequency step a sinusoidal waveform is generated to be loaded into the input buffer of the 1818VSL to be driven by the loudspeaker. The tone is output for a settling period of 2 seconds to ensure system has stabilised, then 204,800 samples are taken over 2.13 seconds. Further details of the acquisition code are presented in appendix F.4.

3.4.1 Discrete Fourier Transform

At each frequency step there are 204,800 magnitude measurements containing random noise and other frequencies caused by the imperfect loudspeaker and impedance tubes. The measured data is cropped to fit an integer multiple of the wavelength of interest to prevent the waveform from having a discontinuity.The only data of interest is at the reference frequency used to drive the loudspeaker. In order to extract that data a discrete Fourier transform (DFT) can be applied to produce one complex value representing the magnitude and phase of the measured waveform with respect to the reference waveform. Oversampling the data by such a large factor greatly increases the accuracy of the measurement at the cost of time.

The DFT MATLAB software source code is given in appendix F.6.

3.5 Measurement

The described system is sufficient to make acoustic impedance measurements, but not with any degree of accuracy. The current measurements contains error from the imperfections in the equipment and materials. In order to achieve greater accuracy a calibration scheme needs to be designed to correct for as much of the systematic error as possible.

4
Vector Calibration

This chapter discusses the sources of error in the directional coupler method. Several error-correction algorithms and various calibration standards are developed to increase the accuracy of the acoustic impedance measurement.

4.1 Introduction

With any sort of measurement there is error in the reading which masks the true value. The key to making accurate measurements is to determine possible sources of error and develop algorithms to null these effects. The RF world has spent a sizeable amount of time and money on developing techniques for use with high frequency electromagnetic wave measurements, many of which can be used in the directional coupler method.

4.2 Error Sources

Errors within a given system can be categorised as either random or systematic.

Random error is the variation from measurement to measurement. If enough measurements are taken and averaged, the random error will tend to zero. The amount of precision a measurement system is capable of is dominated by random error. Smart methods of averaging will find the most efficient trade off between measurement time/data with degrees of precision.

Systematic error is constant each measurement, resulting in the loss of accuracy to the true value. There are many different sources of systematic error in a given measurement device, but the key aspect is that they stay the same for each measurement which allows for a procedure to be developed to measure the resulting error and correct for it.

Some of the various causes of error in impedance measurement systems and their significance are discussed in the following section.

4.2.1 Attenuation

Attenuation is the loss of sound energy as the wave travels though a medium. The energy is generally lost in the form of heat or transmitted to surrounding mediums. The attenuation of a sound wave though a wave guide is often omitted for being insignificant. However, for high precision and accuracy measurement systems each source of error must be evaluated.

4.2.2 Directivity

In a directional coupler the directivity is a measure of the ability to separate the forward signal and reverse travelling waves. In the case of a signal entering the main forward port (P1), the directivity is the ratio of signal at the coupled port (P3) to the reverse coupled port (P4). The directivity of the coupler is dependant on frequency and is limited by unintentionally leaking to the reverse coupled port.

4.3 Error Model

The forms of error previously mentioned are caused by different phenomena in multiple places in a system which can be difficult to visualise. A common tool to describe error in the electromagnetic domain are signal-flow graphs.

4.3.1 Signal-flows Graphs

A signal-flow graph visually describes the relationships between variables by connecting them with functions, see Appendix D for further detail. Figure 4.1 shows the signal-flow graph of the three term error model (described in the next section). Each node represents a variable. In the figure the two nodes on the left represent the incident (top) and received (bottom) travelling waves, which the ratio of which yields the reflection coefficient.

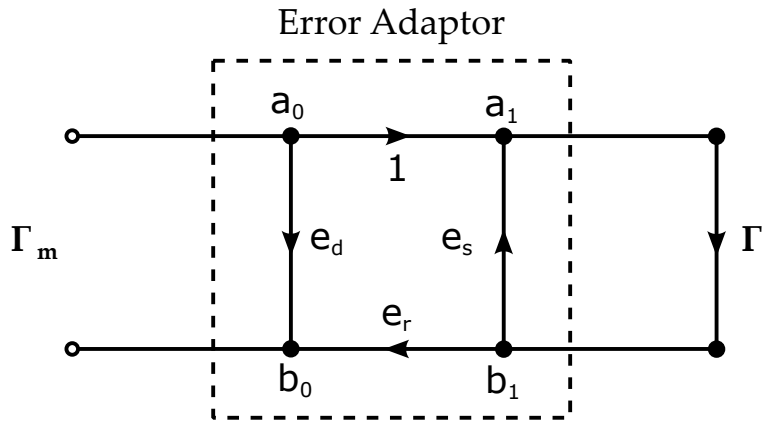

Figure 4.1: 1-port error model where the dashed box is the Error Adapter. The measured reflection coefficient Γ_m (including error) is on the left and the actual reflection coefficient of the load on the right.

An arrow connecting two nodes represents a function applied to the first node and the result received at the second node [78]. In the figure, a_0 is connected to b_0 by e_d, where e_d is a proportion of the incident signal that does not reach the load but instead travels directly to the received node.

If multiple arrow functions meet at a node, the node is the sum of each of the functions.

4.3.2 Three Term Error Model

When measuring the reflection coefficient of an unknown load the measured signal is not solely from the load but the measurement device itself. The three term error model (figure 4.1) is commonly used in VNAs to characterise the cumulative effect of many of the systematic errors in a single port measurement system where:

$\boldsymbol{e_d}$ is the directivity error;

$\boldsymbol{e_s}$ is the source match error;

$\boldsymbol{e_r}$ is the frequency response error [79].

Directivity error can be described as the leakage between the incident and received travelling waves, including reflections from the impedance tube. The source match error is the reflected signal back into the load caused by an impedance mismatch between the source and load. The frequency response error is the vector sum of the attenuation and phase mismatches caused by the length and properties of the

impedance tube. As a note, there is also an error from a_0 to a_1 but this can be ignored by normalising the other error term and allowing this to be unity.

4.4 1-Port Calibration

The calibration of a 1-port network goes as follows

$$\Gamma_m = e_d + \frac{e_r \Gamma}{1 - e_s \Gamma} \tag{4.1}$$

Letting $a = e_r - e_d e_s$, equation 4.1 then becomes

$$\Gamma_m = e_d + e_s \Gamma \Gamma_m + a\Gamma. \tag{4.2}$$

Equation 4.2 can then be applied to each of the three known calibration standard values (Γ_1, Γ_2 and Γ_3) and the measured values (Γ_{m1}, Γ_{m2} and Γm_3) to be expressed as

$$\begin{bmatrix} \Gamma_{m1} \\ \Gamma_{m2} \\ \Gamma_{m3} \end{bmatrix} = \begin{bmatrix} 1 & \Gamma_1\Gamma_{m1} & \Gamma_1 \\ 1 & \Gamma_2\Gamma_{m2} & \Gamma_2 \\ 1 & \Gamma_3\Gamma_{m3} & \Gamma_3 \end{bmatrix} \begin{bmatrix} e_d \\ e_s \\ a \end{bmatrix} \tag{4.3}$$

so that the error terms can be solved

$$\begin{bmatrix} 1 & \Gamma_1\Gamma_{m1} & \Gamma_1 \\ 1 & \Gamma_2\Gamma_{m2} & \Gamma_2 \\ 1 & \Gamma_3\Gamma_{m3} & \Gamma_3 \end{bmatrix}^{-1} \begin{bmatrix} \Gamma_{m1} \\ \Gamma_{m2} \\ \Gamma_{m3} \end{bmatrix} = \begin{bmatrix} e_d \\ e_s \\ a \end{bmatrix} \tag{4.4}$$

$$e_r = a + e_d e_s \tag{4.5}$$

The actual S_{11} can be found by applying the error terms to the measured data with

$$\Gamma = \frac{\Gamma_m - e_d}{e_s(\Gamma_m - e_d) + e_r}. \tag{4.6}$$

4.5 Calibration Standards

Most calibration methods vary only by the mathematical model given to the error sources in the system and the calibration load used, such as quasi-infinite lengths, closed, open, and tube length multiples.

The four variations of calibration standards are shown in Figure 4.2 and their

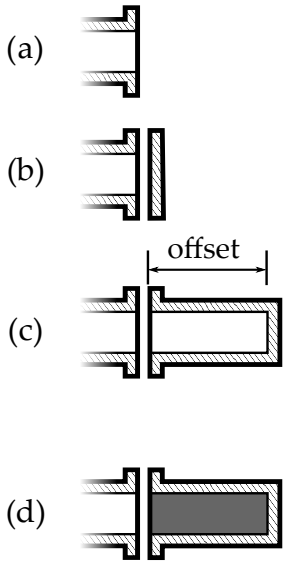

Figure 4.2: Diagram showing the various types of calibration standards used in this calibration. (a) Open. (b) Short. (c) Offset short. (d) Known load with absorbing material.

theoretical reflection coefficients of the various calibration standards are shown in Figure 4.3.

4.5.1 Short

A "short" is then the measurement port is covered with a highly reflective material. Ideally, the reflection coefficient $\Gamma = +1$ and the impedance is $Z = \infty$. The name is analogous to the RF domain short which "short-circuits" the output connector; in our case the waveguide is sealed closed. The short is practically the standard with the least error when constructed due to not having a waveguide component [11]. A short can be constructed with a solid material that is acoustically highly reflective which mounts flush with the connection interface.

4.5.2 Offset Shorts

An offset short is a length of impedance tube with a short on the end. This has the effect of changing the travel distance of the waves, therefore changing the phase. Ideally, it would have a reflection coefficient of unity, but due to the attenuation of the impedance tube walls there are small losses [30].

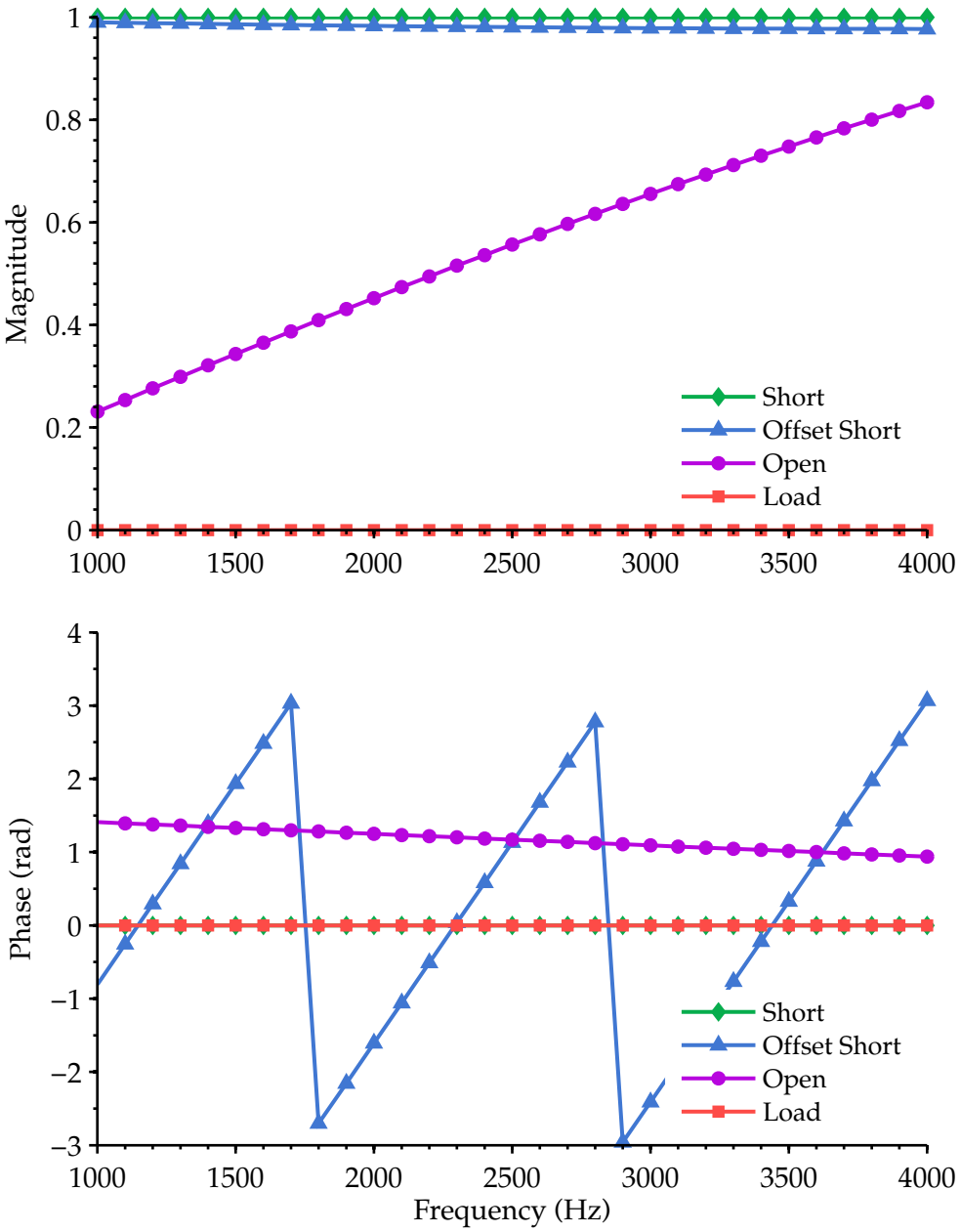

Figure 4.3: Theoretical reflection coefficients of a short, 150 mm offset short, open, and matched load.

4.5.3 Open

An "open" is when the measurement port is disconnected, allowing the travelling waves to move into free air. The reflected wave's sign will be reversed as there is an anti-node at the connection interface. The pressure at the interface will not be zero though due to the geometry of the flange restricting the propagation of the wave into the surrounding medium. The overall effect is that the open has a large reactance and a resistance which is smaller by a factor of ka, where k is the wave number and a is the radius of the tube [11].

In the EM domain a near ideal "open" calibration standard can be achieved due to the large change in impedance between the electromagnetic waveguide and air at the coupling interface [69]. However, in acoustics the open is a weak calibration standard as there is only a small change of impedance between the impedance tube and open air. The size and shape of the flanges at the coupling interface affect the impedance of the open. The theoretical impedance $Z = 0$ and reflection coefficient $\Gamma = -1$ of the open used in this system are shown in Figure 4.3.

4.5.4 Known Load

Known loads are loads with properties that have already been determined, generally either by their physical geometry or by measurement of another device. Many different shapes and materials can be used in combination to create loads which have values that can be calculated, but they are more complex than the short and open, so generally introduce more inaccuracy through estimation than they reduce.

4.5.5 Matched Load

An ideal matched load is an impedance tube of infinite length with the same characteristic impedance of the measurement port. The affect of this is that the impedance of the load is the same as the characteristic impedance of the wave guide, $Z = Z_0$, and the reflection coefficient is $\Gamma = 0$. This can be practically achieved by using a horn, a long impedance tube, or an impedance tube with material of increasing acoustic resistance, but the reflection coefficient will not be ideal and is not well known. A solution to this problem is proposed in the next section.

4.6 Sliding Load Method

The calibration system depends on accurately knowing the reflection coefficient of the calibration standards. Currently the only well known load is the short. The offset shorts introduce the unknown attenuation coefficient of the impedance tube.

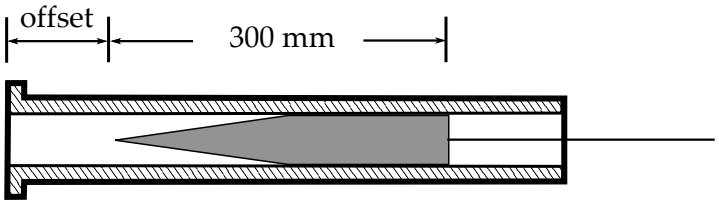

Figure 4.4: Diagram of the sliding load showing the movable wedge-shaped absorbing plunger.

Instead of trying to make the matched load perfect, we can simulate the effect of having one by utilising a physical characteristic of the load.

4.6.1 Theory

When measuring an ideal load, any signal that reached the load would not be reflected. However in the real world there would inherently be some reflections due to impedance mismatches in the system so a non-zero value would be measured. The realisation of this load is constructed by using material which was empirically found to absorb well over the working frequency range and shaping the material into a wedge. Figure 4.4 shows a diagram of the sliding load. Ideally, the non-zero magnitude impedance can be assumed to stay constant as the wedge is moved down the impedance tube – only the phase changes. When plotting the measured reflection coefficient on a real imaginary chart it results in a circle, at the centre of which would be the measured reflection coefficient if the device were presented with an ideal matched load [80]. In reality, the load has the unknown attenuation coefficient of the impedance tube. This attenuation reduces the reflection coefficient of the load and transforms the circle to a spiral, but because this is constant it can be measured.

4.6.2 Circle Fitting Algorithm

The circle (or technically a spiral but can be approximated to a circle) is fitted with a circle fitting algorithm by Taubin [81]. The fitting algorithm attempts to fit a circle to the data which results in the smallest residual error. The fitted circle has a radius and a centre position, where the radius of the circle represents the reflectivity of the load. In other words, a large circle represents a highly reflective load and a small circle being close to a matched load. As described above the centre position is used as proxy for the ideal matched load in the calibration scheme.

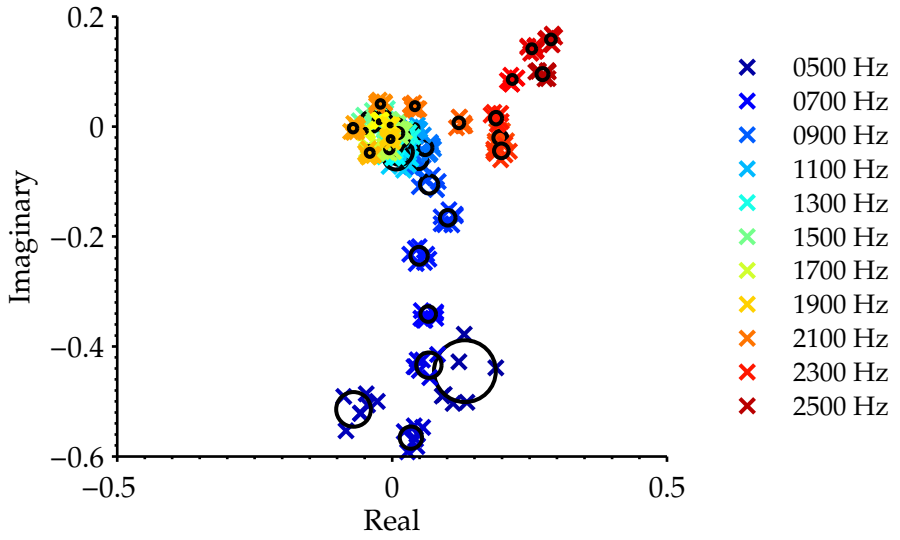

Figure 4.5: Sliding load circle fits.

4.6.3 Measurements

The sliding load was used to make measurements with a foam wedge previously shown in the bottom of Figure 3.8. Figure 4.5 shows the fitted circles of a sliding load at various frequencies. This can be plotted on a smith chart to show the variation of reflection coefficient of the load and residual error of the system as shown in Figure 4.6.

Figure 4.7 shows the fitted circle of a piece of foam with a piece of acrylic attached to the face to create a highly reflective sliding load, or a "sliding short". The result is a circle with a large radius. The frequency response of the sliding short is shown in Figure 4.8. The radiuses of the load can also be interpreted in a manner similar to an uncalibrated reflection coefficient, as shown in Figure 4.9. The large radiuses of the sliding short show the spiralling effect more than the lossy sliding loads, which leads on to measuring this effect in the next section.

4.7 Impedance Tube Attenuation

One of the negative effects of sliding a load down an impedance tube is that the length of the impedance tube changes which causes increased attenuation with distance. This effect is shown in the measured circles by the radius reducing in size as the position increases. The result is a spiral with the pitch being proportional to the attenuation of the tube.

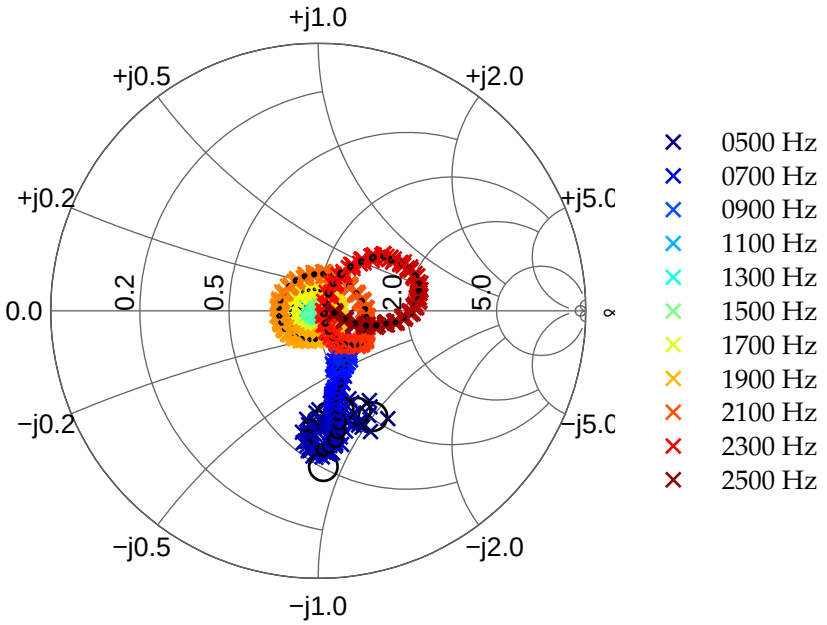

Figure 4.6: Sliding load plotted on a Smith chart. The trail shows the change in impedance with frequency. The size of the circles indicate the absorption of the load.

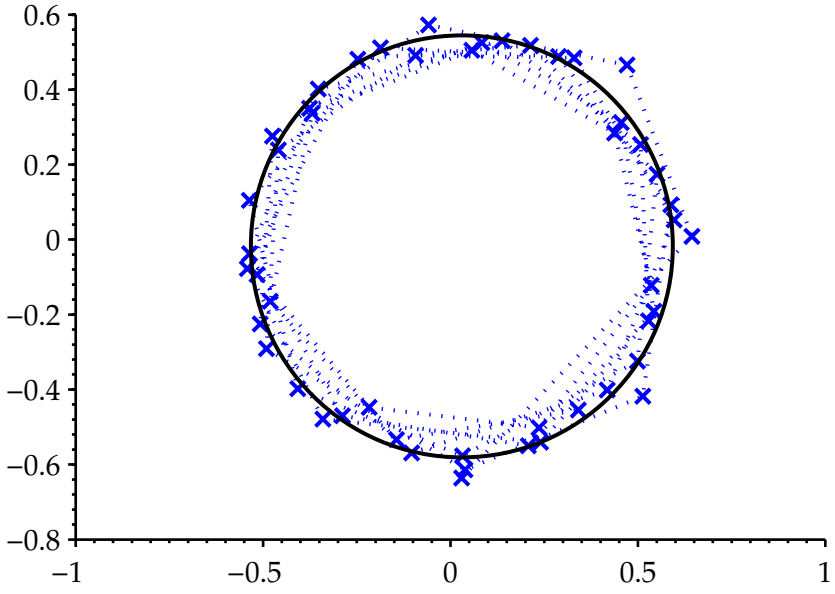

Figure 4.7: Sliding short at 1250 Hz.

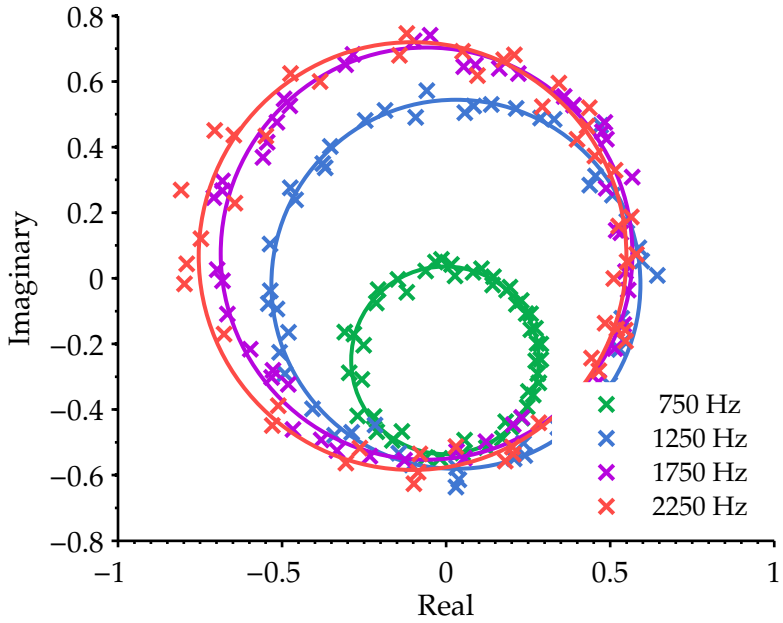

Figure 4.8: Sliding shorts at a selection of four frequencies.

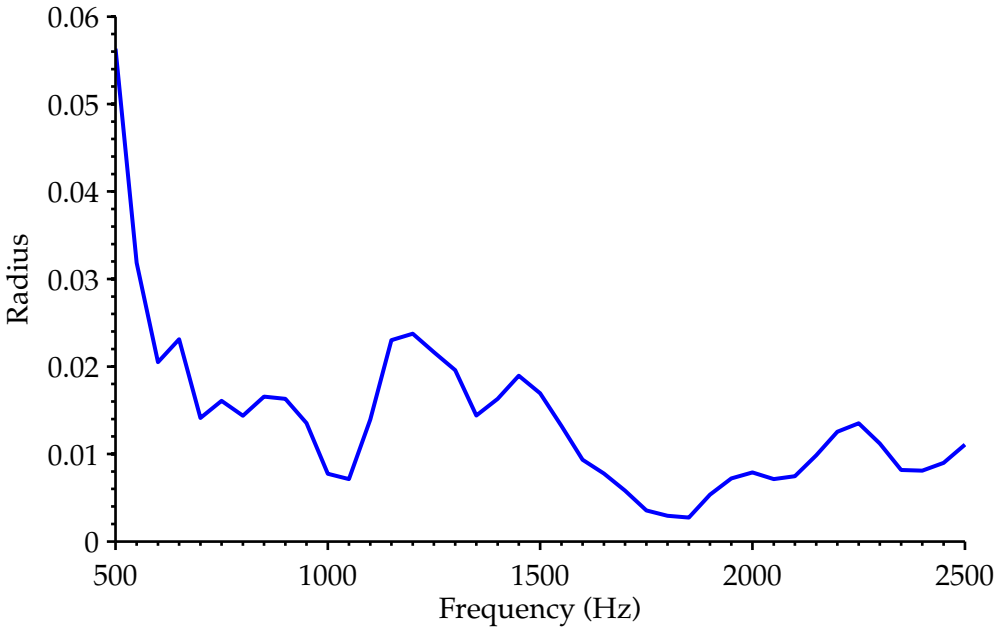

Figure 4.9: Sliding load impedance.

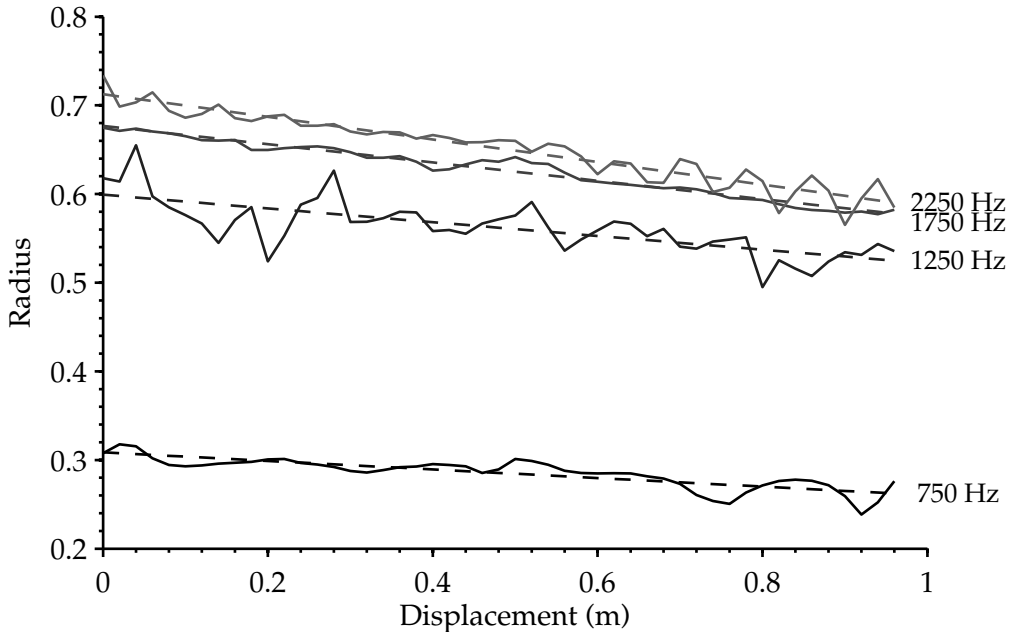

Figure 4.10: Sliding short at 4 frequencies showing the radius of the circle versus displacement.

4.7.1 Spiral Fitting Algorithm

Using the circle fitting algorithm to determine the centre of the spiral the data can be unwrapped to calculate the attenuation with respect to displacement as shown in Figure 4.10. This process can be done for each measured frequency which allows for a measure of the attenuation of the characteristic impedance tube with respect to frequency as shown in Figure 4.11.

4.7.2 Calibration Standard Selection

The 1-port calibration requires at least three distinct known loads in order to produce a successful calibration. Figure 4.12 shows the theoretical characteristics of the various loads available for calibration. The problem lies in that the short and an offset short will have the same phase at specific frequencies determined by the offset distance. Therefore, to work well over the frequency range of the coupler, certain calibration standard combinations can be used for specific frequencies. Figure 4.13 shows the selection of calibration standard based on measurement accuracy. The calibration standard used is the one with the highest measurement confidence.

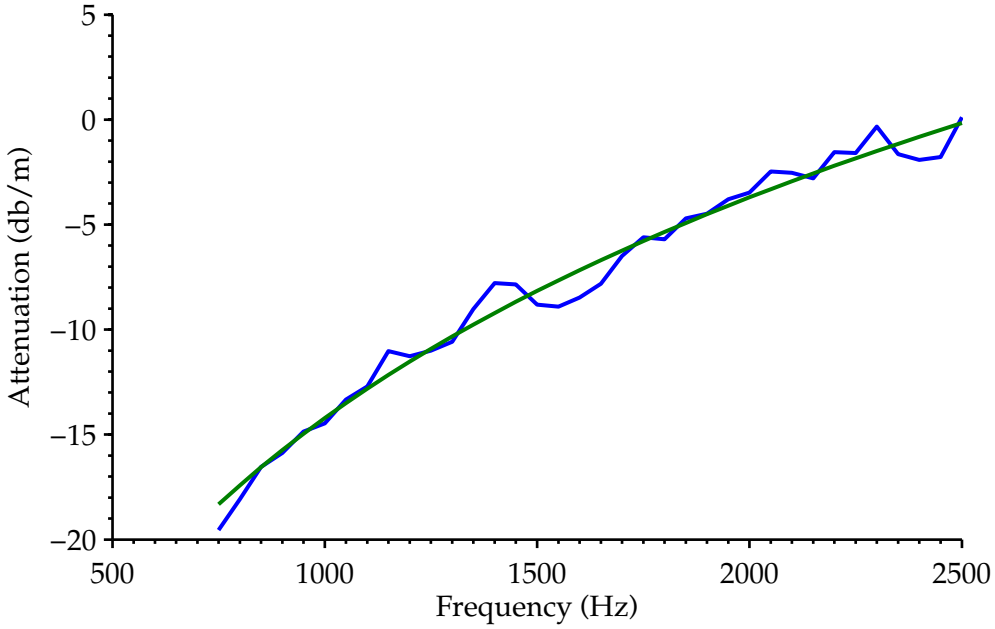

Figure 4.11: Sliding short at 1250 Hz with the unwrapped measured data shown in blue and the polynomial fit shown in green.

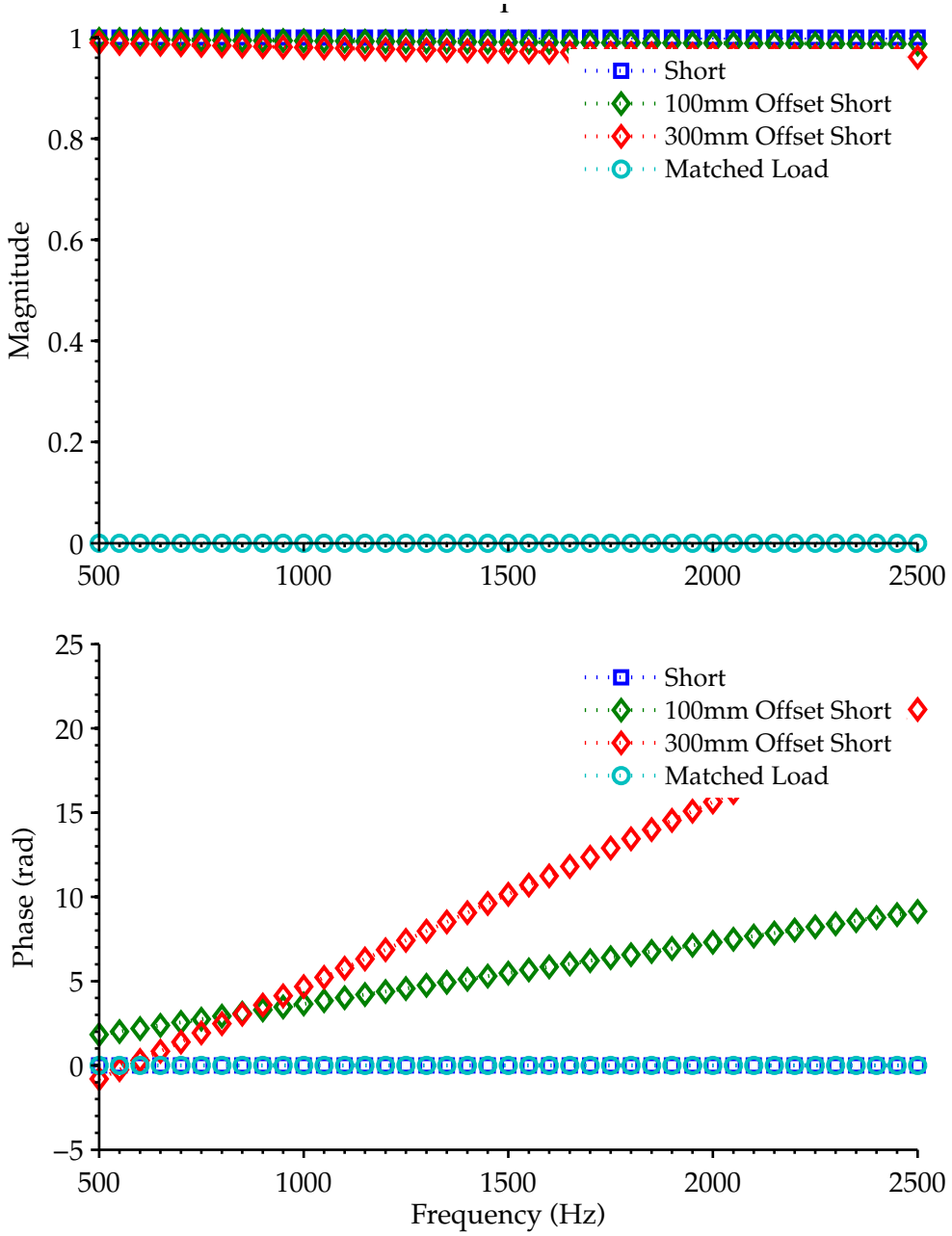

Figure 4.12: Theoretical performance of calibration standards.

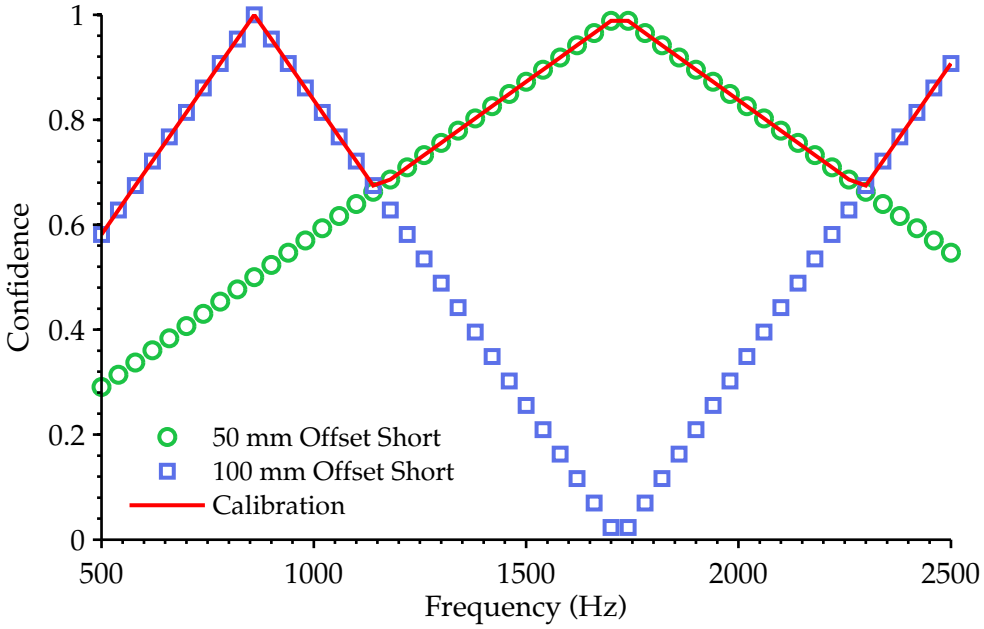

Figure 4.13: Confidence of offset shorts as calibration standards.

5 Measurement

In this chapter the calibrated acoustic vector network analyser is used to measure several 'known' reference standards and used practically to characterise the acoustic properties of pasture. Section 5.2 discusses the reference standard measurements. Measurements of soil and pasture are performed in Section 5.3.

5.1 Introduction

Several calibration standards were developed to calibrate the device but only three were used in the three-term error correction. The unused calibration standards can be used as reference standards to evaluate the performance of the calibration.

5.2 Reference Standards

Measurements of the reference standards further verify the validity of the calibrated device. Figure 5.1 shows the raw results from measuring various available calibration standards. There is high variance of all three short-based calibration standards outside of the usable frequency range but they are relatively similar across the working range. The sliding load has an ideal magnitude due to assumptions when making the measurement as previously discussed in Section 4.6. A comparison of the 50 mm short measured data with the calibrated result is shown in Figure 5.2 .

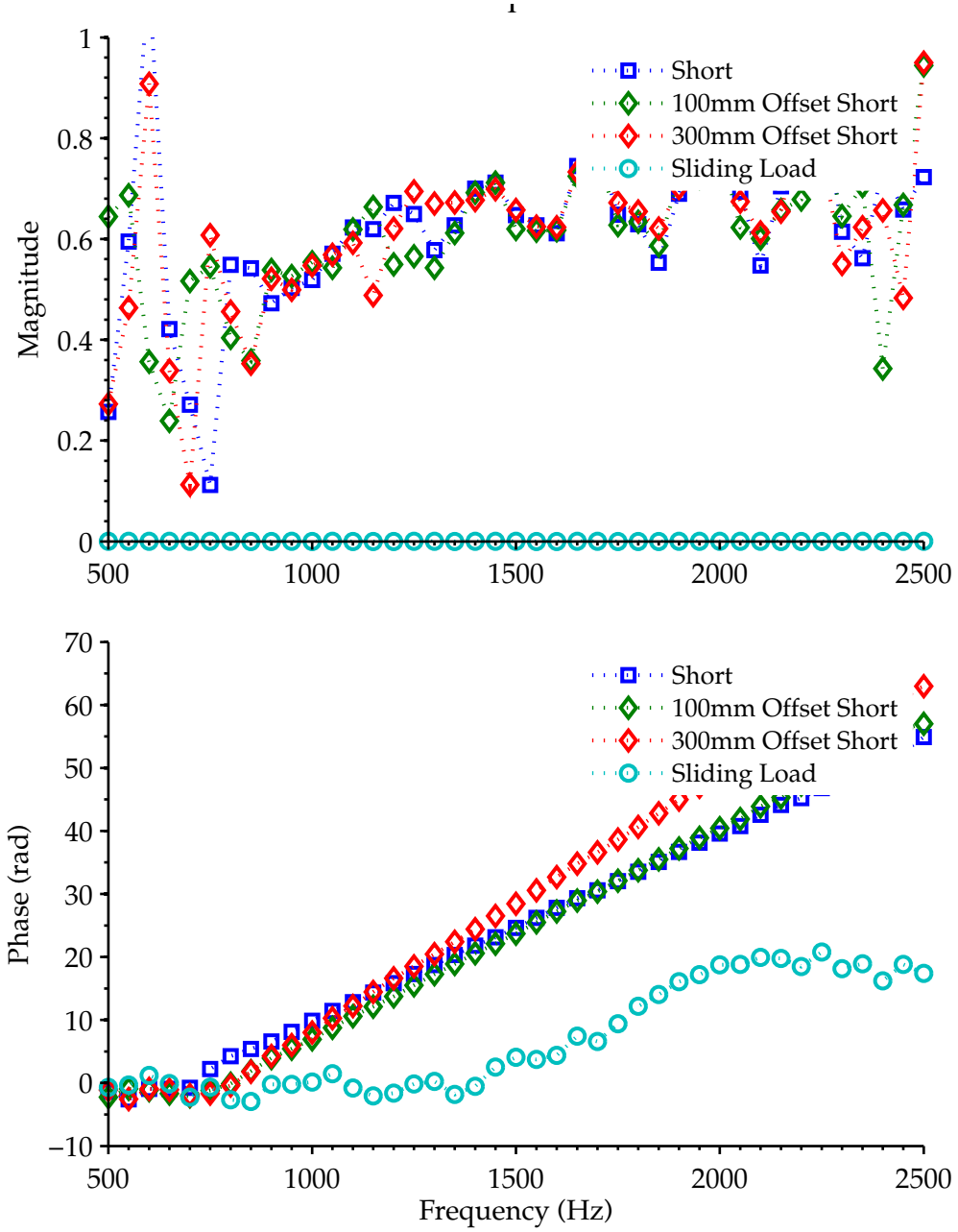

Figure 5.1: Uncalibrated reflection coefficients of various calibration standards.

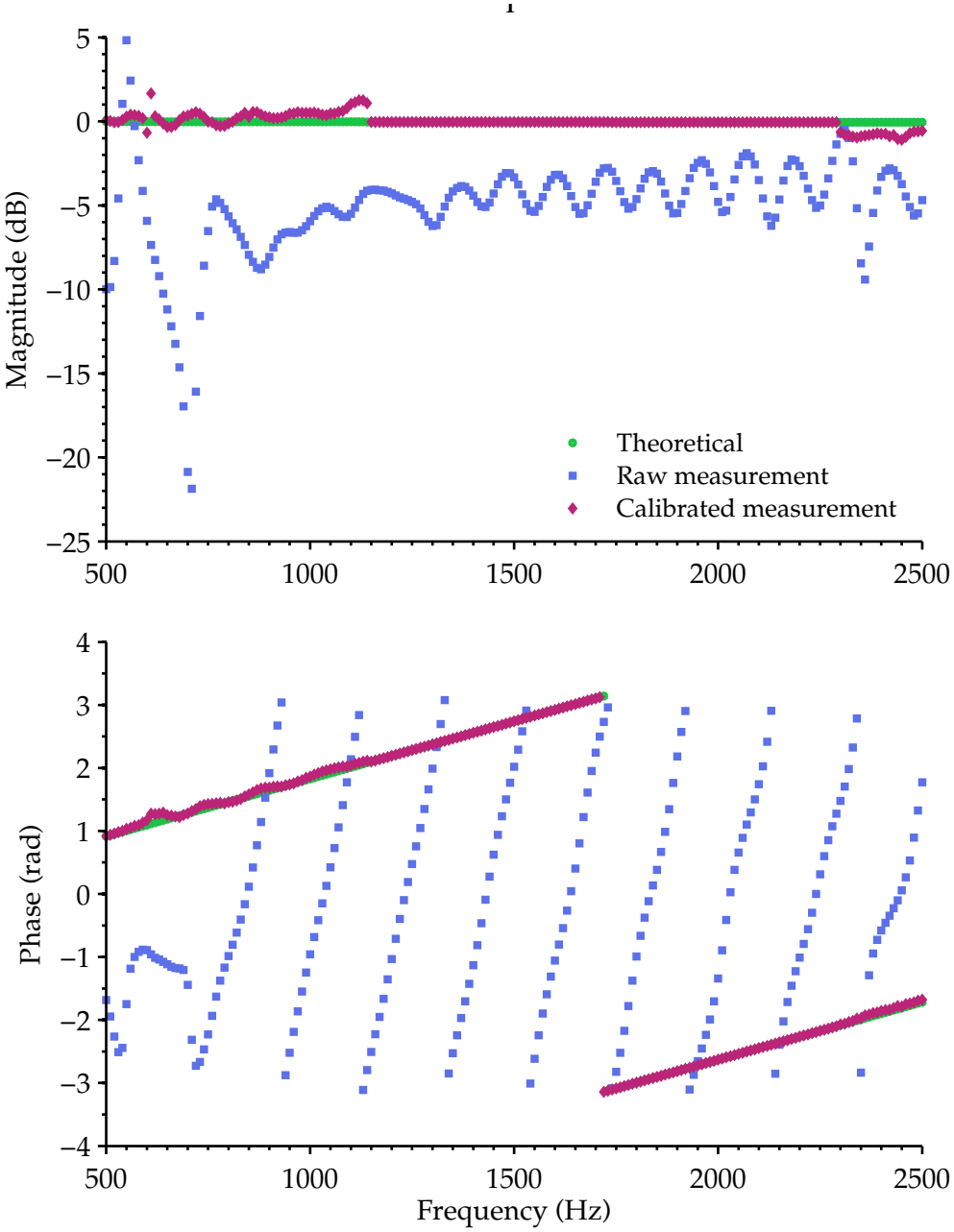

Figure 5.2: Measured versus theoretical 50mm calibration standard comparison.

The bands of frequencies where the 50 mm standard was used in the calibration can be seen where the value is exactly the same as the theoretical.

5.2.1 Time Dependence

The effectiveness of the calibration is greatest directly after calibrating with fresh measurements of the three calibration standards. Over time the system drifts due to various slow moving effects within the hardware and environment. The effectiveness of the measurement system can be shown in Figure 5.3 as the same measurements of the short at different durations after calibration. After one hour the measurement has an error of 1% at various frequencies and after 12 hours the error increases to almost 5%.

The calibrated measurements were made directly after performing a new calibration to ensure this error minimally influenced the results.

5.3 Pasture

The acoustic vector network analyser excels at characterising the impedance of a material or object. One of the original motivations of this research was to measure the acoustic properties of pasture to further aid the development of pasture meters. Living plants are an interesting object to characterise as they have a unique shape, texture and density – appearing quite different from typical acoustic mediums. A simple approach to estimating the quantity by measuring the height of the pasture with respect to the soil. This can be achieved by a device at an unknown height by being able to detect the level of the soil and the pasture independently. Aylor [6] developed a model for the sound attenuation of dense plantations by transmitting random noise through reeds. This method simply transmitted sound from one side of the reeds and measured at the other. He found that the attenuation increased with leaf area density, plantation thickness, and frequency. The model only loosely predicts the behaviour of herbaceous plants.

The pasture sample used in the measurement was perennial ryegrass – commonly used by dairy and beef farms in New Zealand. The grass sample taken from the farm had the grass and layer of soil below; where the grass was on average approximately 20 cm in length to the soil level; and the soil and root section was 15 cm. The measurements were made shortly after collecting the sample to ensure the grass stayed in healthy condition and the soil properties changed as little as possible.

Firstly, the grass and soil sample was cut to a “plug” to fit the same 60x60 mm square shape as the wave guide as shown in Figure 5.4 . The sample plug was

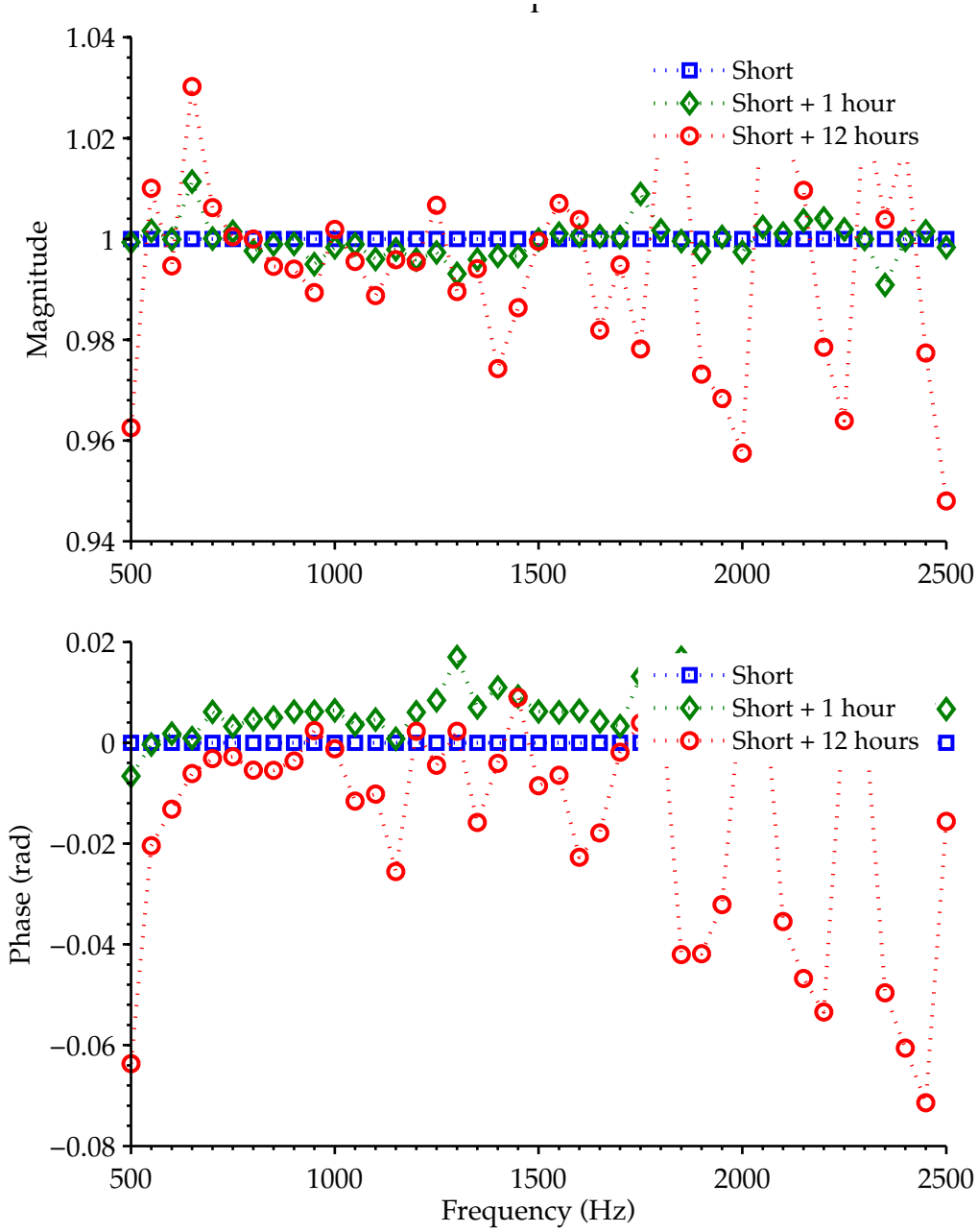

Figure 5.3: Calibrated short measurement after 1 and 12 hours.

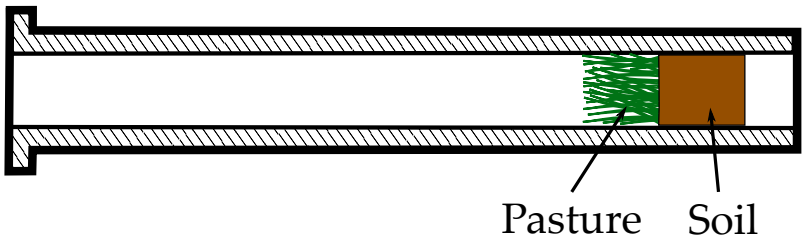

Figure 5.4: Pasture and soil plug in the impedance tube.

placed into the unterminated waveguide with the tips of the grass at the attachment interface ($x = 0$) and the top of the soil starting at approximately $x = 15\,\text{cm}$ down the sample holder. The setup essentially replicates measuring the grass in a paddock from above including the soil below.

The grass was then cut from the soil with as little disturbance to their structure as possible and each measured in the same sample holder waveguide as the previous measurement.

The comparison between three different pasture and soil configurations is shown in Figure 5.5 and 5.6 . The working range of the device is between 800 and 2200 Hz so the results below and above these frequencies can be ignored. The pasture has a reflection coefficient of $-20\,\text{dB}$ and decreases to $-25\,\text{dB}$ with increasing frequency. The increasing ripple can be attributed to standing waves between the pasture and the open end of the sample holder tube. The soil is shown to be highly reflective with a reflection coefficient of 0.7 at 900 Hz and decreasing to 0.4 at 2000 Hz, therefore the absorption and/or transmission of soil must be increasing with frequency. When we look at the pasture and the soil in the sample holder together we see that the reflection coefficient is similar in shape to soil alone, except that the magnitude is approximately 0.2 less. We can conclude that since the pasture by itself has a relatively small reflection coefficient that the majority of the difference between soil and 'pasture+soil' is due to the absorption of the pasture. It can be seen that the pasture and soil together sample approaches the same measurement of just pasture alone at higher frequencies—the soil can no longer be seen. To summarise:

- Pasture reflects a relatively small ($-25\,\text{dB}$) amount of acoustic energy within the working range.

- Pasture and soil absorbs sound well at low frequencies and absorption increases with frequency, to a point where sound is almost no longer transmitted through the pasture.

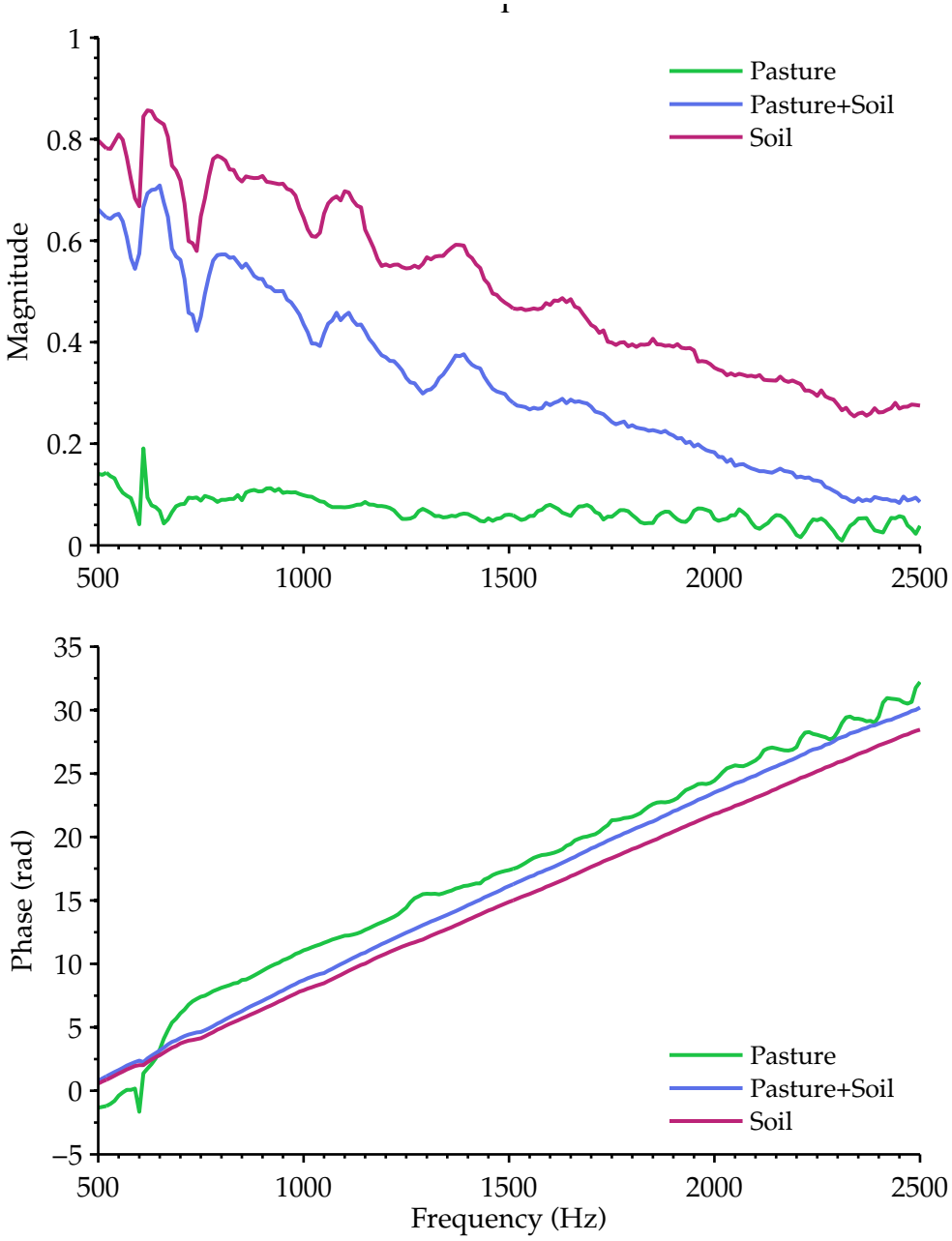

Figure 5.5: The magnitude and phase of the measured reflection coefficient of just the pasture; pasture still attached to the soil; and only the soil.

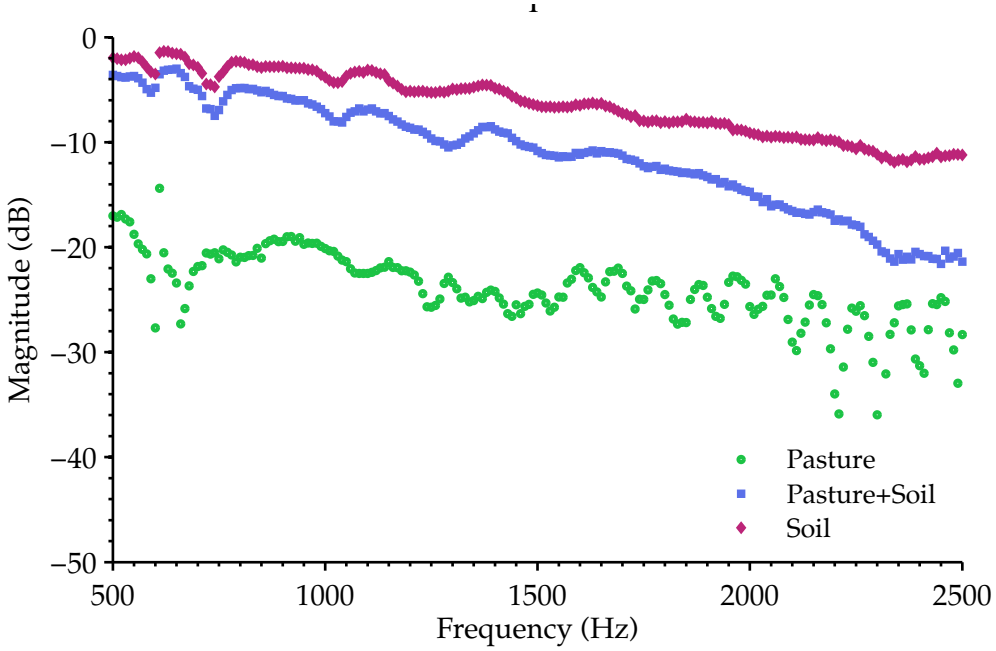

Figure 5.6: The magnitude of the reflection coefficient measurement in dB of pasture, soil and pasture, and soil.

- Soil reflects well at low frequencies and decreases at higher frequencies.

From these observations we can conclude that pasture meters utilising the ultrasonic frequencies will have difficulty transmitting through the pasture measuring echoes from the soil but should work well for the pasture measurement. Frequencies of 2000 Hz or less should be utilised to determine the soil position.

6
Conclusion

This project successfully completed two implementations of an acoustic vector network analyser; the first using the standing-wave method and the second using an acoustic directional coupler.

The literature survey found that Price [55] described a system that appeared to produce accurate results, but more detailed peer-reviewed publications were not found which raises questions to the robustness of the method. Our implemented design tried to use many of the successful aspects shown in the literature. The method was found to be unreliable for two reasons; the fitting algorithm failed at many frequencies and the method requires multiple calibration stages which severely limit error-correction techniques.

Separating the travelling waves using the fitting method looked excellent on paper but in practice we found that there were often microphone measurements that produced contradicting results to the expected standing wave.

The other disadvantage is that the method requires microphone compensation followed by applying the fitting algorithm before directional can be found. This prevents effective error correction due to the data not being repeatable and therefore unable to form an accurate error model of the system.

The directional coupler method utilises a mechanical, rather than computational, method to separate the travelling waves. This method still has inherent error but it is systematic so error-correction methods can be employed to minimise these effects. A three-term error model was utilised to correct the directivity, source match and

frequency response error in the coupler.

The constructed device performs well to an accuracy of ± 1.5 dB over a frequency range from 800 to 2200 Hz, where previously the uncalibrated data varied by ± 5 dB as shown in figure 5.2. The sliding load proved to be a very useful tool when there are no known loads available. It also yielded an accurate attenuation measurement of the impedance tube by unwrapping the phase data. The constructed calibration standards were shown to be non-ideal but good enough to provide meaningful results. We suspect the majority of the error in the system can be attributed to the construction of the system and the 'known' values of the calibration standards. Improving the coupler directivity will yield the greatest gains by increasing the effective signal-to-noise ratio of the coupled directional data. The electromagnetic VNA and calibration standards took decades to progress to the current state of fast, accurate, and convenient measurements. The acoustic VNA could follow a similar path with improved versions building upon the previous best systems.

6.1 Future Work

There are multiple areas for further possible research from this project.

- One of the limitations is the usable frequency range. The impedance tube and coupler dimensions can be scaled up or down to shift the usable frequency range. An investigation could be conducted into alternate coupler designs which choose wider branch nodes to sacrifice more directionality for a wider working range. In order for this sacrifice to be beneficial further efforts must be made to increase signal to noise in the system. These should include improved acoustic seals, a higher performance loudspeaker (preferably a piston driver), microphones and amplifiers that a bigger budget would allow.

- Constructing improved calibration standards. Known resistive loads should provide a more stable calibration due to smaller frequency dependent standing-waves. With each increase in accuracy a better estimate of the actual value of the calibration standards can be made, which in turn further improves measurements. More than three calibration standards could also be used in combination with an algorithm presented by Marks [82].

- Building an additional compatible AVNA would allow for a two-port calibration and to be able to determine the transmission and absorption coefficients of the unknown loads. The two-port calibration also opens the doors to a variety of new calibration standards and error models for faster and more accurate measurements.

- There is a vast amount of practical applications for an accurate acoustic characterisation device. As agriculture is New Zealand's largest export industry it would seem logical to characterise a wide range of plants and pasture. A variety of physical attributes such as moisture content, fibre content, length, growth stage, and species could correlate to acoustic signatures.

A

Mathematical Proofs

A.1 Reflection Coefficient at an Impedance Interface

The reflection coefficient Γ and the transmission coefficient $\mathbf{T}$ can be expressed as

$$\Gamma = \frac{\mathbf{p}_r}{\mathbf{p}_i} \tag{A.1}$$

and

$$\mathbf{T} = \frac{\mathbf{p}_t}{\mathbf{p}_i} \tag{A.2}$$

respectively, where $\mathbf{p}_r$ is the reflected wave, $\mathbf{p}_i$ is the incident wave and $\mathbf{p}_t$ is the transmitted wave. The pressure on either side of the interface must be the same so that

$$\mathbf{p}_i + \mathbf{p}_r = \mathbf{p}_t \tag{A.3}$$

where the pressure on one side is the combination of the incident and reflected waves and the other side is the transmitted wave. Dividing through by $\mathbf{p}_i$ yields

$$\frac{\mathbf{p}_i}{\mathbf{p}_i} + \frac{\mathbf{p}_r}{\mathbf{p}_i} = \frac{\mathbf{p}_t}{\mathbf{p}_i} \tag{A.4}$$

and substituting equations A.1 and A.2 gives

$$1 + \Gamma = T. \tag{A.5}$$

The volume velocity U at the interface is also equal on either side such that

$$U_i - U_r = U_t \tag{A.6}$$

noting that the reflected wave is negative as it is travelling in the opposite direction to the incident and transmitted waves. Equation A.6 can be expressed in terms of p by substituting $U = \frac{p}{Z}$ to give

$$\frac{p_i}{Z_1} - \frac{p_r}{Z_1} = \frac{p_t}{Z_2} \tag{A.7}$$

where Z_1 is the impedance on the incident and reflected side of the interface and Z_2 is on the transmitted side. Rearranging and substituting equations A.1 and A.2 to remove the pressure terms gives

$$1 - \Gamma = \frac{Z_1}{Z_2} T. \tag{A.8}$$

Solving for Γ by using equation A.5 results in

$$\Gamma = \frac{Z_2 - Z_1}{Z_2 + Z_1}. \tag{A.9}$$

B

Publications

Determining Acoustical Directionality in an Impedance Tube Using Multiple Fixed Microphones

Kyle Pennington
Department of Engineering,
University of Waikato
Private Bag 3105,
Hamilton, New Zealand.

Jonathan Scott
Department of Engineering,
University of Waikato
Private Bag 3105,
Hamilton, New Zealand.

Kerry Bodman
Gallagher Group Ltd.
Kahikatea Drive,
Hamilton, New Zealand.

***Abstract*—Acoustic impedance of a port or object is a valuable piece of knowledge describing how well sound is transmitted or reflected. The commonly used slotted-line method is labourious and time consuming, requiring manual movement to find the maxima and minima at each frequency. This paper outlines a technique to computationally determine the magnitude and phase of the constituent travelling waves from the standing plane sound wave measurements in an impedance tube. Measured magnitude and phase data from multiple fixed microphones carefully spaced along the length of the impedance tube is numerically fitted to incident and reflected wave models, which can then be used to calculate the complex acoustic impedance at each frequency of interest.**

I. Introduction

The ability to fully characterise the interaction of sound with objects or materials has a wide range of applications, including sound absorption materials, musical instruments [1], speaker enclosures, exhaust systems [2], and ear canals [3]. Acoustic impedance efficiently describes acoustic reflection, absorption, and transmission for an element of a closed linear system. These properties allow designers to use the most effective material for a particular environment, or to optimise a design to suit a specific purpose.

In the electrical domain, a vector network analyser (VNA) is used to measure the s-parameters with high precision and accuracy by mixing and down converting the signal and reference sources. In order to do this, the forward and reverse travelling waves must be separated. A VNA utilises directional couplers to physically separate these waves by intelligent design with constructive and destructive interference. In the acoustical domain this mechanism is difficult to achieve due to the physical characteristics of sound in air.

Prior to the VNA, the slotted-line method was commonly used to determine the directional waves. This was done by allowing a standing wave signal (caused by the superposition of the incident and reflected plane waves) to stabilise in a transmission line and measure specific points of the standing wave through a small slot to find the standing wave ratio (SWR). This same theory can be applied to the acoustic domain [4][5] using an acoustic impedance tube and a movable microphone. One of the limitations with this method is that it is laborious and time consuming as the microphone must be manually moved to find the maxima and minima for each frequency. This method can also produce small errors attributed to the physical interference of the movable microphone with the sound waves inside the tube.

This paper will explore the concept that the SWR can instead be determined by placing multiple fixed microphones at various spacings along the length of the impedance tube and numerically fitting the standing wave interference pattern to the measured data points.

II. Test Apparatus

The apparatus as shown in fig. 2 is a length of circular tube with a loudspeaker mounted to the left end and a flange to the other. Microphones are inserted so as their faces are flush with the inner surface of the tube and have o-ring seals to minimise any possible interference with the plane waves. [6] states the upper frequency limit f_u is limited by the inner diameter d of the tube such that

$$f_u = \frac{0.58c}{d} \tag{1}$$

where c is the speed of sound in air. Above f_u, higher-order modes take effect and the sound waves are no longer planar.

Fig. 1 shows the system diagram. A VNA is used to measure the magnitude and phase from each microphone. Each input is referenced from the RF out. The VNA mixes the received signal with the output signal in order to isolate and only measure the frequency of interest. The loudspeaker is driven by an audio amplifier with the signal from the RF out of the VNA. A dual channel pre-amplifier was built to enable the microphones have full scale deflection over the VNA input voltage range.

III. Measurement Method

The raw measured data is passed through two stages of processing as shown in fig. 3.

A. Gain Compensation

The low-cost microphones are purchased uncalibrated, so they inherently have slightly different gain profiles. The gain and phase profile of each microphone is measured in the same position along the impedance tube with a solid covered

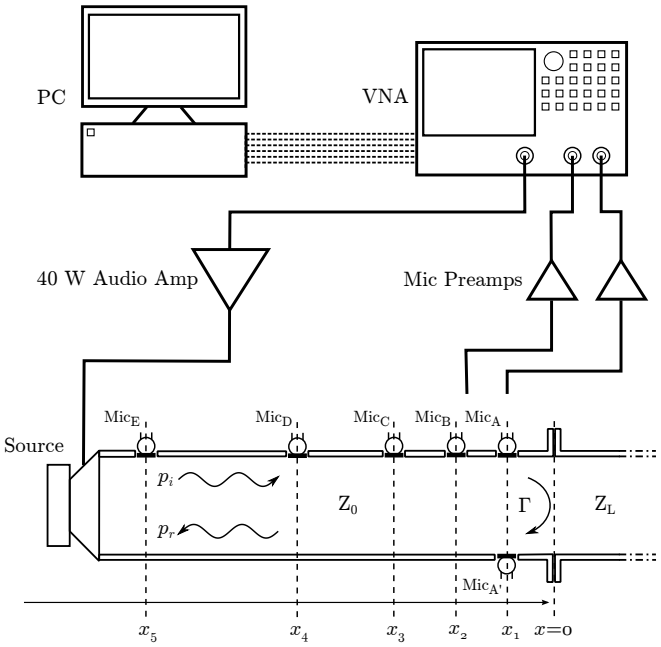

Figure 1. Multi-microphone apparatus.

Figure 2. Acoustic impedance tube.

end. This situation allows the uncompensated gains (shown in fig. 4) to be compared and normalised (shown in fig. 5) to one arbitrary microphone in a repeatable environment. A linear least squares fit of the normalisation matrix is then applied to raw measurement data sets. The effectiveness of the compensation matrix is shown in fig. 6. A high signal amplitude was used to ensure high signal to noise ratio across all of the frequencies. It should be noted that because of this there is clipping due to system resonance at 500 Hz.

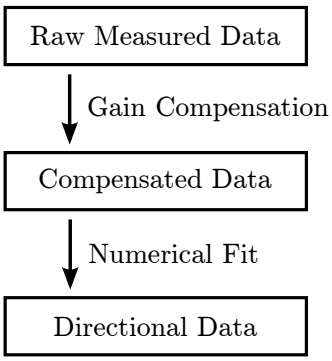

Figure 3. Data block diagram

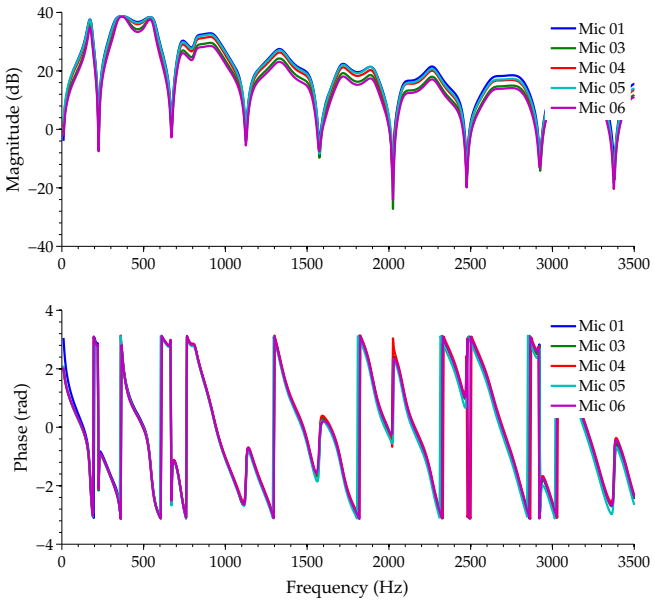

Figure 4. Uncompensated microphone measurements of a covered end.

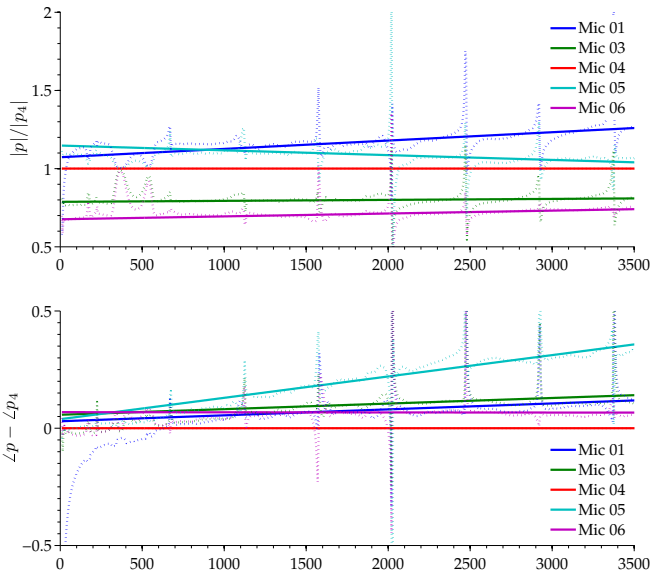

Figure 5. Magnitudes normalised to microphone 4 are shown with the dotted traces and the corresponding least-squares fit shown with a solid line.

B. Directionality

1) Standing Wave Model: An accurate model of the measured sound pressure must be developed in order to decompose the standing wave into the constituent travelling plane waves. The general form for the sound pressure of a travelling wave can be represented at any point on the x-axis and time t by

$$\boldsymbol{p}(x,t) = Ae^{j(\omega t - \boldsymbol{k}x + \phi)} \quad (2)$$

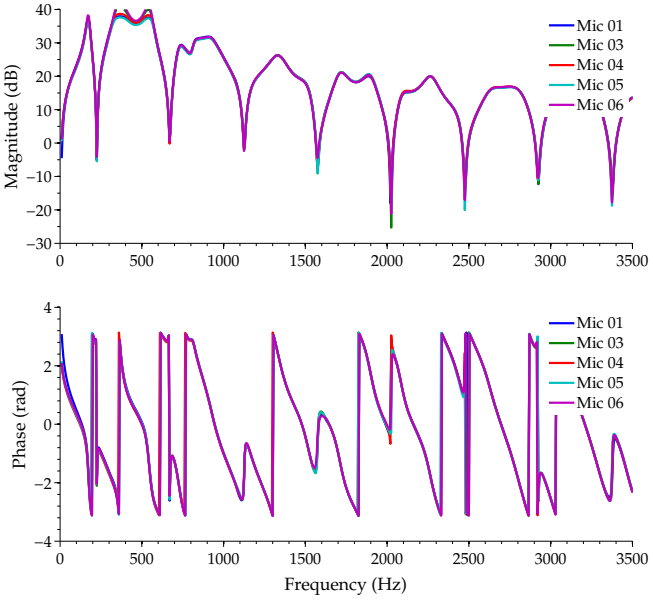

Figure 6. Compensated data of the covered end with the normalisation matrix applied.

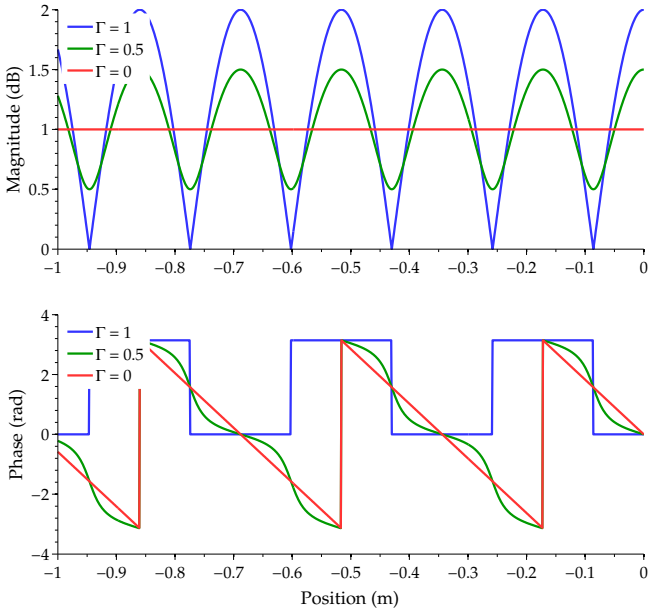

Figure 7. Various standing wave patterns at 1 kHz

$$\boldsymbol{k} = \frac{\omega}{c} + j\alpha \tag{3}$$

where:

A = amplitude,
$\omega = 2\pi f$ = angular frequency,
c = speed of sound in air,
ϕ = phase shift,
α = attenuation constant.

Letting $\boldsymbol{A} = Ae^{j\phi}$ and dropping ωt by using the phasor representation, the sound pressure of the incident (positive x) and reflected plane sound waves (negative x) can then be expressed as

$$\boldsymbol{p_i} = \boldsymbol{A_i} e^{-j\boldsymbol{k}x} \tag{4}$$

and

$$\boldsymbol{p_r} = \boldsymbol{A_r} e^{j\boldsymbol{k}x}, \tag{5}$$

respectively. Using the superposition theory, the actual measured magnitude and phase of the sound pressure by the microphones at any point x becomes:

$$\boldsymbol{p} = \boldsymbol{A_i} e^{-j\boldsymbol{k}x} + \boldsymbol{A_r} e^{j\boldsymbol{k}x} \tag{6}$$

The complex reflection coefficient of the load ($\boldsymbol{Z_L}$) at $x = 0$ is:

$$\boldsymbol{\Gamma} = \frac{\boldsymbol{A_r}}{\boldsymbol{A_i}} = \frac{\boldsymbol{Z_L} - \boldsymbol{Z_0}}{\boldsymbol{Z_L} + \boldsymbol{Z_0}} \tag{7}$$

The standing wave patterns are shown in fig. 7 for a range of reflection coefficients. If the impedance tube has a characteristic impedance $\boldsymbol{Z_0}$ then $\boldsymbol{\Gamma} = 0$, $\boldsymbol{\Gamma} = 0.5$, and $\boldsymbol{\Gamma} = 1$ would be produced in the following conditions $\boldsymbol{Z_L} = \boldsymbol{Z_0}$, $\boldsymbol{Z_L} = 3\boldsymbol{Z_0}$, and $\boldsymbol{Z_L} = \infty$, respectively. The corresponding standing wave pattern expected in the impedance tube is shown in fig. 7. An excellent fit can be achieved due to the strong functions of both the magnitude and phase and by selecting the microphone positions carefully so that they lie across the features of the wave.

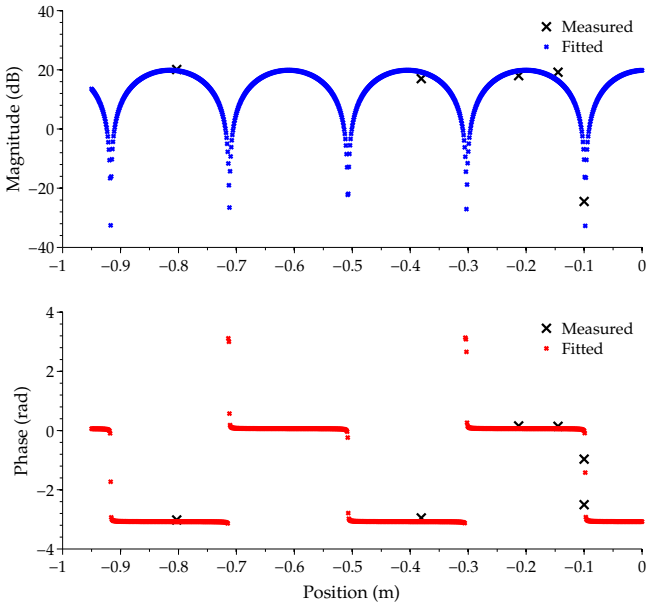

Figure 8. Fitted and measured data of a covered end at 840 Hz.

2) Implementation: MATLAB is used to fit the standing wave pattern (shown in fig. 8) to the measured data by allowing the non-linear solver to vary the magnitude and phase of the

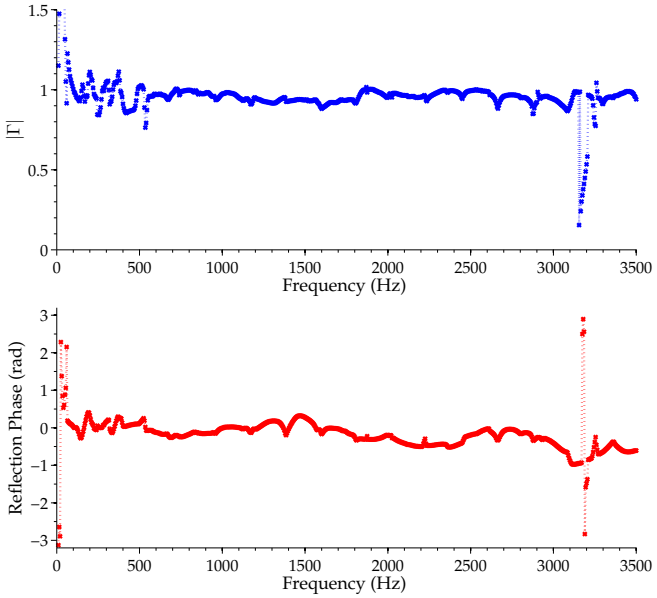

Figure 9. Reflection coefficient and phase of a covered end.

forward and reverse waves while attempting to minimise the least-squares error between the measured ($\boldsymbol{p_{meas}}$) and fitted data ($\boldsymbol{p_{fit}}$). The error term is calculated by:

$$\boldsymbol{p_{fit}} = \boldsymbol{A_i} e^{-j\boldsymbol{k}x} + \boldsymbol{A_r} e^{j\boldsymbol{k}x} \tag{8}$$

$$err_{real} = \Re(\boldsymbol{p_{fit}} - \boldsymbol{p_{meas}})$$

$$err_{imag} = \Im(\boldsymbol{p_{fit}} - \boldsymbol{p_{meas}})$$

$$err_{total} = \frac{err_{real}^2 + err_{imag}^2}{\frac{|\boldsymbol{p_{fit}}|+|\boldsymbol{p_{meas}}|}{2}}. \tag{9}$$

The fitting algorithm is run individually for each step in the frequency sweep to determine the acoustic impedance. Fig. 9 shows the acoustic impedance of the covered end which theoretically should have a reflection coefficient of 1 and a constant phase. The erroneous results below 500 Hz is caused by the microphone voltage clipping due to impedance tube and loudspeaker resonating at those frequencies. This effect can be corrected by lowering the amplitude of the driving signal but was chosen not to so to increase the accuracy of the majority mid-range frequencies. The disparity at 3155 Hz is caused by the 5 microphone measurements coincidentally falling on the same position of the waveform so not providing enough data for an accurate fit.

IV. Conclusions

The acoustic impedance measurements show that this method is a viable alternative to the slotted line method, although there are multiple issues that need to be addressed to improve reliability and accuracy. The precision of the magnitude and phase measurements has a large influence on the resulting fit, which means for this method to be improved, either higher quality microphones should be used or a more detailed calibration routine implemented. Extra elements also need to be included in the standing wave model such as amplitude decay from the tube material and gas losses. The speed of sound should also be intelligently measured precisely in order to further reduce errors rather than an estimate from room temperature.

The next stage of this work should include measuring various known physical elements to compare with the theoretical values and provide more calibration data.

References

[1] V. Gibiat and F. Laloë, "Acoustical impedance measurements by the two-microphone-three-calibration (TMTC) method," *J. Acoust. Soc. Am.*, vol. 88, pp. 2533–2545, December 1990.

[2] R. Boonen and P. Sas, "Determination of the acoustical impedance of an internal combustion engine exhaust," in *Proceedings of ISMA2002*, vol. 5, pp. 1939–1946, 2002.

[3] D. H. Keefe, R. Ling, and J. C. Bulen, "Method to measure acoustic impedance and reflection coefficient," *J. Acoust. Soc. Am.*, vol. 91, pp. 470–485, January 1992.

[4] ISO 10534-1:1996, "Acoustics — determination of sound absorption coefficient and impedance in impedance tubes — Part 1: Method using standing wave ratio."

[5] ASTM Standard C384, 2004, "Standard test method for impedance and absorption of acoustical materials by impedance tube method."

[6] ISO 10534-2:1998, "Acoustics — determination of sound absorption coefficient and impedance in impedance tubes — Part 2: Transfer-function method."

Acoustic Vector-Corrected Impedance Meter

Jonathan Scott, *Senior Member, IEEE*, and Kyle Pennington

***Abstract*—We describe the development of a novel instrument intended for the measurement of the acoustical reflection coefficient of materials. The instrument effectively implements a 1-port, vector-corrected, network analyzer in the acoustic, rather than the electromagnetic, domain. Employing the well-documented methods of error correction familiar to microwave engineers, this instrument permits automated measurement of an acoustic impedance presented to a waveguide port. A dual directional coupler allows a working frequency range of well over an octave. In principle, a set of 6 couplers would allow measurement from 100 Hertz to 50,000 Hertz.**

***Index Terms*—Acoustic measurements, acoustic impedance, acoustic reflection, impedance measurement, impedance tube, vector correction, network analyzer.**

I. Introduction

The vector network analyzer is a familiar and powerful instrument that has been employed for many decades to obtain very accurate impedance measurements in high-frequency systems involving travelling waves and whose operating wavelengths range from tens of metres to fractions of millimetres [1]. Given good impedance standards against which to calibrate, it is capable of very good accuracy and superb resolution and repeatability [2]–[4]. Figure 1(a) shows the notional block diagram of a one-port Vector Network Analyzer (VNA) or Vector Impedance Meter (VIM). Such an instrument consists of a signal source, a mechanism for detection (separation) of the travelling waves carrying energy forward and backwards along a transmission line, an electronics package called a "vector receiver" that is able to measure the magnitude and phase of the travelling waves, and a load whose complex impedance is to be measured. The measurement yields an estimate of the ratio of incident and reflected waves, the reflection coefficient looking into the load, sometimes called the input scattering parameter

$$S_{11} = \Gamma_{\text{LOAD}} = \frac{b_1}{a_1} \tag{1}$$

which is related to the impedance of the unknown load by

$$Z_{\text{LOAD}} = Z_0 \frac{1 + \Gamma_{\text{LOAD}}}{1 - \Gamma_{\text{LOAD}}} \tag{2}$$

where Z_0 is the characteristic impedance of the line connecting the measurement system to the load, a_1 is the incident travelling wave magnitude, and b_1 the reflected wave magnitude.

Figure 1(b) presents a block representation of a microwave impedance meter as it was routinely implemented by the 1950s. Microwave signals can be conveyed in waveguide, and a slotted waveguide provides physical access to the standing wave pattern present in a waveguide transmission line as a result of a given load [5]. The measurement system needs only to measure position and magnitude of the standing wave in the guide. Phase calibration is achieved by temporarily replacing the load with a short (typically a cover plate on the guide flange) and noting the positions of the magnitude minima. The shift in position and depth of the minima, with the load in place of the short, allow the complex ratio of the forward and reverse travelling waves to be found.

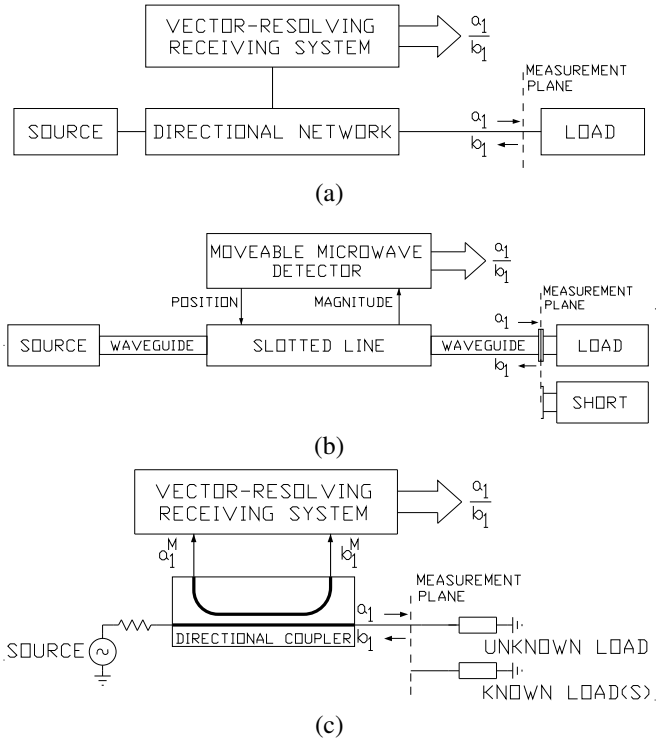

Fig. 1. (a) Notional form of a 1-port vector impedance measurement instrument. (b) Block diagram of an electromagnetic-waveguide impedance measurement system employing a slotted-line and a moveable detector. (c) Block diagram of a modern impedance measurement system using directional couplers.

Figure 1(c) shows the more familiar block diagram of a modern, swept-frequency, 1-port, network analyzer. In this instrument a reflectometer or directional coupler replaces the slotted line [1]. For reasons of convenience and bandwidth most VNAs use coaxial transmission lines below about 67 GHz. For high-power systems and for all systems above 110 GHz waveguide is used. Imperfections in the receivers, directional networks, and interconnecting transmission lines mean that these systems must be calibrated through measurement of a set of known impedance standards. The calibration,

Jonathan Scott is with the School of Engineering, the University of Waikato, Hamilton, New Zealand. e-mail: jonathanscott@ieee.org

Kyle Pennington was with Gallagher Animal Management Systems, Hamilton, New Zealand.

referred to as vector correction, corrects for all imperfections. The process thus provides a path for traceability in the measurement, through the standards. In the case of a single-port impedance measurement, three known standards are required. The theory for such a calibration is presented in the Appendix.

II. Acoustic Impedance Measurement

Measurement of *acoustic* impedance is also of interest. The wavelengths of sound and ultrasound waves span the same range as that of electromagnetic signals from High-Frequency (HF) to Millimetre-Wave (mmW) as addressed by VNAs, and so the measurement challenges in the two domains have a lot in common. Various different approaches for acoustic impedance measurement have been reported in the literature. As in the case for electromagnetic (EM) energy, acoustic energy may be transmitted through a waveguide or "impedance tube". All reported methods employ some sort of waveguide [6]–[16].[1]

The acoustic attenuator method essentially establishes an impedance divider in the guide [6]–[9]. Unfortunately, calibration of such systems leaves a lot to be desired. The most rigorous example is perhaps [8], for which the impedance reference is the calculated values of a series of closed tubes, and whose results rely on the source impedance of the measurement system. In [9] the source is contrived to offer a high characteristic impedance, reducing the dependence of the results upon its value. Rather than an impedance divider, the idea is to deliver a constant acoustic energy, analagous to measuring impedance with a current source. This is achieved with a capillary tube. A single closed tube is used for the calibration. The closed-tube complex impedance, like those of [8], is calculated from theoretical expectations, a mechanism similar to the practice for development of standards in the microwave domain. This approach, where it can be implemented, is accurate provided the capilliary tube is of negligibly-high impedance. While it provides laudable results for the particular application in [9], the capilliary impedance is not accounted for in the calibration, and could affect measurements.

Measurement standards published for the guidance of acoustics companies use the standing-wave ratio (SWR) method [10], [11]. These methods are not exactly convenient, requiring a variety of delicate corrections, and in the end they are essentially equivalent to the slotted-line method of microwave fame, as they work back from the SWR in the guide without resolving the directional components explicitly [12]. The acoustic world is different from the electromagnetic in a number of ways. For example, it is not possible to construct a slotted waveguide as it is in the electromagnetic case, since any breach in the walls will radiate energy. One option is to move a microphone in the guide in some fashion that does not require an open breach in the tube, and trust that the mechanism causes a negligible disturbance, as is anticipated in [10].

[1]It should be noted that there are a number of reports in the literature of ingenious and well-developed acoustic measurements carried out in "free space", without benefit of a guide for the waves, see for example [17]. These must always present difficulty for traceable calibration, as it is not possible to reliably account for the dispersion of the transmission medium. This is the equivalent of attempting electromagnetic calibration in general in dispersive transmission lines such as coplanar waveguide or microstrip [18].

In theory, directional flows can be resolved in both electromagnetic and acoustic waveguides by sampling the magnitude of the standing wave at a number of fixed points. The familiar scalloped magnitude function is then fitted to the measured values, and the magnitudes of maxima and minima deduced once the function is found, as has been done in [13], [14]. After considerable investment of effort, our experience suggests that this method is less than reliable, especially in the presence of noise and measurement uncertainties, because of the need for a numerical fit [16].

An acoustic directional coupler developed using the theories originally used to design microwave waveguide couplers has been reported in [19]. We have constructed a number of such couplers, and assembled an acoustic instrument of the type represented in Figure 1(c). A photograph of a vector impedance meter assembled around one such coupler constructed in transparent acrylic material appears in figure 2. A block diagram of the acoustic hardware appears in figure 3. The waveguide inside dimension is 60mm x 60mm. The coupler-source assembly is made with 14mm-thick walls of clear acrylic. The offset loads are made with 5mm-thick acrylic walls. Each load-coupler junction consists of machined surfaces held in intimate contact by four, 4mm, stainless-steel bolts running through flanges on the loads and screwed into threaded holes tapped into the thicker coupler walls. Audio input and output of signals is achieved with 24-bit resolution using a Presonus AudioBox 1818VSL interfaced to a PC running MatLab. The microphones are Behringer ECM 8000 units. The source transducer is an 8-Ohm Visaton FRS 5 2.5-inch driver. The expected working frequency of the coupler is nominally 1–2kHz, but directivity drops off in the acoustic version less sharply than in the electromagnetic case, and we observed usable directivity from 750Hz at the lower end to 2.25kHz at the upper end.

This class of instrument requires known standards for calibration. As in the case of the rectangular-pipe style of electromagnetic waveguide, there is no such thing as an "open" (infinite impedance) load, so calibrations such as the popular SOLT type routinely employed with coaxial transmission lines [4] are not possible. Nevertheless, full vector calibration can be carried out on 1-port electromagnetic waveguide systems, and this is the approach that we will explore in this manuscript.

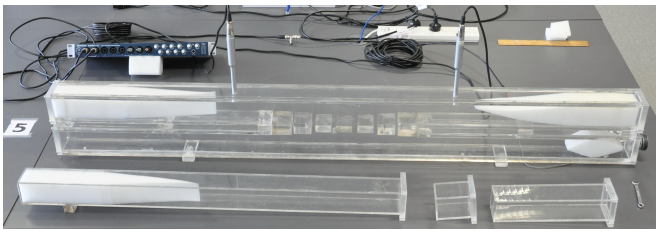

Fig. 2. Photograph of the directional coupler with a loudspeaker source and microphones attached. The source is at the right bottom of the coupler. The coupler has been constructed in transparent acrylic so that the parts are visible. The audio interface with 24-bit ADCs is shown at left rear. Two offset closed pipes and the sliding load are shown in front of the coupler. The ruler in the rear right of the image is 300mm long to show scale.

Calibration of the instrument requires measurement of three

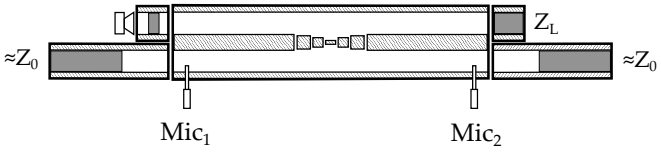

Fig. 3. Block diagram of the acoustic hardware. Microphones sense the sound pressure level in the two side arms of the coupler. The source is a small loudspeaker mounted behind an attenuating pad constructed of the same foam rubber used to make the loads.

known loads, as explained in the appendix. The simplest and most accurate load will be a "short", implemented as a sealed plate over the waveguide opening. In the electromagnetic domain the short standard has a reflection coefficient of unit magnitude and π radians phase. An acoustic short has unit magnitude and zero phase. Provision of the other two known loads is much more complicated, and represents the greatest difficulty in realising an Acoustic Vector-corrected Impedance Meter (AVIM).

III. Sliding Load Standard

An ideal load reflects none of the incident energy. If a load is to be used as a standard, the quality of calibration depends upon the extent to which it is possible to determine the Γ^M_{LOAD} that would result from signals b_1^M and a_1^M measured with such a perfect match presented at the measurement plane. If a load can be constructed whose residual reflection coefficient does not change with position along the waveguide, these desired measurements may be determined irrespective of the actual residual reflection coefficient with judicious choice of positions, using a mathematical process [20]. Consider the construction presented in figure 4. A realisation is visible at the front left of figure 2. Neglecting loss in the offset, and assuming the absorber is imperfect but moveable without change in a uniform guide, it will result in an impedance that describes a circle on the Smith Chart as the load moves along the waveguide. This occurs because the phase alone of the reflected energy is swept with position, and the sliding load would appear to a perfect meter as a circle whose centre lies at the centre of the Smith Chart. The centre of the circle actually measured represents the value that would be returned by the imperfect meter if the load were ideal.

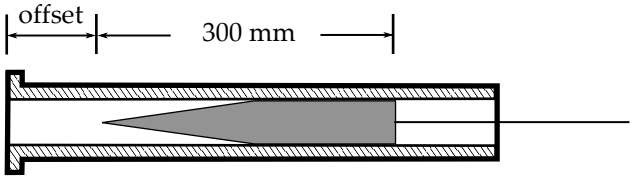

Fig. 4. A sliding load constructed as a wedge-shaped absorbing plunger.

The extent to which one can realise a load whose characteristics do not change as it is moved along a section of lossless waveguide is reflected in the extent to which the returned data represent a circle. The quality of the original load is reflected by the radius of the circle. The proximity of the circle's centre to the centre of the Smith Chart reflects the uncorrected quality of the analyzer hardware, essentially the raw directivity of the system. Thus measurement of a sliding load can say a lot about the quality of the hardware.

Figure 5 presents the result of measuring a sliding load at a number of positions. Note that the frequency range of the measurements extends beyond that over which the coupler is expected to work. The circles are all quite small. Over the expected working frequency range their centres give a reflection coefficient of less than -20dB before calibration. This shows that our coupler is giving good directivity. From the circle radii it can be seen that, at the majority of frequencies, the load has a return loss of 40dB or more, and in all cases it is better than 20dB. This confirms that the load has adequately high return loss. It is also sufficiently invariant with position so that the circle model fits the data very well.

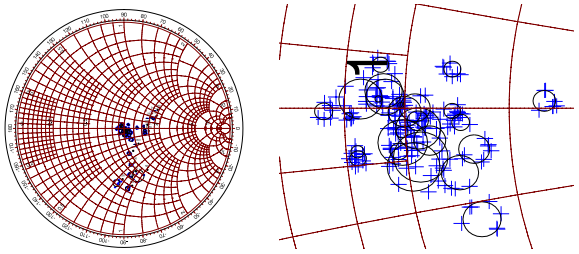

Fig. 5. Uncorrected measurements of the sliding load and the circles fitted to the data. Points nominally outside the usable frequency range of the coupler (800–2200 Hz) have been labelled with the measurement frequency. The right-hand image is a zoom of the centre of the Smith Chart at left.

IV. Offset Short Standards

Since an "open" standard does not exist in waveguide, so-called "offset shorts", in the form of lengths of waveguide sealed at the end, are used to realise the final impedance standards. In the acoustic case, more so than the electromagnetic case, loss in the offsetting line contributes to the perceived impedance of an offset short. In order to establish the impedance presented by an offset short, line loss must be found. We again resort to a sliding method, this time presenting a sliding reflection. The expected result of measuring a sliding reflection is again a circle on the Smith Chart if the line were to be lossless. In the case of a lossy offset transmission line, the action of sliding the reflector results in a spiral trajectory on the Smith Chart, as the length of line increases. The instantaneous radius of the spiral reduces as the length of lossy line increases. If the "slope" of the spiral—that is the rate at which its radius falls with plunger displacement—can be determined from such a measurement it becomes possible to calculate the impedance that is presented by a short of given offset, that is a closed pipe of known length. We fitted spirals to the data at each frequency using the algorithm of Taubin [21].

Figure 6 depicts two spirals plotted from the measured Γ^M_{LOAD} at representative frequencies and a number of positions

of a substantially reflective plunger with known sequential displacements. The center of the spiral at each frequency and the rate of amplitude reduction with distance were found using [21]. Figure 7 shows some results after carrying out this procedure.

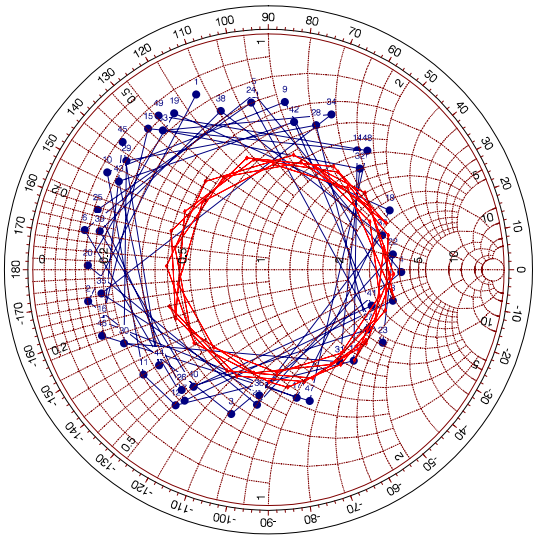

Fig. 6. Example spiral traces on the Smith Chart obtained by plotting measured, uncorrected, reflection coefficients at individual frequencies as a function of plunger position. Example spirals are shown at 1kHz and 2kHz. The data at 2kHz is shown in blue with the data points numbered sequentially with plunger position. Data at 1kHz is red with diamond symbols.

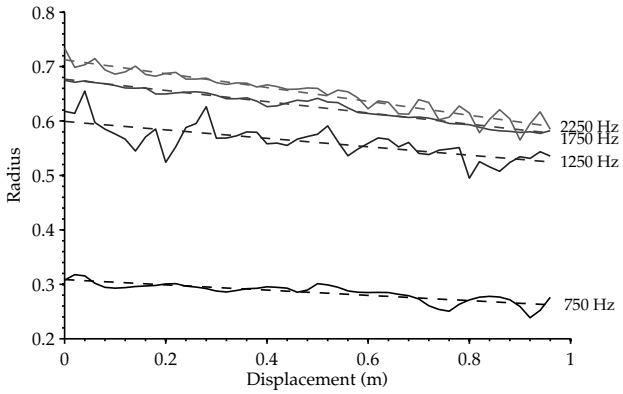

Fig. 7. Measured values of spiral radius against plunger displacement at some example frequencies (solid lines) compared to the values predicted from the fit (dashed lines).

Integrating the results, figure 8 shows the estimated loss in dB per meter as a function of frequency. Using this data, the expected impedances of the two offset shorts visible at the front in figure 2 were calculated.

Different offset loads have been characterised. The requirements for a robust calibration are that the three standard impedances used be spaced apart on the Smith Chart. Since we rely on a load, a short, and an offset short, the length of the offset needs to be distant from a multiple of half a wavelength, in order that the two impedance values whose

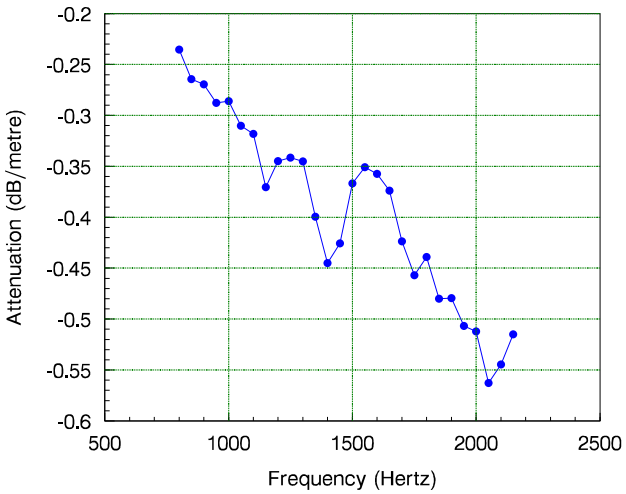

Fig. 8. Plot of the loss per metre of sound waves propagating through acrylic waveguide as a function of frequency found from linear fits to the estimates of spiral radii.

reflection coefficient approaches 1 do not coincide. It is usually considered that a spacing of at least 30^o on the chart is satisfactory. For the spread of frequencies here at least two shorts, in addition to the zero-length one, will be required.

V. Consistency Check

At any single frequency the AVIM is calibrated using the plain short, the sliding load in a number of positions, and one or other of the offset shorts. The particular offset short is selected according to the relative proximity of the expected impedance to that of the plain short. Figure 9 shows the result of measuring the 300mm offset short with the instrument once calibration has been carried out. Of course, the result is a perfect reproduction of its calculated impedance at frequencies where that standard is used as one of the three reference impedances. At other frequencies the errors of the instrument are evident. The errors after calibration appear to be in the region of ± 1.0 to 1.5dB, which corresponds to a range of 12–19% of uncertainty in sound pressure level (SPL).

VI. Measurement of Soil and Pasture

Our interest in this work is to characterise the acoustic "visibility" of pasture above soil. Our pasture sample was freshly-cut perennial ryegrass, averaging 20cm in height, representative of what is found in paddocks and open land in dairy areas of New Zealand. It was transferred to the test waveguide promptly, preserving the soil integrity, and it was maintained in typical healthy conditions during the measurement. We repeated measurements to ensure that the sample was not degrading or materially changing. The entire process took only a few hours.

We first measured the reflection coefficient of the pasture, still rooted in a compacted soil sample, essentially a small square of soil with grass growing up from it extracted without disturbance. This was placed in the same open-ended length

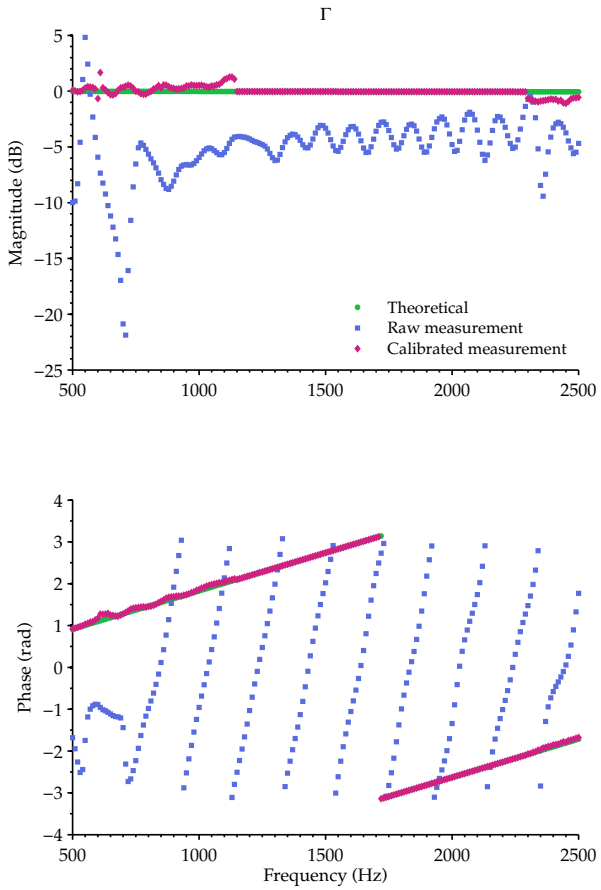

Fig. 9. Plot of the magnitude and phase of the first offset short. The regions where the calibration did not use this particular standard show the errors arising from the standard definitions we have used. Elsewhere the result is perfect to numerical precision by definition.

of transparent acryllic waveguide with 60mm x 60mm cross section and the same 5mm wall thickness used for the characterisation of offset loss as described above. We then measured the acoustic reflection coefficient of a sample of compacted soil by itself, and a sample of harvested pasture, both in the same sample guide. The results of these measurements are depicted in figure 10.

We should ignore the results below about 800Hz and above about 2200Hz where coupler performance is falling away. In the usable range, the grass shows a reflection coefficient of -20dB or smaller. This indicates that in this frequency range the grass reflects very little energy, less than 1%, with all of it being either absorbed or transmitted. We attribute the ripples visible at higher frequencies to interference with equally-small reflections from the environment behind the pasture material, an absorber in front of the open-end of the sample tube.

On the other hand, the compacted soil sample reflected about half of the incident power at 1kHz. The fraction reflected fell steadily with frequency so that at 2kHz three-quarters of the power is absorbed and one-quarter reflected.

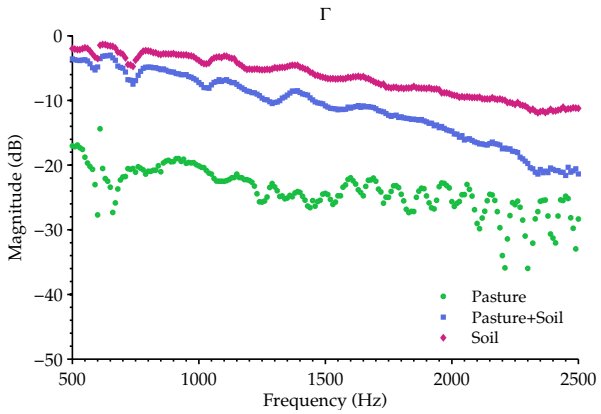

Fig. 10. Plot of the magnitude of S_{11} with samples in an acoustic waveguide. The grass sample had the sliding load behind it when no soil was present. The presence of a load behind the soil sample had no effect.

When grass and soil are observed together, we see that 3–6dB less energy is returned than in the case of the soil alone. Since a relatively small fraction of energy is reflected from the grass, as evidenced from the grass-alone trace, we must conclude that the grass is absorbing a good deal of the energy, 1.5–3dB on each pass (the 3–6dB represents loss from a return trip through the grass). We may thus infer that

1) Soil reflects sound energy relatively well at low frequencies;
2) Soil reflects less energy at higher frequencies (2kHz and above) than it does at low frequencies (800Hz and below);
3) Grass reflects little acoustic energy, about 1%, with no obvious trend with frequency;
4) Grass absorbs energy, about 10dB/meter at 1500Hz, with absorption increasing at higher frequencies.

These observations account for the inability of ultrasonic-based pasture meters to obtain a reliable measurement of the height of pasture. Rather, they achieve only a measurement of the distance to the top of the sward, since the echo from the ground is weak because of both the low reflection from the soil and the attenuation of the pasture.

VII. Conclusion

We have constructed a vector impedance meter, essentially by realising the first 1-port vector network analyzer (VNA) in the acoustic rather than the electromagnetic domain. The directivity of the hardware is adequate for calibration over a frequency ratio of almost 3:1. We believe the accuracy to be around ± 1.5dB, limited by the availability of techniques and standards against which the instrument is calibrated. There remains much work to be done on this aspect of the instrument.

The electromagnetic VNA advanced over a number of decades to provide fast, convenient measurement of impedance with very high accuracy and traceability. We have already taken advantage of several of the advances applied to the EM version of VNAs to speed development of this acoustic version. The current instrument represents a level of sophistication roughly corresponding with that of the VNA of 3

decades ago. This instrument promises to provide the same advantages in the acoustic realm as are afforded by the VNA in the EM domain. We believe it will prove to have application in architecture, sound reproduction, musical instrument design, biomedical diagnostics, and agriculture.

VIII. Acknowledgement

This work was supported by Gallagher Animal Management Systems, the Ministry of Business, Innovation, and Employment, New Zealand, and the Faculty of Science and Engineering at the University of Waikato. The authors wish to express their thanks especially to Kerry Bodman and Tony Smith.

Appendix
Calibration of a 1-port Vector Meter

The waves actually measured by the receiving system in instruments of the type portrayed in figure 1(c) are a_1^M and b_1^M. By definition we can write down equation (1) but the analyzer actually measures

$$\Gamma_{\text{LOAD}}^M = \frac{b_1^M}{a_1^M} \tag{3}$$

where the measured signals b_1^M and a_1^M have been corrupted by the imperfections of the directional detection hardware. We seek a method of obtaining Γ_{LOAD} given Γ_{LOAD}^M.

Using the well-known technique of modeling the circuit as an ideal VNA connected to the port through an error network [22], the flow diagram of figure 11 follows from the theory of signal graphs [23], [24] and some algebra yields the equation:

$$\Gamma_{\text{LOAD}}^M = I_{11} + \frac{I_{12}I_{21}\Gamma_{\text{LOAD}}}{1 - I_{22}\Gamma_{\text{LOAD}}} \tag{4}$$

which may be manipulated to give the correction equation:

$$\Gamma_{\text{LOAD}} = \frac{\Gamma_{\text{LOAD}}^M - E_{d_1}}{E_{r_1} + E_{s_1}(\Gamma_{\text{LOAD}}^M - E_{d_1})} \tag{5}$$

where the error terms $E_{d_1} = I_{11}$, $E_{s_1} = I_{22}$, and $E_{r_1} = I_{12}I_{21}$ are the three error coefficients required at each calibration frequency. Their values (at each individual frequency) are determined by measuring three known terminations, typically two reflective and a resistive load. This determination of the error coefficients ("calibration") is accomplished by observing that equation 4 may be manipulated to become:

$$\Gamma_{\text{LOAD}}^M = E_{d_1} + (E_{r_1} - E_{s_1}E_{d_1})\Gamma_{\text{LOAD}} + E_{s_1}\Gamma_{\text{LOAD}}^M\Gamma_{\text{LOAD}} \tag{6}$$

which, after a change of variable, has the form

$$k_1 = x + k_2 y + k_3 z \tag{7}$$

where the k_i are obtained from measurements of the known reflection coefficients, and x, y and z quickly yield $E_{d_1} = x$, $E_{s_1} = z$ and $E_{r_1} = y + xz$. After measuring three known loads the solution of three complex linear equations in three unknowns may be carried out with standard matrix arithmetic, giving values for the error coefficients. Thereafter equation (5) yields Γ_{LOAD} given Γ_{LOAD}^M.

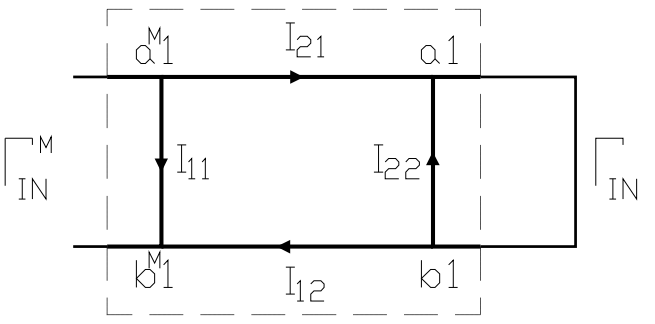

Fig. 11. Flow diagram for analysis of errors in a 1-port measurement network. The load impedance Γ_{IN} appears as Γ_{IN}^M as a result of the error network represented by the coefficients I_{xy}.

References

[1] Rytting, Doug, "ARFTG 50 year network analyzer history", *IEEE MTT-S International Microwave Symposium Digest*, 2008, pp11–18.

[2] Rytting, Douglas Kent "Network Analyzer Accuracy Overview", *58th ARFTG Conference Digest*, volume 40, Fall 2001, pp1–20.

[3] Marks, R.B., Jargon, J.A., and Rytting, D.K. "Accuracy of lumped-element calibrations for four-sampler vector network analyzers", *IEEE MTT-S International Microwave Symposium Digest*, Volume: 3, 1998, pp1487–1490, 1998.

[4] Jargon, J.A., Marks, Roger B., and Rytting, D.K., "Robust SOLT and alternative calibrations for four-sampler vector network analyzers", *IEEE Transactions on Microwave Theory and Techniques*, Volume:47, Issue:10, 1999, pp2008–2013.

[5] Das, Annapurna, and Sisir Das, *Microwave Engineering* McGraw-Hill Education, 2009, ISBN 0-07-066738-1.

[6] Smith, J., Fritz, C. and Wolfe, J. "A new technique for the rapid measurement of the acoustic impedance of wind instruments", *Proc. Seventh International Congress on Sound and Vibration*, 4–7 July 2000, Garmisch-Partenkirchen, Germany, Vol III, pp.1833–1840.

[7] De Blok, C. M., and R. F. M. Van den Brink, "Direct-Reading One-Port Acoustic Network Analyzer", *Journal of the Audio Engineering Society*, vol. 41, no. 4, April 1993, pp231–238.

[8] D. H. Keefe, R. Ling, and J. C. Bulen, "Method to measure acoustic impedance and reflection coefficient," J. Acoust. Soc. Am., vol. 91, pp. 470–485, January 1992.

[9] Kausel, W., "Bore reconstruction of tubular ducts from its acoustic input impedance curve," *IEEE Transactions on Instrumentation and Measurement*, vol. 53, no. 4, August 2004, pp. 1097–1105.

[10] ISO 10534-1:1996, "Acoustics—determination of sound absorption coefficient and impedance in impedance tubes—Part 1: Method using standing wave ratio".

[11] ASTM Standard C384, 2004, "Standard test method for impedance and absorption of acoustical materials by impedance tube method".

[12] Clifton, Brian J. "Precision Slotted-Line Impedance Measurements Using Computer Simulation for Data Correction", *IEEE Transactions on Instrumentation and Measurement*, Volume: 19, Issue: 4, 1970, pp358–364.

[13] William Johnston, "The Construction and Initial Measurements of an Acoustic Reflectometer", Internal report, Colorado State University, John Price Advisor. http://www.colorado.edu/physics/Web/reu/Projects/Projects2007/WilliamJohnston.pdf See also http://spot.colorado.edu/~pricej/acoustics.html.

[14] John Price, "Acoustic VNA User's Guide", January 2008. http://spot.colorado.edu/~pricej/pdfdocs/AVNAUser'sGuide.pdf

[15] Peter D'Antonio, and Brian Rife, "The use of multi-microphone measurements of directional and random incidence acoustical coefficients", *Journal of the Acoustical Society of America*, April 2012; 131(4):3284.

[16] Kyle Pennington, Jonathan Scott, and Kerry Bodman, "Determining Acoustical Directionality in an Impedance Tube Using Multiple Fixed Microphones", *Proceedings of the 18th ENZCon*, Palmerston North, 21–22 November, 2011, pp73-76.

[17] Chen, T., Ho Bong and H.R. Zapp, "Impedance and attenuation profile estimation of multilayered material from reflected ultrasound," *IEEE*

Transactions on Instrumentation and Measurement, vol. 40, no. 4, August 1991, pp. 787–791.
[18] Jonathan Scott, "Investigation of a Method to Improve VNA Calibration in Planar Dispersive Media Through Adding an Asymmetrical Reciprocal Device", *IEEE Transactions on Microwave Theory and Techniques*, vol. 53, no. 9, September 2005, pp 3007–3013.
[19] Lagasse, P., "Realisation of an acoustical directional coupler", *Journal of sound and vibration*, 15(3), April 1971, pp367–372.
[20] H. C. Heyker, "The Choice of Sliding Load Positions to Improve Network Analyzer Calibration", 12th European Microwave Conference, Helsinki, September 1982, pp429–434.
[21] Taubin, Gabriel, "Estimation of planar curves, surfaces, and nonplanar space curves defined by implicit equations with applications to edge and range image segmentation," *IEEE Transactions on Pattern Analysis and Machine Intelligence*, vol. 13, no. 11, pp 1115–1138, November 1991.
[22] Rehnmark, Stig "On the Calibration Process of Automatic Network Analyzer Systems", *IEEE Transactions onMicrowave Theory and Techniques*, Volume:22, Issue:4, 1974, pp457–458.
[23] Mason and Zimmerman, *Electronic Circuits, Signals & Systems* Wiley, 1960.
[24] Kuhn, "Signal Flow Graphs", Microwave Journal, November 1963, pp 59+.

Jonathan Scott (M'80–SM'99) is the Foundation Professor in Electronic Engineering at the University of Waikato in Hamilton, New Zealand. From 1998 to 2006 he was with the Hewlett-Packard/Agilent Technologies, Microwave Technology Center in Santa Rosa, where he was responsible for advanced measurement systems. In 1998 he was Chief Engineer at RF Technology in Sydney. He was with The University of Sydney in the Department of Electrical Engineering prior to 1997. He is a Professorial Fellow of Macquarie University. Professor Scott has authored over 100 refereed publications, and he holds a number of patents.

Kyle E. Pennington was born in Auckland, New Zealand, in 1986. He received the BE degree in electronic engineering from the University of Waikato in 2009. Since 2010, he has been working on completing his PhD in the field of acoustics.

C

Smith Chart

The Smith chart is a tool commonly used by RF engineers to display and assist in solving impedance problems. Figure C.1 shows an example of a Smith chart. They are most frequently scaled to a normalised impedance

$$z = \frac{Z_L}{Z_0} \tag{C.1}$$

where Z_L is the impedance of the load and Z_0 is the characteristic impedance of connecting impedance line. The chart contains imaginary impedances from negative infinity to positive infinity and all positive real impedances.

The Smith chart also provides a fast method to convert the normalised impedance to a reflection coefficient which is represented by the distance from the centre of the chart, 0 at the centre and 1 at the outside edge. This can be used to match a load to the impedance line by increasing or decreasing the impedance in order to move the load to the centre of the chart.

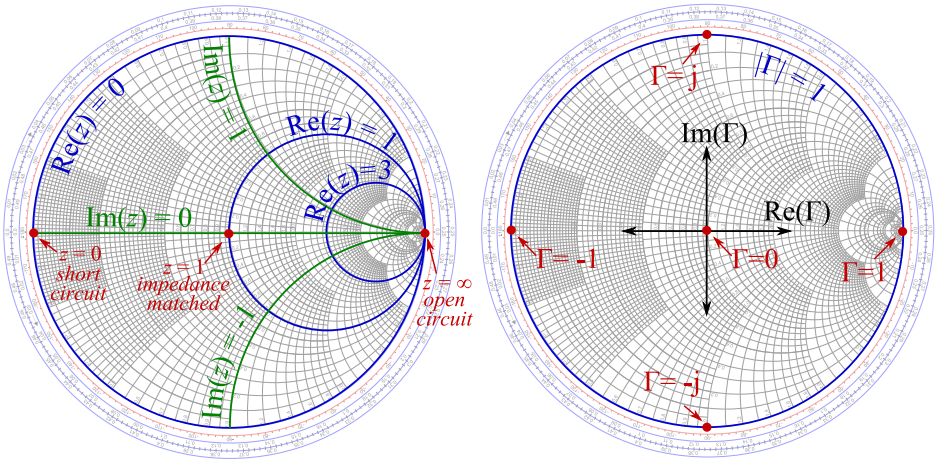

Figure C.1: Example of a Smith Chart showing the positions of the important load impedances and reflection coefficients.

D

Scattering Parameters

Scattering parameters can be used to describe a steady-state network. For a two-port network, the parameters are the ratios of input, a, and output, b, signals travelling to and from each of the two ports. Figure D.1 shows a the scattering parameters for a two-port network. As an example, S_{21} is the ratio of $\frac{b_2}{a_1}$ and S_{11} is the ratio of $\frac{b_1}{a_1}$ or the complex reflection coefficient.

A signal flow graph is another way of representing the input and output signals at the ports of a network where the right-travelling signals are on the top and the left-travelling signals are on the bottom. Reflected portions of the signals are shown as a vertical line with an arrow connecting the left and right travelling waves [78,83].

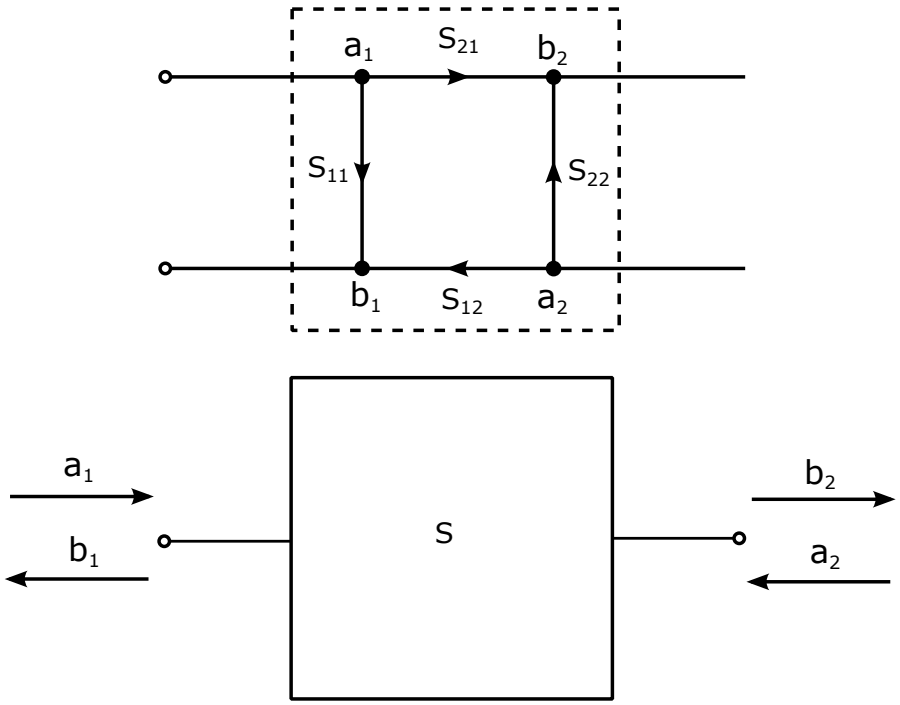

Figure D.1: Scattering parameters and the equivalent signal flow graph.

E
Hardware

E.1 Acoustic Directional Coupler

The dimensions of the acoustic directional coupler are shown in Figure E.1.

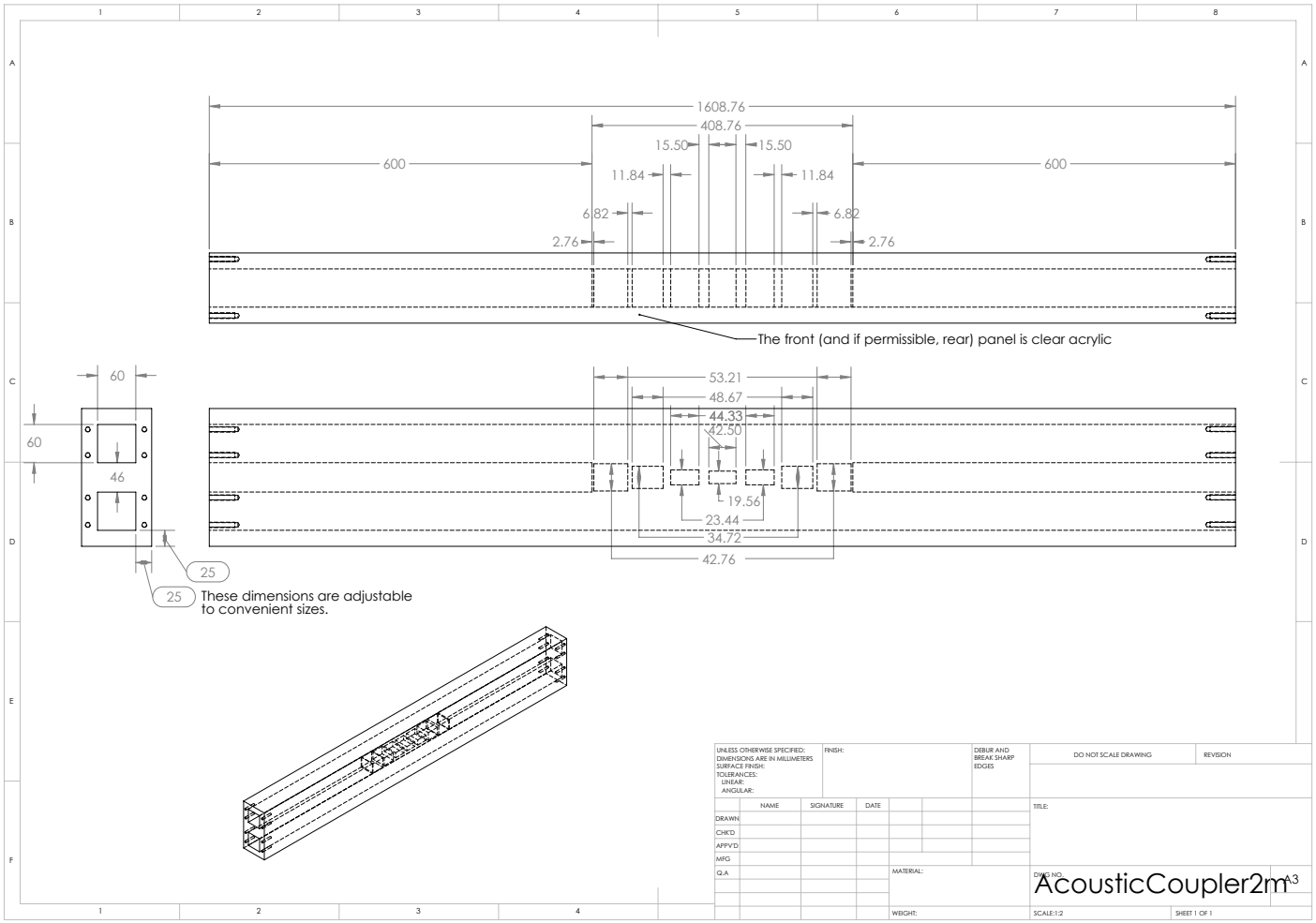

Figure E.1: Technical drawing of the acoustic directional coupler.

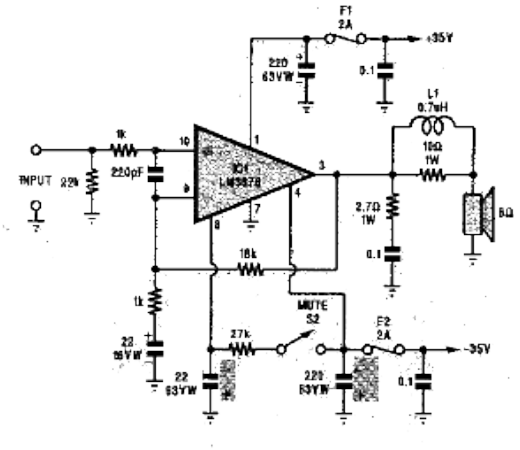

Figure E.2: Schematic diagram of the 50 W audio amplifier.

E.2 50 W Audio Amplifier

The schematic diagram of the audio amplifier is shown in Figure E.2.

E.3 Microphone Pre-amps

The schematic diagram of the microphone pre-amps is shown in Figure E.3 and the realisation appears in Figure E.4.

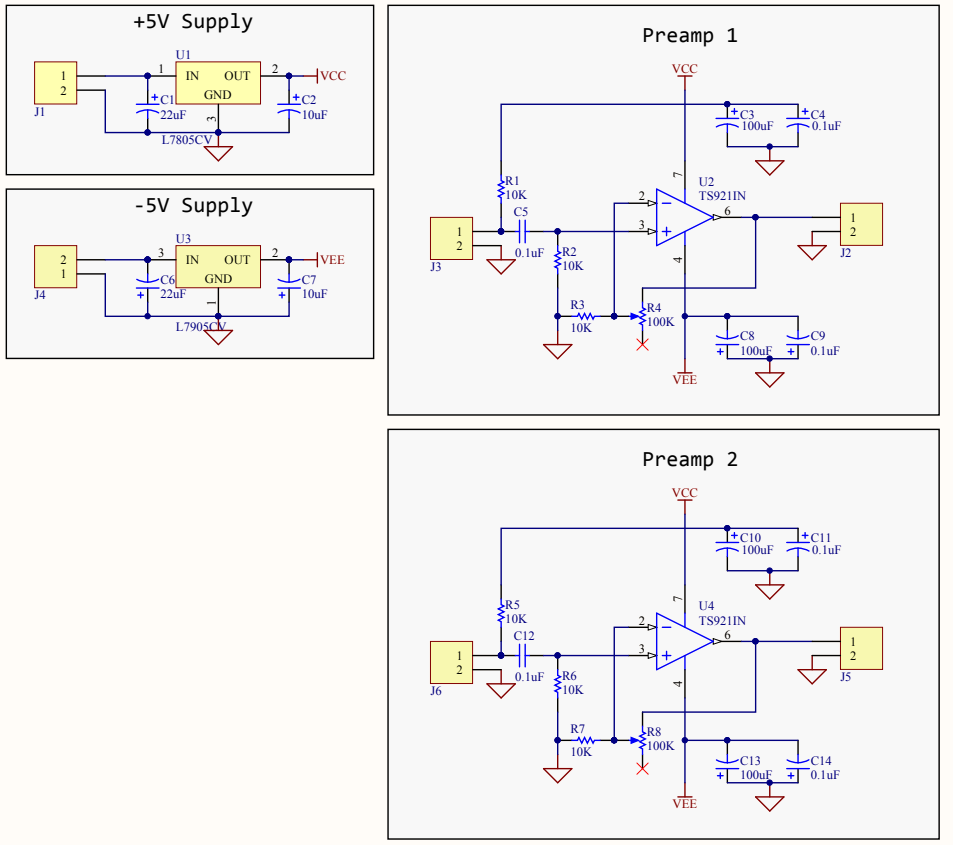

Figure E.3: Schematic diagram of the pre-amp circuit.

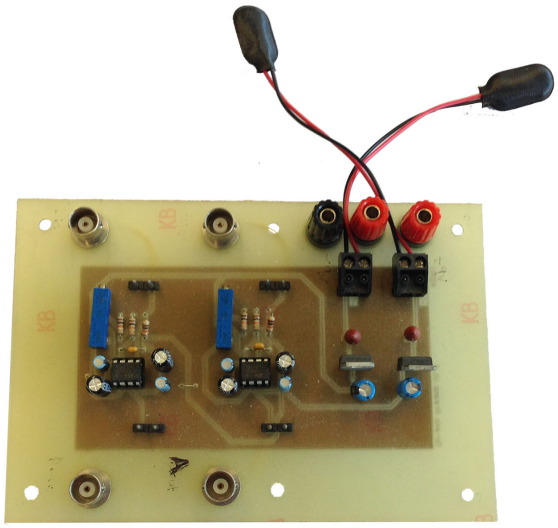

Figure E.4: Photograph of the pre-amp PCB.

F
Software

F.1 Impedance Tube Confidence

```
micLoc = [-0.100, -0.100, -0.145, -0.213, -0.381, -0.803];
%%%%%%%%%%%%%%%%%%%%%%%%%%
% Generate Synthetic Data
%%%%%%%%%%%%%%%%%%%%%%%%%%
f = 10:10:5000;
x = 0:-0.001:-1;
nLocs = size(micLoc,2);
nFreq = size(f,2);
nX = size(x,2);
y = zeros(nFreq,nLocs);
for k=1:nFreq
    for m=1:nX
        freq = f(k);
        A0 = 1;
        Ai = 0;
        R0 = 1;
        Ri = 0;
        alpha = 0;
        y(k,m) = waveEq(A0,Ai,R0,Ri,alpha,x(m),freq);
```

```
20      end
21  end
22
23  z = 0;
24  for m=1:(nLocs-1)
25            figure(1);
26            for n=(m+1):nLocs
27           z = z+1;
28           for k=1:nFreq
29               ym = waveEq(A0,Ai,R0,Ri,alpha,micLoc(m),f(k));
30               yn = waveEq(A0,Ai,R0,Ri,alpha,micLoc(n),f(k));
31               phaseShift = diffAngle(0,Ai - Ri)/2;
32               wl = 344/f(k);
33               quarterWl = wl/4;
34               wlShift = wl*phaseShift/(2*pi);      %first
                     maximum occurs here on x-axis
35               seperation = abs(micLoc(n) - micLoc(m));
36               remConf = rem(seperation, wl/2);
37               sepConfidence = abs(remConf)/quarterWl;
38               if sepConfidence > 1
39                    sepConfidence = 2 - sepConfidence;
40               end
41
42               posConfidence1 = rem((micLoc(m) - wlShift) / -
                     quarterWl,1);
43               posConfidence1 = posConfidence1 - 0.5;
44               posConfidence1 = posConfidence1*2;
45               posConfidence1 = abs(posConfidence1);
46               posConfidence2 = rem((micLoc(n) - wlShift) / -
                     quarterWl,1);
47               posConfidence2 = posConfidence2 - 0.5;
48               posConfidence2 = posConfidence2*2;
49               posConfidence2 = abs(posConfidence2);
50
51               totalConf(z,k) = sepConfidence*posConfidence1*
                     posConfidence2;
52
53        end
54
```

```
55          plot(f, totalConf(z,:));
56            hold all;
57        end
58    end
59    maxConf = max(totalConf,[],1);
60    figure(); colorMap = kool_colors(2,1);
61    plot(f, maxConf*100, 'Color', colorMap(1,:)) xlabel('
        Frequency␣(Hz)') ylabel('Confidence␣(%)')
```

F.2 Fitting Algorithm

Listing F.1: Fitting error algorithm program listing.

```
1   function y=recfun(a, Xexp, Yexp, f)
2       x = Xexp;
3       A0 = a(1);
4       Ai = a(2);
5       R0 = a(3);
6       Ri = a(4);
7       alpha = a(5);
8       alpha = 0;      % comment to enable decay optimisation
9       Ycal = waveEq(A0, Ai, R0, Ri, alpha, x, f);
10      realErr = real(Ycal) - real(Yexp);
11      imagErr = imag(Ycal) - imag(Yexp);
12      y = realErr.^2 + imagErr.^2;
13      ave = (abs(Ycal) + abs(Yexp))/2 + 0.00001;
14      y = y ./ ave;
15  end
```

Listing F.2: Wave equation program listing.

```
1   function y=waveEq(A0, Ai, R0, Ri, a, x, f)
2       k = 2*pi*f/344;
3       A = A0*exp(1i*Ai);
4       R = R0*exp(1i*Ri);
5       y = A*exp(1i*(k*(-x)) - x*a) + R*exp(1i*(k*(x)) + x*a);
6   end
```

F.3 VNA Acquisition

The graphical user interface (GUI) is shown in Figure F.3 which sets up automated testing and frequency sweeps.

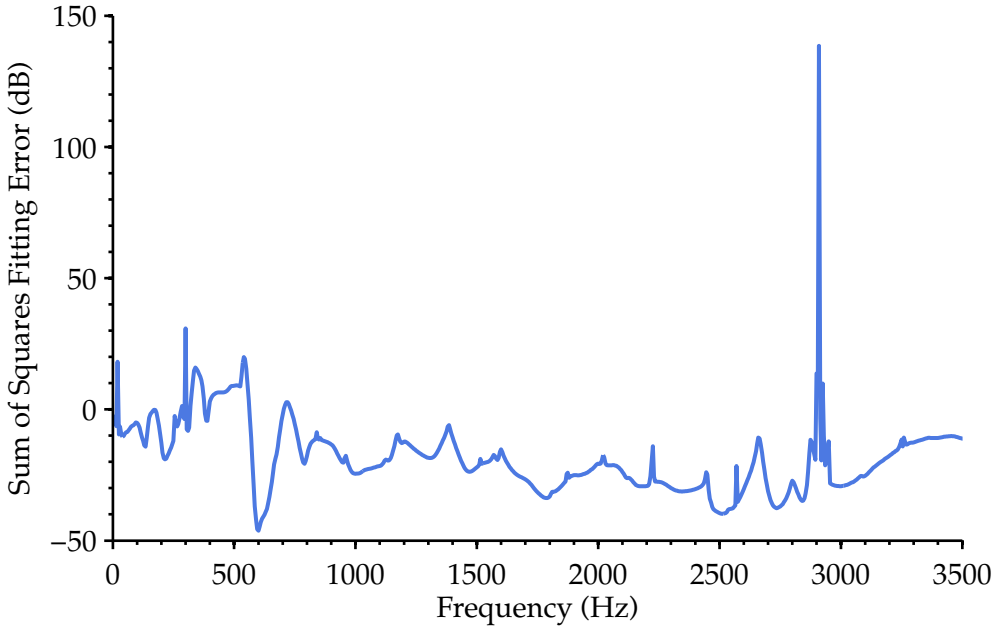

Figure F.1: Sum of least squares error for an acoustic short.

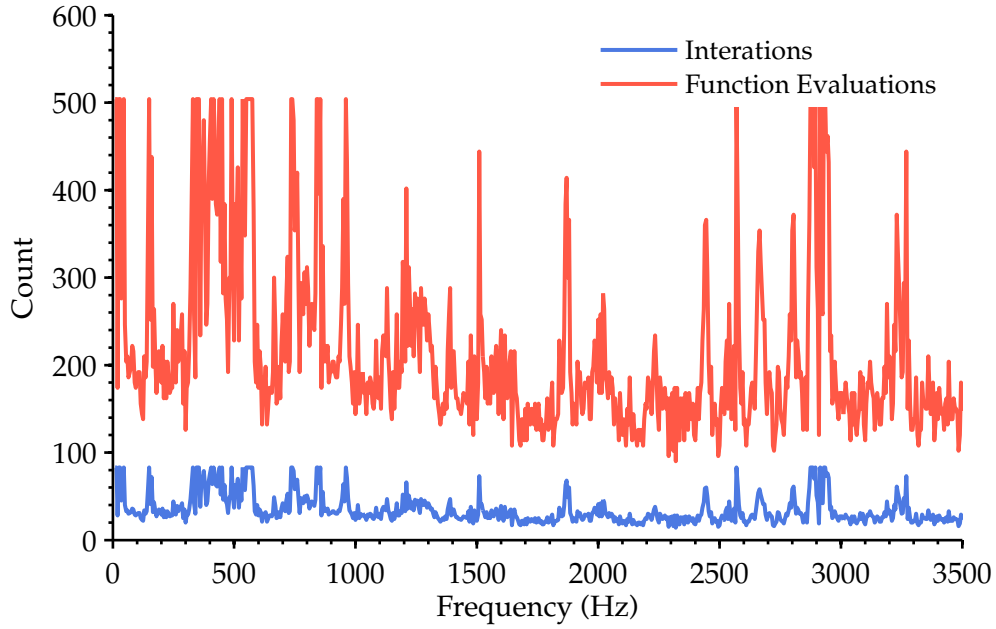

Figure F.2: Iterations the optimiser performed at each frequency for an acoustic short. The maximum function evaluations of 500 can be seen.

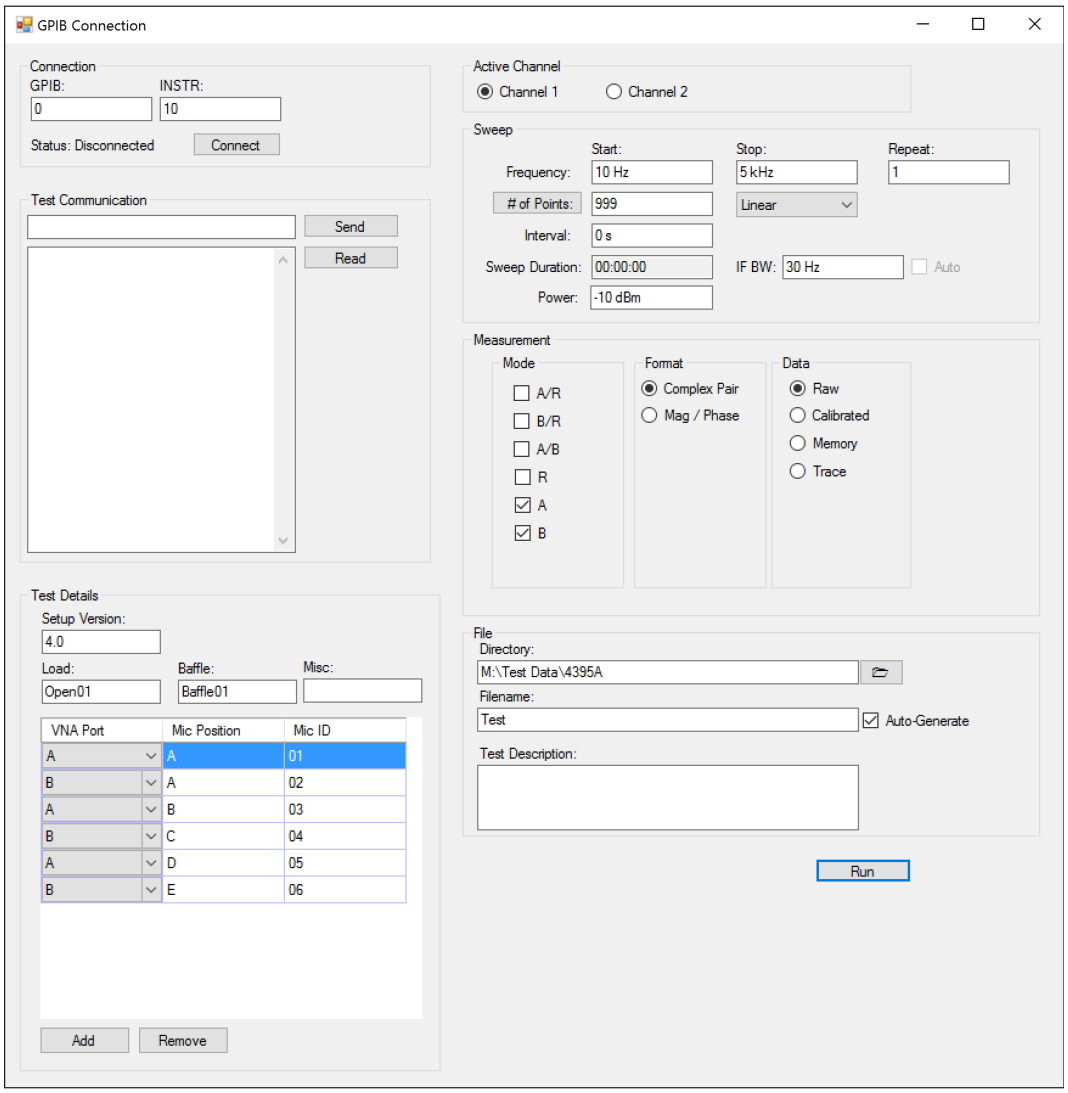

Figure F.3: Graphical user interface of the custom 4395A interface software.

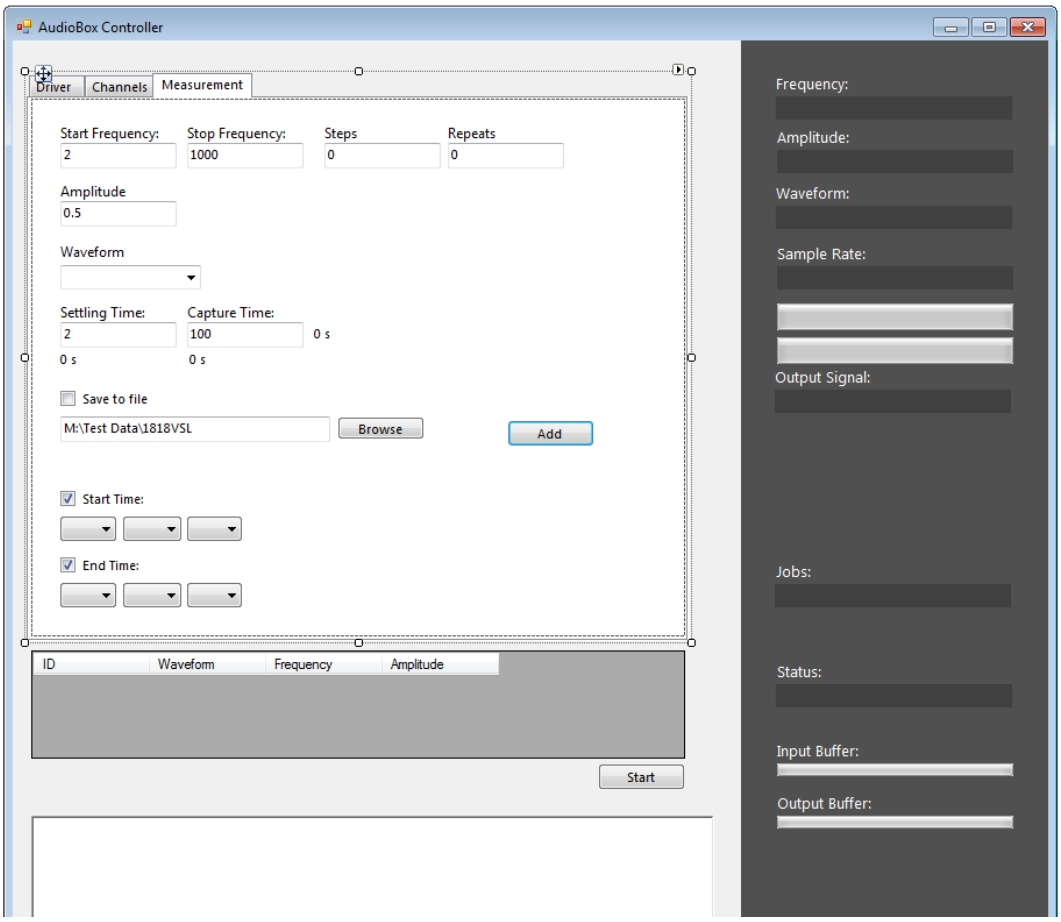

Figure F.4: Graphical user interface of the AudioBox Controller software.

F.4 AudioBox Acquisition

The GUI is shown in Figure F.4 used to interface with the AudioBox and collect data.

F.5 GenerateSweep

Listing F.3: GenerateSweep program listing. Used to convert raw data files to compensated data files.

```
1 function [f, m] = GenerateSweep(rawDir, varargin)
2 % file: GenerateSweep.m
3 % version 1.0 - 31/10/2012
4 % This matlab subroutine reads all Raw Data Files (.rdf) in a
      directory and
5 % compensates the gain of each microphone, then outputs a
      Compensated Data
6 % File (.cdf).
```

```
7  %%%%%%%%%%%%%%%%%%%%%%%%
8  % Optional arguments
9  %%%%%%%%%%%%%%%%%%%%%%%%
10 % 'graph' 'on'|'off'
11 graph = false; %default
12 overwrite = false;
13 cleanup = false;
14 settling = 0;
15 N = length(varargin);
16 if mod(N,2)==1
17     error('gainComp: An odd number of optional arguments!');
18 end
19 for j=1:2:N
20     arg = varargin(j);
21     arg = cell2mat(arg);
22     switch arg
23         case 'graph'
24             if strcmp(varargin(j+1),'on')
25                 graph = true;
26             end
27         case 'overwrite'
28             if strcmp(varargin(j+1),'true')
29                 overwrite = true;
30             end
31         case 'cleanup'
32             if strcmp(varargin(j+1),'true')
33                 cleanup = true;
34             end
35         case 'settling'
36             settling = str2double(cell2mat(varargin(j+1)));
37         otherwise
38     end
39 end
40 %%%%%%%%%%%%%%%%%%%%%%%%
41 % Setup
42 %%%%%%%%%%%%%%%%%%%%%%%%
43 newPath = [rawDir '/sweep.cdf'];            % remove old extension
       and new
44 exists = (exist(newPath,'file') ~= 0);      % check if output file
       already exists
45 haveData = false;
46 %%%%%%%%%%%%%%%%%%%%%%%%
47 % Read Files and Process
48 %%%%%%%%%%%%%%%%%%%%%%%%
```

```
49 if ~exists || overwrite || graph
50
51     cd(rawDir);
52     dirInfo = dir('*.rdf');
53     numOfFiles = length(dirInfo);
54     h = waitbar(0,'Initializing waitbar...');
55
56     for i=1:numOfFiles
57         [header data] = LoadRawCapture(dirInfo(i).name);
58         f(i) = header.frequency;
59         Fs = header.samplerate;        % Sampling frequency
60         T = 1/Fs;                      % Sample time
61         L = size(data, 1);             % Length of signal
62         t = (0:L-1)*T;                 % Time vector
63     %    FFT PLOT
64         if graph
65             figure(1);
66             clf;
67             plot(data(:,1),'b')
68             hold on;
69             plot(1000*t,data(:,2),'r')
70             xlabel('time (milliseconds)')
71             ylabel('Y(t)')
72             title(['Frequency = ' int2str(f(i)) 'Hz']);
73             legend('a','b');
74            % set(gcf, 'Position', get(0,'Screensize')); % Maximize
                  figure.
75         end
76         % determine phase and magnitude using linear regression
77         m(i,:) = FilteredDFT(data, f(i), Fs, 'settling', num2str(
               settling));
78         haveData = true;
79
80         if cleanup
81             delete(dirInfo(i).name);
82         end
83
84         waitbar(i/numOfFiles,h,'Processing...')
85     end
86     close(h)
87 end
88 %%%%%%%%%%%%%%%%%%%%%%%%%
89 % Read Saved Data
90 %%%%%%%%%%%%%%%%%%%%%%%%%
```

```
91  if ~haveData
92      [header data] = LoadDataFile(newPath);
93      [f, m] = ConvertToComplex(data);
94  end
95  %%%%%%%%%%%%%%%%%%%%%%%%
96  % Plots
97  %%%%%%%%%%%%%%%%%%%%%%%%
98  if graph
99
100     figure();
101     subplot(2,1,1);
102     plot(f,mag2db(abs(m(:,1))));
103     hold all;
104     plot(f,mag2db(abs(m(:,2))));
105     ylabel('Magnitude (dB)');
106     subplot(2,1,2);
107     plot(f,angle(m(:,1)));
108     hold all;
109     plot(f,angle(m(:,2)));
110     ylabel('Phase (rad)');
111     xlabel('Frequency (Hz)')
112 end
113 %%%%%%%%%%%%%%%%%%%%%%%%
114 % Write data to file
115 %%%%%%%%%%%%%%%%%%%%%%%%
116
117 if overwrite || ~exists
118
119     fid = fopen(newPath, 'w');
120
121     % Write file header
122     fprintf(fid, '%-20s%s\r\n', 'Device:', header.device);
123     fprintf(fid, '%-20s%s\r\n', 'Date:', header.date);
124     fprintf(fid, '%-20s%s\r\n', 'Waveform:', header.waveform);
125     fprintf(fid, '%-20s%d\r\n', 'Sample Rate (Hz):', header.
            samplerate);
126     fprintf(fid, '%-20s%d\r\n', 'Start Freq (Hz):', f(1));
127     fprintf(fid, '%-20s%d\r\n', 'Stop Freq (Hz):', f(end));
128     fprintf(fid, '%-20s%d\r\n', 'Steps:', size(f,2));
129     fprintf(fid, '\r\n');
130     % write column header
131     fprintf(fid, '%-14s', 'Freq (Hz)');
132     for j=1:size(m,2)
133         fprintf(fid, '\t%-14s', 'Magnitude');
```

```
134             fprintf(fid, '\t%-14s', 'Phase(rad)');
135         end
136         fprintf(fid, '\r\n');
137         % write data
138         for k=1:size(m,1)
139             fprintf(fid, '%-+14E', f(k));
140             for j=1:size(m,2)
141                 mag = abs(m(k,j));
142                 phs = angle(m(k,j));
143                 fprintf(fid, '\t%-+14E', mag);
144                 fprintf(fid, '\t%-+14E', phs);
145             end
146             fprintf(fid, '\r\n');
147         end
148         fclose(fid);
149     end
```

F.6 Processing

Listing F.4: Discrete Fourier transform algorithm.

```
1  T = 1/Fs;                          % Sample time
2  L = size(data, 1);                 % Length of signal
3  t = (0:L-1)*T;                     % Time vector
4  X = ones(L,3);                     % DC
5  X(:,2) = cos(2*pi*f*t)';           % Real
6  X(:,3) = sin(2*pi*f*t)';           % Imaginary
7  beta = X \ data;
8  amp = sqrt(beta(2,:).^2 + beta(3,:).^2);
9  phase = atan2(beta(3,:), beta(2,:));
10 m = amp.*exp(1i*phase);
```

F.7 Vector Calibration

Listing F.5: 1-Port calibration program listing.

```
1  N = size(gmeas,1);
2  estd = zeros(N,3);
3  for m = 1:N
4      matA = [1    gstd(m,1).*gmeas(m,1)    gstd(m,1);
5              1    gstd(m,2).*gmeas(m,2)    gstd(m,2);
6              1    gstd(m,3).*gmeas(m,3)    gstd(m,3)];
```

```
7     B = gmeas(m,:)';
8     estd(m,:) = matA\B;
9     estd(m,3) = estd(m,3) + estd(m,1)*estd(m,2);
10 end
```

F.8 Theoretical Calibration Standard Generation

Listing F.6: Calibration standard generation program listing.

```
1  function gamma = GenerateCalStandard(f, type, offset, varargin)
2  %
3  %   generateCalStandard
4  %   Generates the ideal refkection coefficients of cal standards
       over the desired
5  %   frequency range.
6  %
7  %   Usage:
8  %     generateCalStandard(f, type, offset): Returns a 1xN matrix
       with
9  %     impedance
10 %
11 %   Parameters and output:
12 %       f        1xN Frequency range.
13 %       type     Load type: 'short', 'open', or 'load'
14 %       offset   Distance in metres.
15 %%%%%%%%%%%%%%%%%%%%%%%%%%
16 % Optional arguments
17 %%%%%%%%%%%%%%%%%%%%%%%%%%
18 % 'graph' 'on'|'off'
19 attenuation = 0; %default
20 p_att = [2.50198798022228e-07 -0.00204450900646237];
21 radius = 0.015; % radius in metres
22 speedOfSound = 344;
23 N = length(varargin);
24 if mod(N,2)==1
25     error('gainComp: An odd number of optional arguments!');
26 end
27 for j=1:2:N
28     arg = varargin(j);
29     arg = cell2mat(arg);
30     switch arg
31         case 'attenuation'
32             attenuation = cell2mat(varargin(j+1));
```

```
33
34          case 'radius'
35              radius = cell2mat(varargin(j+1));
36
37          case 'c'
38              speedOfSound = cell2mat(varargin(j+1));
39
40          otherwise
41      end
42  end
43  N = size(f, 1);
44  c = speedOfSound*ones(N, 1);
45  offset = 2*offset*ones(N, 1);
46  wavelength = c ./ f;
47  k = 2*pi*f./c;
48  ratio = k.*radius;
49  if strcmp(type, 'short')
50      theta = offset./wavelength;
51      n = fix(theta);
52      theta = theta*2*pi;
53      remainder = offset - n.*wavelength;
54      phase = 2*pi*remainder./wavelength;
55      att = polyval(p_att, f).*theta;
56
57      gamma = (1+att).*exp(1i*phase);
58
59  elseif strcmp(type, 'open')
60      offset = 0.61*radius*2*ones(N, 1);        % end correction for
            an unflanged open
61      n = fix(offset./wavelength);
62      remainder = offset - n.*wavelength;
63      phase = 2*pi*remainder./wavelength;
64      real = ((k*radius).^2)/2 - ((k*radius).^4)/12 + ((k*radius)
            .^6)/144;
65      imag = 4/pi*(2*k*radius/3 - ((2*k*radius).^3)/45 + ((2*k*
            radius).^5)/1575);
66      %gamma = mag.*exp(1i*phase);
67      gamma = real + 1j*imag;
68
69  elseif strcmp(type, 'load')
70      gamma = zeros(N, 1);
71
72  else
73      error('Invalid type');
```

```
74 end
```

F.9 Circle Fit

Listing F.7: Circle fit program listing by G. Taubin [81].

```
1  function [a b R] = CircleFit(XY)
2  %
       ---------------------------------------------------------------------------
3  %
4  %     Circle fit by Taubin
5  %      G. Taubin, "Estimation Of Planar Curves, Surfaces And
       Nonplanar
6  %                 Space Curves Defined By Implicit Equations,
       With
7  %                 Applications To Edge And Range Image
       Segmentation",
8  %      IEEE Trans. PAMI, Vol. 13, pages 1115-1138, (1991)
9  %
10 %     Input: XY(n,2) is the array of coordinates of n points x(i)
       =XY(i,1), y(i)=XY(i,2)
11 %
12 %     Output: Par = [a b R] is the fitting circle:
13 %                           center (a,b) and radius R
14 %
15 %     Note: this fit does not use built-in matrix functions (
       except "mean"),
16 %           so it can be easily programmed in any programming
       language
17 %
18 %
       ---------------------------------------------------------------------------
19 n = size(XY,1);      % number of data points
20 centroid = mean(XY);   % the centroid of the data set
21 %     computing moments (note: all moments will be normed, i.e.
       divided by n)
22 Mxx = 0; Myy = 0; Mxy = 0; Mxz = 0; Myz = 0; Mzz = 0;
23 for i=1:n
24     Xi = XY(i,1) - centroid(1);  % centering data
25     Yi = XY(i,2) - centroid(2);  % centering data
26     Zi = Xi*Xi + Yi*Yi;
```

```
27      Mxy = Mxy + Xi*Yi;
28      Mxx = Mxx + Xi*Xi;
29      Myy = Myy + Yi*Yi;
30      Mxz = Mxz + Xi*Zi;
31      Myz = Myz + Yi*Zi;
32      Mzz = Mzz + Zi*Zi;
33  end
34  Mxx = Mxx/n;
35  Myy = Myy/n;
36  Mxy = Mxy/n;
37  Mxz = Mxz/n;
38  Myz = Myz/n;
39  Mzz = Mzz/n;
40  %    computing the coefficients of the characteristic polynomial
41  Mz = Mxx + Myy;
42  Cov_xy = Mxx*Myy - Mxy*Mxy;
43  A3 = 4*Mz;
44  A2 = -3*Mz*Mz - Mzz;
45  A1 = Mzz*Mz + 4*Cov_xy*Mz - Mxz*Mxz - Myz*Myz - Mz*Mz*Mz;
46  A0 = Mxz*Mxz*Myy + Myz*Myz*Mxx - Mzz*Cov_xy - 2*Mxz*Myz*Mxy + Mz*
        Mz*Cov_xy;
47  A22 = A2 + A2;
48  A33 = A3 + A3 + A3;
49  xnew = 0;
50  ynew = 1e+20;
51  epsilon = 1e-12;
52  IterMax = 20;
53  % Newton's method starting at x=0
54  for iter=1:IterMax
55      yold = ynew;
56      ynew = A0 + xnew*(A1 + xnew*(A2 + xnew*A3));
57      if abs(ynew) > abs(yold)
58          disp('Newton-Taubin goes wrong direction: |ynew| > |yold|')
                ;
59          xnew = 0;
60          break;
61      end
62      Dy = A1 + xnew*(A22 + xnew*A33);
63      xold = xnew;
64      xnew = xold - ynew/Dy;
65      if (abs((xnew-xold)/xnew) < epsilon), break, end
66      if (iter >= IterMax)
67           disp('Newton-Taubin will not converge');
68           xnew = 0;
```

```
69      end
70      if (xnew<0.)
71          fprintf(1,'Newton–Taubin␣negative␣root:␣␣x=%f\n',xnew);
72          xnew = 0;
73      end
74  end
75  % computing the circle parameters
76  DET = xnew*xnew - xnew*Mz + Cov_xy;
77  Center = [Mxz*(Myy-xnew)-Myz*Mxy , Myz*(Mxx-xnew)-Mxz*Mxy]/DET/2;
78  a = Center(1)+centroid(1);
79  b = Center(2)+centroid(2);
80  R = sqrt(Center*Center'+Mz);
81  %par = [Center+centroid , sqrt(Center*Center'+Mz)];
82  end     %     CircleFitByTaubin
```

Bibliography

[1] V. Gibiat and F. Laloë, "Acoustical impedance measurements by the two-microphone-three-calibration (TMTC) method," *J. Acoust. Soc. Am.*, vol. 88, no. 6, pp. 2533–2545, Dec. 1990.

[2] T. Y. Lung and Doige, "A time-averaging transient testing method for acoustic properties of piping systems and mufflers with flow," *J. Acoust. Soc. Am.*, vol. 73, no. 3, pp. 867–876, Mar. 1983.

[3] R. Boonen and P. Sas, "Determination of the acoustical impedance of an internal combustion engine exhaust," in *Proceedings of ISMA2002*, vol. 5, 2002, pp. 1939–1946.

[4] Z. Tao and A. Seybert, "A review of current techniques for measuring muffler transmission loss," in *SAE 2003 Noise & Vibration Conference and Exhibition*, May 2003.

[5] D. H. Keefe, R. Ling, and J. C. Bulen, "Method to measure acoustic impedance and reflection coefficient," *J. Acoust. Soc. Am.*, vol. 91, no. 1, pp. 470–485, Jan. 1992.

[6] D. Aylor, "Sound transmission through vegetation in relation to leaf area density, leaf width, and breadth of canopy," *J. Acoust. Soc. Am.*, vol. 51, no. 1B, pp. 411–414, Jan. 1972.

[7] T. Watanabe and S. Yamada, "Sound attenuation through absorption by vegetation," *J. Acoust. Soc. Jpn.*, vol. 17, no. 4, pp. 175–182, 1996.

[8] J. González Suárez, M. Machimbarrena Gutiérrez, A. Tarrero Fernández, T. Lorenzana Lorenzana, and A. Moreno, "Comparative analysis of several acoustic impedance measurements," in *Forum Acusticum Sevilla 2002*. Sociedad Española de Acústica, 2002. [Online]. Available: http://hdl.handle.net/10261/7995

[9] K. V. Horoshenkov, A. Khan, and H. Benkreira, "Acoustic properties of low growing plants," *J. Acoust. Soc. Am.*, vol. 133, no. 5, pp. 2554–2565, May 2013.

[10] J. Scott and K. Pennington, "Acoustic vector-corrected impedance meter," *IEEE Trans. Instrum. Meas.*, vol. 63, no. 12, pp. 2726–2732, Dec. 2014.

[11] D. T. Blackstock, *Fundamentals of Physical Acoustics*. J. Wiley & Sons, 2000.

[12] A. H. Benade and M. I. Ibisi, "Survey of impedance methods and a new piezo-disk-driven impedance head for air columns," *J. Acoust. Soc. Am.*, vol. 81, no. 4, pp. 1152–1167, Apr. 1987.

[13] J.-P. Dalmont, "Acoustic impedance measurement, Part I: A review," *Journal of Sound and Vibration*, vol. 243, no. 3, pp. 427–439, 2001.

[14] *Standard Test Method for Sound Absorption and Sound Absorption Coefficients by the Reverberation Room Method*, ASTM C 423, Rev. A, 2009.

[15] T. G. H. Basten and H.-E. de Bree, "Full bandwidth calibration procedure for acoustic probes containing a pressure and particle velocity sensor," *J. Acoust. Soc. Am.*, vol. 127, no. 1, pp. 264–270, Jan. 2010.

[16] A. F. Seybert and D. F. Ross, "Experimental determination of acoustic properties using a two-microphone random-excitation technique," *J. Acoust. Soc. Am.*, vol. 61, no. 5, pp. 1362–1370, May 1977.

[17] J. C. Webster, "An electrical method of measuring the intonation of cup-mouthpiece instruments," *J. Acoust. Soc. Am.*, vol. 19, no. 5, pp. 902–906, Sep. 1947.

[18] O. K. Mawardi, "Measurement of acoustic impedance," *J. Acoust. Soc. Am.*, vol. 21, no. 2, pp. 84–91, Mar. 1949.

[19] C. M. de Blok and R. F. M. van den Brink, "Direct-reading one-port acoustic network analyzer," *J. Audio Eng. Soc.*, vol. 41, no. 4, pp. 231–238, 1993.

[20] W. K. R. Lippert, "The practical representation of standing waves in an acoustic impedance tube," *Acustica*, vol. 3, no. 3, pp. 153–160, 1953.

[21] C. M. de Blok and R. F. M. van den Brink, "Full characterization of linear acoustic networks based on n-ports and S parameters," *J. Audio Eng. Soc.*, vol. 40, no. 6, pp. 517–523, Jun. 1992.

[22] *Acoustics — Determination of sound absorption coefficient and impedance in impedance tubes — Part 1: Method using standing wave ratio*, ISO Std. 10 534-1, 1996.

[23] *Standard Test Method for Impedance and Absorption of Acoustical Materials by Impedance Tube Method*, ASTM C 384, 2004.

[24] H.-E. de Bree, P. Leussink, T. Korthorst, H. Jansen, T. S. Lammerink, and M. Elwenspoek, "The microflown: a novel device for measuring acoustic flows," *Sensors and Actuators A: Physical*, vol. 54, no. 1-3, pp. 552–557, Jun. 1996.

[25] R. L. Pratt, S. J. Elliott, and J. M. Bowsher, "The measurement of the acoustic impedance of brass instruments," *Acustica*, vol. 38, no. 4, pp. 236–246, Oct. 1977.

[26] Y. Liu and F. Jacobsen, "Measurement of absorption with a p-u sound intensity probe in an impedance tube (l)," *J. Acoust. Soc. Am.*, vol. 118, no. 4, pp. 2117–2120, Oct. 2005.

[27] A. F. Seybert. Notes on absorption and impedance measurements. University of Kentucky. [Online]. Available: http://www.engr.uky.edu/vac/public_html/Absorption_Meas.pdf

[28] J. Y. Chung and D. A. Blaser, "Transfer function method of measuring in-duct acoustic properties. i. theory," *J. Acoust. Soc. Am.*, vol. 68, no. 3, pp. 907–913, Sep. 1980.

[29] J. Y. Chung and D. A. Blaser, "Transfer function method of measuring in-duct acoustic properties. ii. experiment," *J. Acoust. Soc. Am.*, vol. 68, no. 3, pp. 914–921, Sep. 1980.

[30] H. Bodén and M. Åbom, "Influence of errors on the two-microphone method for measuring acoustic properties in ducts," *J. Acoust. Soc. Am.*, vol. 79, no. 2, pp. 541–549, Feb. 1986.

[31] W. T. Chu, "Extension of the two-microphone transfer function method for impedance tube measurements," *J. Acoust. Soc. Am.*, vol. 80, no. 1, pp. 347–348, Jul. 1986.

[32] P. Banks-Lee and H. Peng, "Length error analysis for impedance tube measurements," *J. Acoust. Soc. Am.*, vol. 85, no. 4, pp. 1769–1772, Apr. 1989.

[33] *Acoustics — Determination of sound absorption coefficient and impedance in impedance tubes — Part 2: Transfer-function method*, ISO Std. 10 534-2, 1998.

[34] *Standard Test Method for Impedance and Absorption of Acoustical Materials Using A Tube, Two Microphones and A Digital Frequency Analysis System*, ASTM E 1050, 1998.

[35] B. F. G. Katz, "Method to resolve microphone and sample location errors in the two-microphone duct measurement method," *J. Acoust. Soc. Am.*, vol. 108, no. 5, pp. 2231–2237, Nov. 2000.

[36] R. Boonen, P. Sas, W. Desmet, W. Lauriks, and G. Vermeir, "Calibration of the two microphone transfer function method to measure acoustic impedance in a wide frequency range," in *Proceedings of ISMA 2006*, Leuven, Belgium, 2006, pp. 4501–4512.

[37] X. Jing and X. Sun, "Flat-response sound source technique for using the two-microphone method in an impedance tube (L)," *J. Acoust. Soc. Am.*, vol. 122, no. 5, pp. 2519–2521, Nov. 2007.

[38] R. Boonen, P. Sas, W. Desmet, W. Lauriks, and G. Vermeir, "Calibration of the two microphone transfer function method by determining the hard wall impedance at shifted reference sections," in *Proceedings of ISMA 2008*, Leuven, Belgium, 2008, pp. 1413–1424.

[39] J. L. Roux, J.-P. Dalmont, and B. Gazengel, "A new impedance tube for large frequency band measurement of absorbing materials," *J. Audio Eng. Soc.*, vol. 123, no. 5, pp. 961–964, 2008.

[40] X. Sagartzazu, L. Hervella-Nieto, and J. Pagalday, "Review in sound absorbing materials," *Archives of Computational Methods in Engineering*, vol. 15, no. 3, pp. 311–342, May 2008.

[41] Brüel & Kjær. (2009) 4206 impedance tube kit documentation. Brüel & Kjær. http://www.bksv.com/doc/bp1039.pdf.

[42] C. D. Smith and T. L. Parrott, "Comparison of three methods for measuring acoustic properties of bulk materials," *J. Acoust. Soc. Am.*, vol. 74, no. 5, pp. 1577–1582, Nov. 1983.

[43] M. G. Jones and T. L. Parrott, "Evaluation of a multi-point method for determining acoustic impedance," *Mechanical Systems and Signal Processing*, vol. 3, no. 1, pp. 15–35, Jan. 1989.

[44] J. D. Mcintosh, M. T. Zuroski, and R. F. Lambert, "Standing wave apparatus for measuring fundamental properties of acoustic materials in air," *J. Acoust. Soc. Am.*, vol. 88, no. 4, pp. 1929–1938, Oct. 1990.

[45] Y. Champoux and M. R. Stinson, "Measurement of the characteristic impedance and propagation constant of materials having high flow resistivity," *J. Acoust. Soc. Am.*, vol. 90, no. 4, pp. 2182–2191, Oct. 1991.

[46] W. T. Chu, "Impedance tube measurements- a comparative study of current practices." *Noise Control Engineering Journal*, vol. 37, no. 1, pp. 37–44, 1991.

[47] B. H. Song and J. S. Bolton, "A transfer-matrix approach for estimating the characteristic impedance and wave numbers of limp and rigid porous materials," *J. Acoust. Soc. Am.*, vol. 107, no. 3, pp. 1131–1152, Mar. 2000.

[48] J.-P. Dalmont, "Acoustic impedance measurement, Part II: A new calibration method," *Journal of Sound and Vibration*, vol. 243, no. 3, pp. 441–459, 2001.

[49] K. M. Ho, Z. Yang, X. Zhang, and P. Sheng, "Measurements of sound transmission through panels of locally resonant materials between impedance tubes," *Appl. Acoust.*, vol. 66, no. 7, pp. 751–765, Jul. 2005.

[50] Y. Salissou and R. Panneton, "A general wave decomposition formula for the measurement of normal incidence sound transmission loss in impedance tube," *J. Acoust. Soc. Am.*, vol. 125, no. 4, pp. 2083–2090, Apr. 2009.

[51] R. T. Muehleisen and W. I. C. Beamer, "Comparison of errors in the three- and four-microphone methods used in the measurement of the acoustic properties of porous materials," *Acoustics Research Letters Online*, vol. 3, no. 4, pp. 112–117, Jun. 2002.

[52] O. Doutres, Y. Salissou, N. Atalla, and R. Panneton, "Evaluation of the acoustic and non-acoustic properties of sound absorbing materials using a three-microphone impedance tube," *Applied Acoustics*, vol. 71, no. 6, pp. 506 – 509, 2010. [Online]. Available: http://www.sciencedirect.com/science/article/B6V1S-4YC8RH8-2/2/5b17adc5a4ac91db5ed5d10760f5750a

[53] W.-S. Cheung, M.-J. Jho, and Y.-H. Kim, "Improved method for the measurement of acoustic properties of a sound absorbent sample in the standing wave tube," *J. Acoust. Soc. Am.*, vol. 97, no. 5, pp. 2733–2739, May 1995.

[54] S.-H. Jang and J.-G. Ih, "On the multiple microphone method for measuring in-duct acoustic properties in the presence of mean flow," *J. Acoust. Soc. Am.*, vol. 103, no. 3, pp. 1520–1526, Mar. 1998.

[55] J. Price. (2008, Jan.) Acoustic VNA user's guide. University of Colorado. [Online]. Available: http://spot.colorado.edu/~pricej/pdf%20docs/AVNA%20User's%20Guide.pdf

[56] E. Sarradj, J. Hübelt, E. Elsaghir, and P. Holstein. Extended impedance tube measurements of porous absorbers. [Online]. Available: http://www.acousticsgroup.com/pdf/sarradj_tube_DAGA2004.pdf

[57] K. Pennington, J. Scott, and K. Bodman, "Determining acoustical directionality in an impedance tube using multiple fixed microphones," in *Proceedings of the 18th Electronics New Zealand Conference*, no. 18, Nov. 2011, pp. 73–76.

[58] Y. Ryu. The acoustic impedance measurement system using two microphones. Brüel & Kjær Sound and Vibration Measurement A/S.

[59] A. Lefebvre, G. P. Scavone, J. Abel, and A. Buckiewicz-Smith, "A comparison of impedance measurements using one and two microphones," in *Proceedings of the ISMA*, Barcelona, Spain, 2007.

[60] D. Rytting, "ARFTG 50 year network analyzer history," in *IEEE MTT-S International Microwave Symposium Digest*, Atlanta, GA, Jun. 2008, pp. 11–18.

[61] (2014, Nov.) zijitek. [Online]. Available: http://www.zijitek.com.my/microwave/original_pic/adjustable_slot.gif

[62] R. G. Carter, *Electromagnetic waves : microwave components and devices*. Chapman and Hall, 1990.

[63] S. B. Cohn and R. Levy, "History of microwave passive components with particular attention to directional couplers," *IEEE Trans. Microw. Theory Techn.*, vol. 32, no. 9, pp. 1046–1054, Sep. 1984. [Online]. Available: http://wenku.baidu.com/view/116af7ef856a561252d36f56.html

[64] R. Levy, "A guide to the practical application of chebyshev functions to the design of microwave components," *Proc. IEE*, vol. 106, no. 10, pp. 193–199, Sep. 1959.

[65] B. Epsztein, "Backward flow travelling wave devices," French Patent FRD1 035 379 19 510 413, Aug. 24, 1953.

[66] National Instruments. National Instruments. [Online]. Available: http://download.ni.com/evaluation/rf/Introduction_to_Network_Analyzer_Measurements.pdf

[67] G. F. Engen and C. A. Hoer, "Thru-reflect-line: An improved technique for calibrating the dual six-port automatic network analyzer," *IEEE Trans. Microw. Theory Techn.*, vol. 27, no. 12, pp. 987–993, Dec. 1979.

[68] K. Wong, "The "unknown thru" calibration advantage," in *ARFTG Conference Digest*, vol. 63rd, Jun. 2004, pp. 73–81.

[69] J. P. Dunsmore, *Handbook of Microwave Component Measurements: with Advanced VNA Techniques*. Wiley, 2012.

[70] A. Ferrero and U. Pisani, "Two-port network analyzer calibration using an unknown 'thru'," *IEEE Microw. Guided Wave Lett.*, vol. 2, no. 12, pp. 505–506, Dec. 1992.

[71] *LM3876 Overture Audio Power Amplifier Series High-Performance 56W Audio Power Amplifier w/Mute*, Texas Instruments, Mar. 2013. [Online]. Available: http://www.ti.com.cn/cn/lit/ds/symlink/lm3876.pdf

[72] *Agilent 4395A Network/Spectrum/Impedance Analyzer Data Sheet*, Agilent Technologies, Feb. 2001, revised: Oct. 2007. [Online]. Available: http://literature.cdn.keysight.com/litweb/pdf/5965-9340E.pdf

[73] S. C. Douglas and D. P. Mandic, "A family of least-squares magnitude phase algorithms," in *Proc. IEEE Conf. Acoust., Speech & Sig. Proc.*, Kyoto, Mar. 2012, pp. 3769–3772.

[74] S. Barrera-Figueroa, K. Rasmussen, and F. Jacobsen, "The acoustic center of laboratory standard microphones," *J. Acoust. Soc. Am.*, vol. 120, no. 5, pp. 2668–2674, Nov. 2006.

[75] J.-F. Allard and Y. Champoux, "New empirical equations for sound propagation in rigid frame fibrous materials," *J. Acoust. Soc. Am.*, vol. 91, no. 6, pp. 3346–3353, Jun. 1992.

[76] R. Levy and L. Lind, "Synthesis of symmetrical branch-guide directional couplers," *IEEE Trans. Microw. Theory Techn.*, vol. 16, no. 2, pp. 80–89, Feb. 1968.

[77] P. Lagasse, "The realization of an acoustical directional coupler," *J. Sound Vib.*, vol. 15, no. 3, pp. 367–372, 1971.

[78] J. K. Hunton, "Analysis of microwave techniques by means of signal flow graphs," *IRE Transactions on Microwave Theory and Techniques*, vol. 8, no. 2, pp. 207–212, Mar. 1960.

[79] D. Rytting. An analysis of vector measurement accuracy enhancement techniques. Hewlett-Packard Company. [Online]. Available: http://www.hparchive.com/seminar_notes/a-218.pdf

[80] D. Rytting. (1987) Advances in microwave error correction techniques. Hewlett-Packard Company. [Online]. Available: http://www.hparchive.com/seminar_notes/a-138.pdf

[81] G. Taubin, "Estimation of planar curves, surfaces, and nonplanar space curves defined by implicit equations with applications to edge and range image segmentation," *IEEE Trans. Pattern Anal. Mach. Intell.*, vol. 13, no. 11, pp. 1115–1138, Nov. 1991.

[82] R. B. Marks, "A multiline method of network analyser calibration," *IEEE Trans. Microw. Theory Techn.*, vol. 39, no. 7, pp. 1205–1215, Jul. 1991.

[83] S. Mason, "Feedback theory - further properties of signal flow graphs," *Proceedings of the IRE*, vol. 44, no. 7, pp. 920–926, Jul. 1956.